The Role of Neuroinflammation in Alzheimer's Disease

Dimitrios Ion Sideris

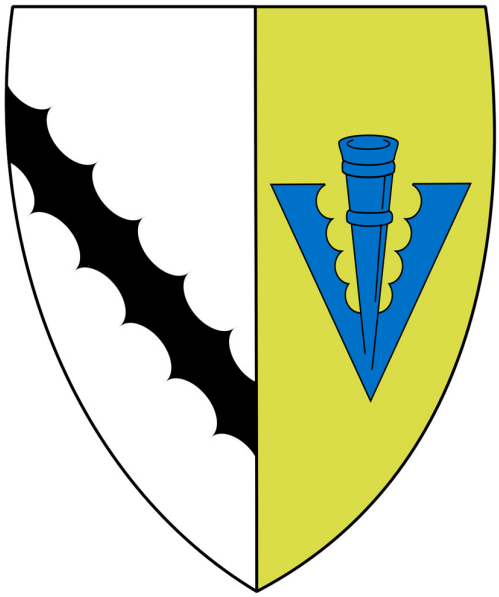

Sidney Sussex College

Prof Sir David Klenerman Group

This thesis is submitted for the degree of Doctor of Philosophy at the

University of Cambridge

May 2021

Declaration

This thesis is the result of my own work and includes nothing which is the outcome of work done in collaboration except as declared in the preface and specified in the text. It is not substantially the same as any work that has already been submitted before for any degree or other qualification except as declared in the preface and specified in the text. It does not exceed the prescribed word limit for the Physics and Chemistry Degree Committee.

This thesis has been reviewed and approved by AstraZeneca's sign-off process (The PSO Process). This process employs the least restrictive means possible, while ensuring scientific and medical accuracy of content, compliance with applicable publication standards, regulatory compliance (for example, avoidance of inappropriate promotional statements) and, protection of intellectual property through patent attorney review.

Dimitrios Ion Sideris

May 2021

Abstract

The Role of Neuroinflammation in Alzheimer's Disease

Dimitrios Ion Sideris

Neuroinflammation is believed to play a key role in Alzheimer's disease, as evidenced by recent genome wide association studies highlighting several risk genes associated with the immune response. Misfolded and aggregated proteins bind to pattern recognising receptors on glial cells in the brain, causing the production and release of pro-inflammatory messengers, which contribute to disease progression. By studying the relationship between protein aggregation and neuroinflammation at early stages, we can begin to uncover the mechanisms underlying the initiation of the disease.

Chapter 3 describes the optimisation of a neuroinflammation assay that uses a BV2 microglial cell line to test the inflammatory potential of synthetic amyloid beta 42 aggregates. In conjunction with a liposome-permeability assay and an immunoprecipitation assay, this assay has been used to validate a proprietary amyloid beta 42 antibody from MedImmune (now AstraZeneca).

Most neuroinflammation studies have focused extensively on synthetic aggregates and to a much lesser extent on endogenous soluble aggregates from human tissue. The aggregates present in humans are still poorly characterised due to a lack of suitable methods required for characterising the low concentration of heterogeneous aggregates present.

In Chapter 4, a variety of biophysical methods have been employed to characterise the soluble aggregates present in human Alzheimer's disease brains at Braak stage III. We have identified the similarities and differences between the soluble aggregates in eight different regions by providing a detailed characterisation of their size, morphology, structure, neurotoxicity, inflammatory potential, and capability to permeabilise a lipid membrane. This data shows that soluble aggregates of a range of sizes and morphologies, capable of causing inflammation, are already present in all brain regions at Braak stage III and that aggregation is occurring by the same processes all over the brain to a greater or lesser extent.

Acknowledgements

I would like to thank Prof Sir David Klenerman and Dr Damian Crowther for their guidance and mentorship throughout this project. Special thanks to the Neuroscience team at AstraZeneca Granta Park site, and the members of the Prof Sir David Klenerman, Prof Steven Lee, Prof Clare Bryant, Prof Christopher Dobson and Prof Sonia Gandhi groups, for their motivational and technical support. I am very grateful to AstraZeneca and the Biotechnology and Biological Sciences Research Council (BBSRC) for funding this research.

I would also like to thank the Cambridge Brain Bank and Addenbrooke's hospital, Cambridge, for processing and providing Alzheimer's disease brain tissue for this study. The Human Research Tissue Bank is supported by the NIHR Cambridge Biomedical Research Centre.

I would like to express my gratitude towards the patients and their families for their donations of brain tissue, without which this research would not be possible.

I am particularly grateful for the following people, who went out of their way to support me on multiple occasions and greatly improved my PhD experience (in no particular order): Kushal Rugjee, Graham Fraser, Robyn McAdam, Pete Thornton, Olly Freeman, Andy Billinton, Mike Perkinton, Kieren Allinson, Rob Pickering, Lee Hopkins, Prof Clare Bryant, Claire Butler, Patrick Flagmeier, Suman De, Alex Carr, Derya Emin, Anoushka Handa, Santiago Sanchez, Chris Taylor, Anna Lippert, Markus Körbel, Jason C. Sang, John Danial, Juan Varela, Margarida Rodrigues, Zengjie Xia, Klara Kulenkampff, Bing Li, Eric Zuo, Daniel Esteban, Steph Huang, Yannis Dimitroulas, Maximilien Rothier Bautzer, Aryan Nikhab, Ryan Stephenson, Julien Mahin, Nick Bampos, & Rachel MacDonald.

I would like to thank my viva examiners Dr Janet Kumita and Prof Selina Wray for taking the time to read and discuss this thesis.

Finally, a huge thank you to my family and Sarah Davies for putting up with me throughout the past 4 years.

List of Abbreviations

AAV	adeno-associated virus
Aβ	amyloid-beta
Aβ-DP	amyloid-beta-degrading protease
AC	anterior cingulate cortex
aCSF	artificial cerebrospinal fluid
AD	Alzheimer's disease
AD PAINT	aptamer DNA-PAINT
AF	Alexa fluor
AFM	atomic force microscopy
AICD	amyloid precursor protein intracellular domain
AMPA	α-amino-3-hydroxyl-5-methyl-4-isoxazolepropionic acid
ANOVA	analysis of variance
AP-1	activator protein 1
ApoE	apolipoprotein E
APP	amyloid precursor protein
ATB	antibody
a.u.	arbitrary unit
BACE1	β-secretase 1
BBB	blood-brain barrier
BBSRC	Biotechnology and Biological Sciences Research Council
BCA	bicinchoninic acid
BDNF	brain-derived neurotrophic factor
BSA	bovine serum albumin
°C	degree(s) Celsius

Cas9	CRISPR associated protein 9
Cat	catalogue number
CBL	cerebellum
CD14	cluster of differentiation 14
cm	centimetre(s)
CRISPR	clustered regularly interspaced short palindromic repeats
CSF	cerebrospinal fluid
CTF	c-terminal fragment
D1	dichroic
DAMP	damage-associated molecular pattern
DIV	days *in vitro*
DMEM	Dulbecco's modified eagle medium
DNA	deoxyribonucleic acid
EC	entorhinal cortex
EC_{50}	half maximal effective concentration
EDTA	ethylenediaminetetraacetic acid
ELISA	enzyme-linked immunosorbent assay
EMCCD	electron-multiplying charge coupled device
Fab	antigen-binding fragment
FPLC	fast protein liquid chromatography
FBS	foetal bovine serum
FC	frontal cortex
Fc	fragment, crystallisable
FCγR	fragment crystallizable region gamma receptor
Fig	figure

g	grams
$g_{(av)}$	gravitational force
GABA	γ-aminobutyric acid
GFP	green fluorescent protein
GSH	glutathione
GuHCl	guanidine hydrochloride
GWAS	genome-wide association study
HBSS	Hank's balanced salt solution
HEPES	4-(2-hydroxyethyl)-1-piperazineethanesulfonic acid
HFIP	1,1,1,3,3,3 -Hexafluoro-2-propanol
HPC	hippocampus
hr	hour(s)
iBMMs	immortalised bone marrow-derived macrophages
IC_{50}	half maximal inhibitory concentration
ICD	intracellular domain
IDE	insulin-degrading enzyme
IFN-γ	interferon-γ
IKK	inhibitor of nuclear factor-kB kinase
IL	interleukin
iNOS	inducible nitric-oxide synthase
iPSCs	induced pluripotent stem cells
IRAK	interleukin-1 receptor-associated kinase
JNK	c-Jun N-terminal kinase
kDa	kilodalton(s)
L	litre(s)

L1-L5	lenses 1-5
lncRNA	long non-coding RNA
LPS	lipopolysaccharide
LTP	long-term potentiation
M	molar
m	milli-
M1-M3	mirrors 1-3
MAPK	mitogen-activated protein kinase
MedI	MedImmune (now AstraZeneca)
min	minute(s)
mol	mole(s)
MSD	Meso Scale Delivery
MyD88	myeloid differentiation primary response 88
n	nano-
NBM	neurobasal media
ND	neutral-density
NF-κB	nuclear factor kappa-light-chain-enhancer of activated B cells
NIA	neuroinflammation assay
NMDA	N-methyl-D-aspartate
p	pico-
PAINT	points accumulation for imaging in nanoscale topography
PAMP	pathogen-associated molecular pattern
PBS	phosphate-buffered saline
PDL	poly-D-lysine
PEG	polyethylene glycol

PFA	paraformaldehyde
pH	power of hydrogen
PK	proteinase-K
PM	postmortem
POPC	1-palmitoyl-2-oleoyl-sn-glycero-3-phosphocholine
PP	posterior parahippocampal gyrus
PRR	pattern-recognising receptor
PS-1	presenilin-1
PS-2	presenilin-2
p-value	probability (significance) value
PVC	primary visual cortex
RNA	ribonucleic acid
ROS	reactive oxygen species
RSLA	*Rhodobacter sphaeroides* lipid A
sAPPα	soluble peptide APP-α
sAPPβ	soluble peptide APP-β
SD	standard deviation
SDS-PAGE	sodium dodecyl sulfate polyacrylamide gel electrophoresis
SiMPull	single-molecule pull-down
SPIP	scanning probe image processor
SSPE	saline-sodium phosphate-ethylenediaminetetraacetic acid
TAK1	transforming growth factor β-activated kinase 1
TAPI-0	tumour necrosis factor-α protease inhibitor-0
TBS	tris-buffered saline
TGFβ	transforming growth factor-β

ThT	thioflavin T
TIR	Toll/Interleukin-1 receptor
TIRF	total internal reflection microscopy
TLR	toll-like receptor
TNFα	tumour necrosis factor α
TNFR	tumour necrosis factor receptor
TRAF6	TNF receptor-associated factor 6
TREM2	triggering receptor expressed on myeloid cells 2
v	volume
VAC	visual association cortex
W	watt(s)
ε	molar extinction coefficient
μ or u	micro-

Table of Contents

1: Literature Review

Parts of this chapter have been adapted from the following published manuscript:

Dimitrios I. Sideris, John S. H. Danial, Derya Emin et al. Soluble amyloid beta-containing aggregates are present throughout the brain at early stages of Alzheimer's disease, Brain Communications, 2021.

1.1. Alzheimer's disease

Alzheimer's disease (AD) is a progressive neurodegenerative disorder that targets the central nervous system. It is the leading cause of dementia, accounting for 60-80 percent of reported cases.[1] Dementia is characterised by a wide range of symptoms including memory loss, problems with language, difficulties with problem-solving, executive dysfunction and general cognitive impairment. These symptoms are a product of the degeneration of neuronal cells, as well as the dysfunction of synaptic connections between them. In patients with advanced AD, the loss of neurons leads to a significant physical shrinkage of the brain, notably with a great reduction in grey matter and the formation of large empty vacuoles within the brain tissue.[2,3] AD is most prevalent in people over the age of 65 and is not part of the normal ageing process. The progressively debilitating nature of this disease makes daily tasks impossible to carry out without the help of a carer. In the UK, the cost of dementia research and social care has reached £26.3 billion a year and is on the rise. When measured in 2014, approximately 850,000 people were suffering from dementia in the UK alone. This number is increasing dramatically and is estimated to reach two million by 2050.[4] Dementia and AD are currently the leading cause of death in the UK.[5] Due to an ageing population, there is a socio-economic urgency to find a prevention or therapeutic strategy for AD.

In order for a therapy or preventative treatment to be developed, there needs to be a better understanding of AD's complex aetiology. AD can be split into two subtypes, familial and sporadic. Familial AD is the rarer form, accounting for 1% of cases and is caused by a subset of dominantly inherited genes that can be passed from one generation to the next. These include the genes that encode presenelin-1 (PS-1), presenelin-2 (PS-2) and the amyloid precursor protein (APP), all of which affect the processing of the amyloid beta (Aβ) protein, which is heavily implicated in AD. [6–8]

Sporadic AD develops through environmental risk factors such as age, as well as non-dominant genetic mutations, which generally affect the way Aβ is cleared. Apolipoprotein E (ApoE) is the strongest sporadic risk gene for AD. There are three types of APOE in humans, APOEε2, APOEε3, APOEε4. APOE is secreted by astrocytes and lipidated by ABCA1. Lipidated APOE has been shown to interact with Aβ aggregates and triggering receptor expressed on myeloid cells 2 (TREM2), another genetic risk factor for AD, and binds to low-density lipid (LDL) receptors, such as LRP1, LDLR, VLDLR, ApoER2.[9] Aβ42 coupled with APOEε3 and APOEε4 is more toxic than when coupled with APOEε2,[10] further highlighting their involvement in AD pathology. GWAS studies have identified over 25 genetic loci that cause genetic risks for sporadic AD, several which are highly expressed in microglia.[11–13] These risk factors can contribute to the assembly of toxic proteins that are believed to cause downstream toxic events, leading to disease pathology. The essential diagnostic hallmarks of AD include extracellular Aβ plaques and intracellular neurofibrillary tangles consisting of hyperphosphorylated tau protein.[14,15] During disease progression, neurofibrillary tangle pathology tends to develop and spread throughout the brain in distinct stages (Braak stages) that correlate with the degree of Aβ pathology (Thal phases) as well as cognitive decline (**Figure 1**).[16,17] Tau inclusions first start appearing in the entorhinal cortex and neighbouring areas (stages I/II), followed by the hippocampus and frontal cortex (stages III/IV), which then spread to most of the neocortex. Aβ pathology tends to originate in the frontal cortex (phase 1), and spreads through the neocortex, hippocampus, amygdala, basal ganglia (phases 2/3), before reaching the midbrain, lower brainstem, and cerebellum (phases 4/5) in advanced AD.[18] The brain regions that are affected early are associated with memory (hippocampus/entorhinal cortex), higher cognitive function, emotions, impulse control and problem solving (frontal lobe).

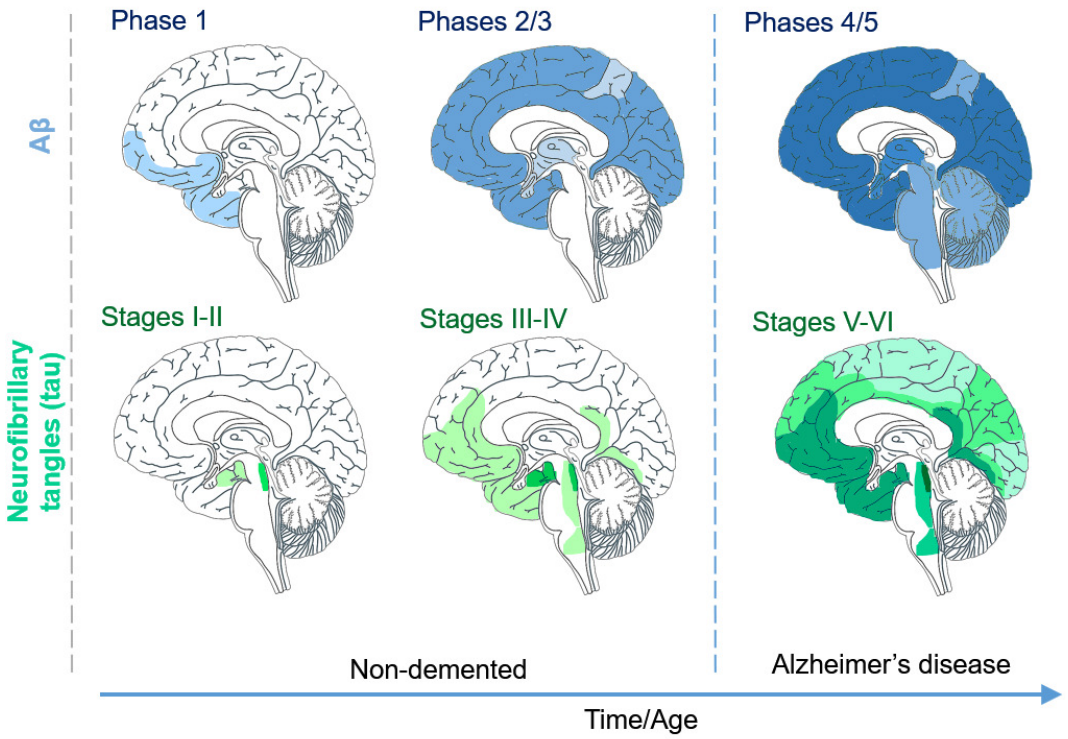

Figure 1: Aβ and tau pathology in Alzheimer's disease

During AD progression, Aβ (blue) and tau (green) pathology develop through the brain in several distinct stages that correlate with cognitive decline. Adapted from [18,19].

AD genetics affect Aβ processing (familial genes) and Aβ clearance (sporadic genes), suggesting that Aβ pathology might precede tau pathology. However, Aβ-induced neuronal death has been shown to be tau-dependent both *in vivo* and in cultured neurons, suggesting that while Aβ might be upstream of tau, tau is responsible for the neuronal death in AD.[20] Toxicity from Aβ and tau pathology can occur independently, however Aβ buildup has been shown to induce tau hyperphosphorylation, suggesting a link between the two.[21] Further highlighting this link, tau has been shown to be able to influence Aβ aggregation, as seen from the decreased amyloidogenic processing of APP in tau knockout APP/PS1 mice.[22] A better understanding is required of how these proteins assemble and their mechanisms of toxicity.

1.2. Amyloid Assembly

The aggregation of monomeric proteins into toxic species is a common mechanism involved in many neurodegenerative diseases[23]. The protein most strongly associated with AD pathology is the 42-amino acid protein, Aβ. The Aβ peptide is formed by the sequential cleavage of the amyloid precursor protein (APP) by β- and γ-secretases (**Figure 2**). The cleavage of APP can occur on the plasma membrane, the endoplasmic reticulum, golgi apparatus, or in endocytic vesicles.[24,25] APP's functional role remains elusive, but has recently been suggested to be a modulator of synaptic transmission.[26]

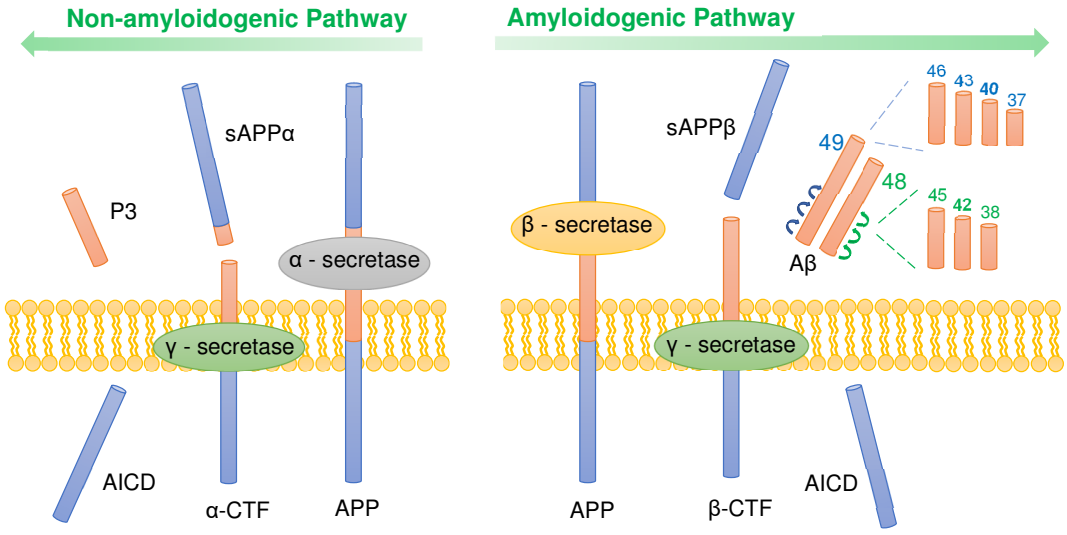

Figure 2: Amyloidogenic vs non-amyloidogenic pathways of APP cleavage

APP = amyloid precursor protein, *sAPPα* = soluble peptide APP-α, *sAPPβ* = soluble peptide APP-β, *AICD* = APP intracellular domain, *α-CTF* = α-C terminal fragment, *β-CTF* = β-C terminal fragment

The non-amyloidogenic pathway (left) involves the proteolytic cleavage of APP by α- and γ-secretase, forming sAPPα and C-terminal fragments (α-CTF, AICD and p3). The amyloidogenic pathway (right) involves APP cleavage by β- and γ-secretase, resulting in the formation of sAPPβ, C-terminal fragments (β-CTF and AICD) and Aβ. Two long forms of Aβ, 48 and 49 amino acids long, are produced and sequentially cleaved causing tripeptide or tetrapeptide release giving rise to a range of different Aβ peptide lengths (37-46 amino acids).[27,28] The Aβ42 form is the most susceptible to aggregation, which results in cytotoxic effects.[29]

The Aβ42 peptide is non-toxic in its monomeric form but is highly prone to misfolding and aggregating into toxic protein species. As aggregation progresses, the amyloid proteins adopt a beta-sheet structure, which is more stable and therefore harder to

degrade. The amyloid assembly mechanism follows a lag, elongation and plateau phase (**Figure 3**).[30]

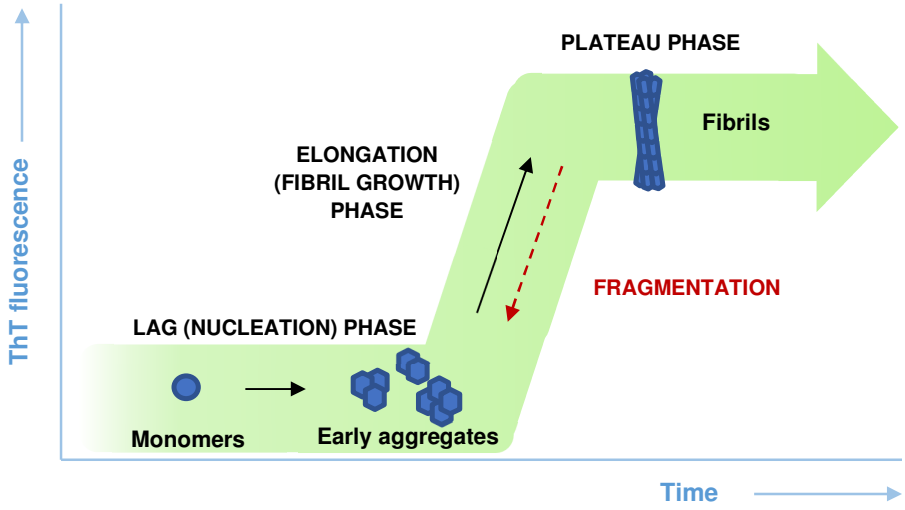

Figure 3: Kinetics of amyloid formation

ThT = Thioflavin T

Amyloid fibrils are formed from the misfolding and aggregation of monomeric amyloid peptides into soluble prefibrillar aggregates, in what is known as the lag or nucleation phase. By acting as a template for other intermediates, these early aggregates promote rapid fibril growth until a maximum steady state is reached (plateau phase).[31] Amyloid aggregation kinetics can be measured by ThT fluorescence, a dye that fluoresces when bound to beta-sheet structures.

Within these three macroscopic phases, there are four smaller events taking place. Primary nucleation, elongation, secondary nucleation and fragmentation occur in all three kinetic stages, although at varying rates.[32] These are dependent on rate constants, as well as the concentrations of reacting protein species. Following the formation of soluble early aggregates (nuclei), monomeric proteins begin assembling at the ends of existing aggregates and form insoluble fibrillar structures. Fibrils can act as a platform from which other proteins can then begin to assemble; a process known as secondary nucleation.[33] In some cases, fibrils are also prone to fragmentation, which reduces them to shorter assemblies. This enhances amyloid cytotoxicity, as shorter fibrils tend to cause more membrane disruption than longer fibrils.[34] Aβ is also prone to being post-translationally modified. Nitrated, pyroglutamylated or phosphorylated Aβ can cause an increase in reactive oxygen species (ROS), which leads to neurotoxicity.[35]

The amyloid assembly mechanism has become an important target for drug therapies, however, there needs to be a better understanding of which stage of the assembly to focus on. Some literature suggests that early prefibrillar soluble aggregates, termed oligomers, are the most toxic to cells.[36–38] However, the heterogeneous nature of Aβ42 aggregation has left this question up for debate. This is further complicated by the fact that synthetic or recombinant Aβ42 is extensively used for experimentation. While they can be used to provide a rough idea of amyloid aggregation kinetics and cytotoxicity, it is unclear how physiologically relevant these proteins are to the endogenous Aβ42 found in human patients. This is because unlike *in vitro* aggregates, endogenous Aβ can undergo post-translational modifications, that can cause increased aggregation, neurotoxicity, amyloidogenicity, and suppression of hippocampal long-term potentiation (LTP).[35] Furthermore, many studies tend to separate Aβ42 aggregates based on size, using size exclusion chromatography, ultrafiltration, or fractionation using a chemical gradient. However, size does not necessarily distinguish soluble aggregates from fibrils; it is the structure that seems to be of more importance.[39]

The assembly of the Aβ42 peptide plays a critical role in the initiation of AD, as supported by the genetics of APP, PS1, and PS2. It has given rise to the amyloid-cascade hypothesis; the idea that genetic and environmental risk factors lead to the production and aggregation of Aβ42, followed by downstream toxic events resulting in synaptic and neuronal dysfunction and loss.[40–43] These toxic events include widespread oxidative stress, glutamate excitotoxicity, tau aggregation and neuroinflammation.

1.3. Neuroinflammation

The innate immune response in the brain is triggered by several different factors, including trauma, invading pathogens and the presence of toxic peptides.[44] This response is crucial as it helps control the disturbance of the initial infliction event by repairing damaged tissue and removing dead cells. The immune response is mediated by glial cells, namely astrocytes and microglia.[45] They help provide metabolic and structural support to neurons and protect the brain from pathogens. At the early stages of AD, astrocytes and microglia gather around senile plaques to clear Aβ deposits through phagocytosis.[46] However, in response to chronic inflammatory signals such as damage-associated molecular patterns (DAMPs), which include Aβ aggregates,

senile plaques and tau neurofibrillary tangles, glial cells are unable to carry out their function and adopt an altered proinflammatory morphology.[47] In this state, the neuroprotective actions of these cells are outweighed by the production of proinflammatory cytokines and chemokines. An overproduction of these cytokines can cause significant damage, by inducing Aβ42 aggregation, tau hyper-phosphorylation, blood-brain barrier (BBB) permeability and inhibiting neurogenesis, resulting in neurodegeneration (**Figure 4**).[48–50] It is widely reported that Aβ42 aggregates can cause neuroinflammation, which in turn induces Aβ42 aggregation, suggesting the two mechanisms might be in a positive feedback loop.[51] Cytokine release from microglia promotes the astrocytic proinflammatory state, and vice versa. This active glial phenotype has been shown to play a role in early disease.[52] As the disease progresses, there is an increase in active microglia, with a change towards dystrophic microglia in the late stages of the disease.[53]

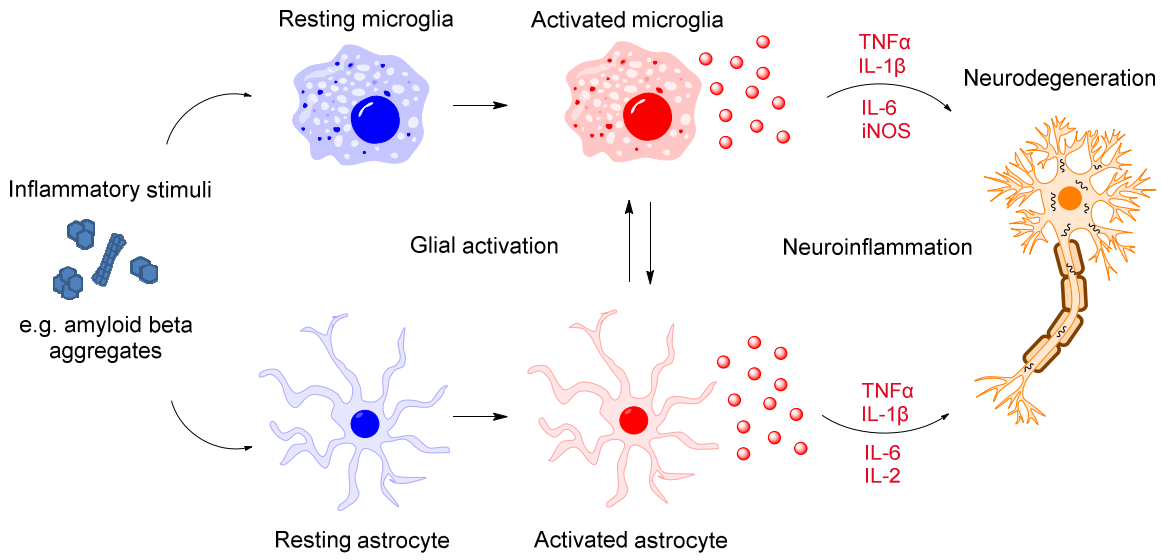

Figure 4: The role of neuroinflammation in Alzheimer's disease

TNFα = tumour necrosis factor α, *IL* = interleukin, *iNOS* = inducible nitric oxide synthase

In response to the presence of chronic inflammatory stimuli such as amyloid beta aggregates, microglia and astrocytes become activated. This triggers the release of proinflammatory cytokines, chemokines, and reactive oxygen species, an overproduction of which can result in neurodegeneration.

In transgenic mouse models of AD, microglial activation in early disease can help with the clearance of Aβ deposits.[54] It is possible that microglial activation is beneficial in early disease but becomes detrimental in later stages. Microglial activation relies on

the identification of inflammatory stimuli through various membrane pattern-recognising receptors (PRR).

AD patients have elevated levels of proinflammatory cytokines and chemokines such as TNFα, IL-1β, and IL-6 in their brain and CSF.[55,56] Further evidence of the role of neuroinflammation in AD comes from GWAS studies that have identified several genetic risk factors such as TREM2, CLU, CR1 and CD33, all of which are involved in the innate immune system.[57] Furthermore, the dysregulation of the complement protein system in AD, an integral component of the innate immune system, is believed to contribute to the neurotoxic effects of microglia and astrocytes,[58] as well as cause direct damage through its cytotoxic effector, the membrane attack complex.[59]

Aβ aggregates interact with cells through several mechanisms, including non-specific biophysical interactions with cell membranes resulting in a loss of normal barrier function, and specific receptor-mediated interactions on the cell membrane.[60–63] The heterogeneity of Aβ aggregates makes them a diverse ligand for a wide range of possible receptors.[64,65] Over 20 candidates have been proposed, including cellular prion protein,[66] nicotinic acetylcholine receptors,[67] glutamate receptors such as AMPA, NMDA and mGluR5,[68–70] TREM2,[71] ApoE,[72] and toll-like receptors 2 and 4.[73–75] These varied Aβ-receptor interactions are likely to be contributing to synaptic dysfunction and neurodegeneration.[65] The toll-like receptor interactions are of particular interest due to their critical role in neuroinflammation.

1.4. Toll-like Receptors

The Toll-like receptor family plays a central role in the innate immune response by recognising pathogen-associated molecular patterns (PAMPs) and DAMPs. In the brain, these receptors are mostly found in glial cells, namely microglia and astrocytes,[76] but have also been reported in less abundance in neurons.[77] TLR4, a member of this receptor family, has been strongly implicated with AD pathology.[74] Like other toll-like receptors, TLR4 is activated via ligand-induced dimerisation, mediated by membrane-anchored co-receptor proteins (e.g. CD14) and cytoplasmic Toll/Interleukin-1 receptor (TIR) domain-containing adaptor proteins (e.g. Mal, MyD88). This leads to a downstream signalling cascade, causing the translocation of transcription factors into the nucleus, resulting in proinflammatory cytokine and

chemokine production (**Figure 5**). One of these cytokines, tumour necrosis factor α (TNFα), plays a central role in neuroinflammation and AD pathology.

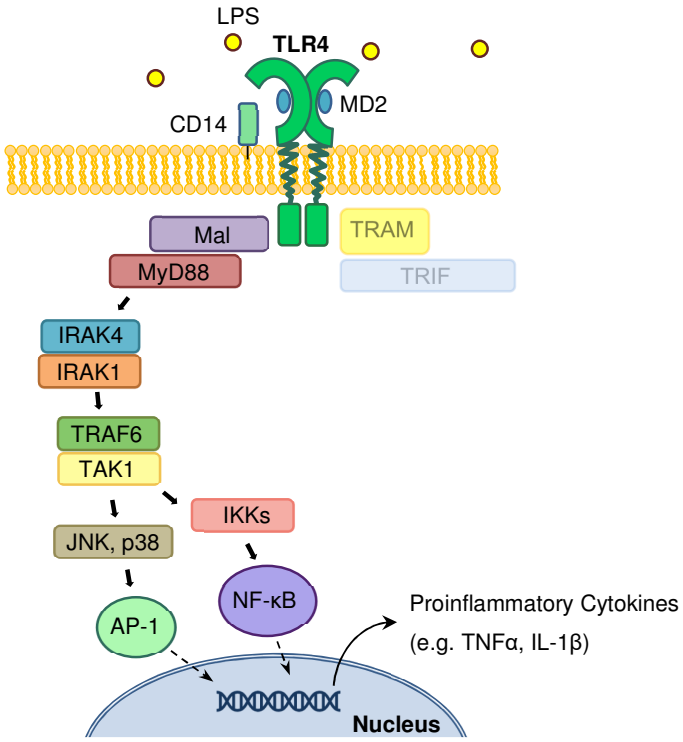

Figure 5: TLR4 MyD88-dependent signalling (simplified)

LPS = lipopolysaccharide, *TLR4* = toll like receptor 4, *CD14* = cluster of differentiation 14, *MyD88* = myeloid differentiation primary response 88, *IRAK* = interleukin-1 receptor-associated kinase, *TRAF6* = TNF receptor-associated factor 6, *TAK1* = transforming growth factor β-activated kinase 1, *JNK* = c-Jun N-terminal kinase, *IKK* = inhibitor of nuclear factor-kB kinase, *AP-1* = activator protein 1, *NF-κB* = nuclear factor kappa-light-chain-enhancer of activated B cells.

The recognition and binding of LPS or other PAMPs causes the dimerisation of the TLR4 receptor. Mediated by the CD14 co-receptor, the MyD88-dependent pathway recruits several proteins involving IRAKs, TRAFs, IKKs, JNK and p38, which cause the translocation of transcription factors NF-κB and AP-1 to the nucleus. This leads to the production of proinflammatory cytokines and chemokines.

1.5. Tumour Necrosis Factor (TNF)α

TNFα is an inflammatory cytokine secreted by activated macrophages/monocytes in response to inflammatory stimuli such as PAMPs. Most TNFα production occurs from the TLR4 MyD88-dependent downstream signalling cascade involving nuclear factor kappa-light-chain-enhancer of activated B cells (NF-κB) translocation to the nucleus (**Figure 5**).[78] TNFα can also be produced by the TLR4 MyD88-independent late activation of NF-κB, from other members of the TLR family, and from TNFR1 and TNFR2 signalling. Newly synthesised TNFα is trafficked from the Golgi apparatus to the cell membrane where it is cleaved by the TNFa-converting enzyme (TACE) ADAM17, a member of the ADAM family of disintegrin proteinases.[75,79] Upon cleavage, this type 2 transmembrane protein (25.6 kDa) releases a soluble trimeric cytokine (17 kDa) that binds to several receptors, namely tumour necrosis factor receptor 1 (TNFR1) and TNFR2.[80] TNFR1 contains a death-domain (DD) and typically carries out pro-apoptotic effects.[81] TNFR2, which does not have a DD, is involved with promoting cell survival and proliferation, as well as pro-inflammatory cytokine production.[82] This is done through the activation of cellular inhibitors of apoptosis 1 and 2,[83] NF-κB,[84] and phosphatidylinositol 3-kinase-dependent signalling pathways.[85,86]

Under physiological conditions, TNFα helps regulate the cells of the immune system, as well as support synaptic transmission and plasticity.[87,88] However, in disease conditions TNFα forms a positive feed-back loop resulting in elevated levels of TNFα, which have been shown to enhance Aβ production,[89,90] decrease microglial clearance of Aβ,[91] increase neuronal cell death,[92] and are associated with cognitive decline (**Figure 6**).[82,93] These effects likely arise from a combination of mechanisms, including the direct binding of TNFα proteins to receptors on neurons (e.g. TNFR1 and 2), and the recruitment and activation of astrocytes, which in turn release a variety of toxins (e.g. transforming growth factor-β (TGFβ)) that have been implicated in AD pathology.[94]

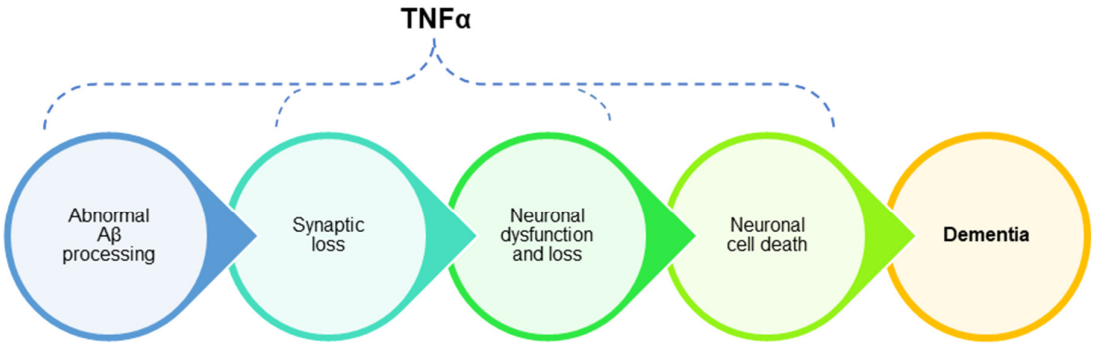

Figure 6: Toxic effects of TNFα

Overproduction of TNFα can lead to several toxic effects, including the abnormal processing of the Aβ peptide, the loss of synaptic connections, neuronal dysfunction and loss, as well as neuronal cell death. These toxic effects can lead to dementia.

Abnormal Aβ clearance may also be caused by TNFα, possibly through irregular cleavage of APP via the mitogen-activated protein kinase (MAPK) pathway[90] and through NF-κB signalling.[26] AD patients have significantly higher levels of TNFα in their blood[96] and central nervous system[97] than healthy adults, which correlates with disease progression.[98] In post-mortem human AD brains, TNFα has been found localised around amyloid plaques.[99] TNFR1 signalling is required for Aβ-induced neuronal death.[100] Single-cell experiments have identified that paracrine signalling is important for regulating macrophage responses to TLR4 stimulation.[101] It should be noted that as well as the production of TNFα, TLR4 activation can cause the priming of inflammasomes (e.g. nLRP3, nLRC4, AIM2); multimeric protein complexes that assemble in the cytosol, which can produce IL1β and IL-18 via caspase-1 activation.[102] IL1β is believed to play an important role in the initiation and propagation of neuroinflammation in AD, by providing a robust activation of astrocytes and microglia.[103,104] IL1β is also thought to contribute to neuronal and synaptic dysfunction through several possible mechanisms, including the modulation of β-APP mRNA processing,[105] and tau hyperphosphorylation.[106,107]

Along with playing an integral role in neuroinflammation, proinflammatory cytokines such as TNFα can cause high levels of excitotoxicity (**Figure 7**).[108] Excitotoxicity occurs from the excessive stimulation of excitatory neurotransmitters such as glutamate, which can lead to the production of ROS, resulting in neuronal toxicity and cell death.

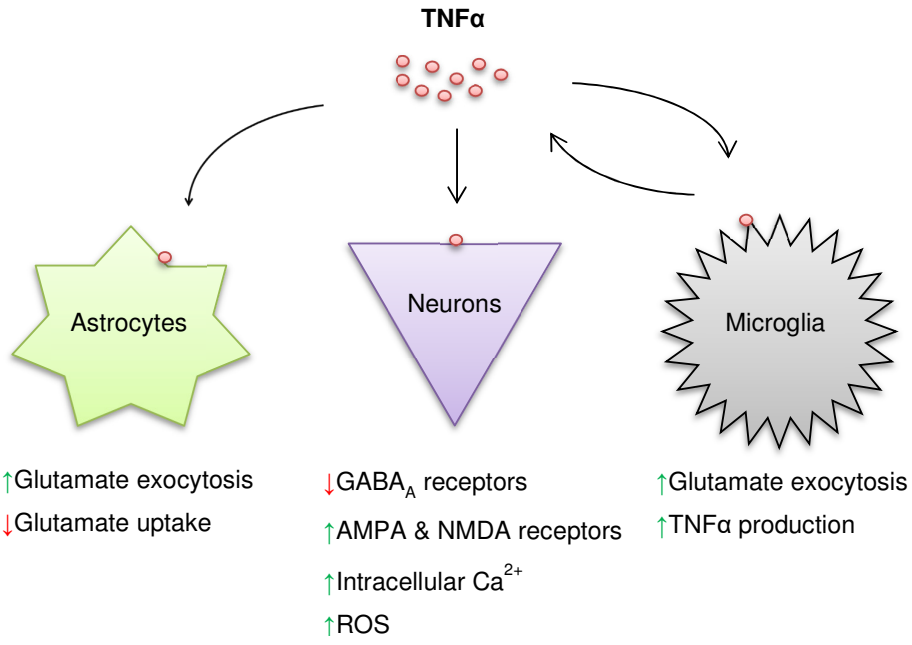

Figure 7: The excitotoxic effects of TNFα

TNFα is produced and released from microglia, which feeds back and stimulates further TNFα production. This promotes an extracellular release of glutamate from microglia and astrocytes, while inhibiting astrocytic glutamate uptake. In neurons, TNFα decreases the expression of inhibitory receptors, while activating excitatory receptors. This causes an influx of intracellular Ca^{2+}, leading to the production of ROS.

In the presence of interferon (IFN)-γ from T-cells, effector cells such as microglia secrete TNFα. This leads to glutamate release from gap junctions on the microglial membrane. TNFα also stimulates the microglial TNFR1, which produces even more TNFα, creating a positive feedback loop. This results in the stimulation of the TNFR1 receptor on astrocytes, causing glutamate exocytosis, while inhibiting glutamate uptake. In neurons, excitatory receptors AMPA and NMDA are activated, while inhibitory $GABA_A$ receptors are supressed. This leads to a net increase of extracellular glutamate, resulting in an influx of Ca^{2+} in neurons. The consequent mitochondrial

calcium overload causes the production of ROS, resulting in the degeneration of neurons. Neuronal cell death further induces the microglial release of proinflammatory cytokines such as TNFα.[108]

1.6. Triggering Receptor Expressed on Myeloid Cells 2 (TREM2)

Recent genome-wide association studies (GWAS) have identified TREM2, a gene involved in microglial inflammation, as a strong correlate with late onset AD pathology.[109] Patients with a rare variant causing partial loss of TREM2, p.Arg47His (rs75932628), have a two-to-four time increase in risk of developing AD.[110,111] Loss of function TREM2 variants affect the way microglial cells respond to inflammatory stressors, such as amyloid beta,[112] resulting in impaired amyloid clearance. TREM2 can bind to Aβ aggregates directly, which affects microglial responses.[113] In TREM2 variant AD, microglial cells stop undergoing apoptosis, and instead undergo senescence. Less microglia are also present around plaques and there are elevated levels of tau protein. In TREM2 variant AD, there is more insoluble tau than Aβ.[53] TREM2 plays a role in preventing tau seeding in neuritic plaques.[114] TREM2 is cleaved by α-secretases ADAM10 and ADAM17, resulting in ectodomain shedding, which releases soluble TREM2 into the extracellular space. This is followed by further cleavage of the C-terminus by γ-secretase (**Figure 8**).[115,116] Soluble TREM2 in CSF is a potential biomarker for disease progression from early AD to dementia, since it is elevated in AD patients and has significant changes with disease progression.[117–119] In addition, TREM2 has been shown to have reciprocal inhibition with TLR4, further supporting TREM2's role in regulating neuroinflammation.[120,121]

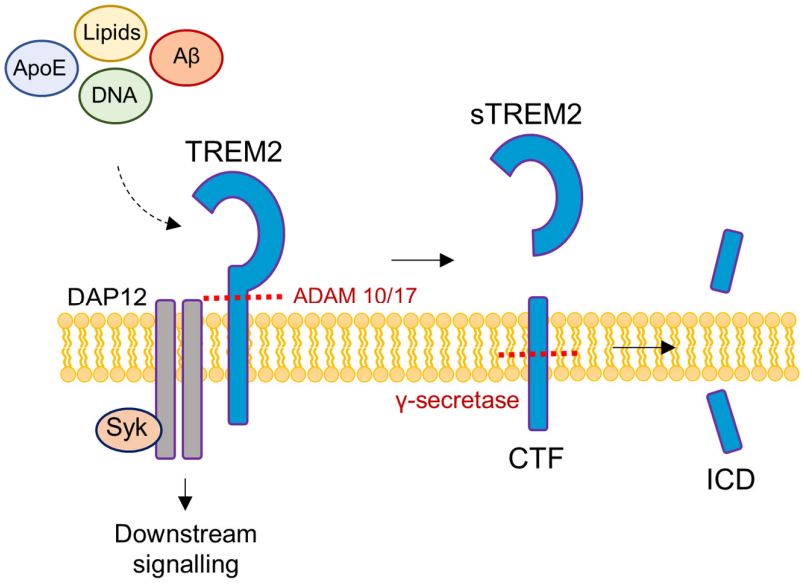

Figure 8: TREM2 cleavage

TREM2 is cleaved by α-secretases ADAM 10 and/or ADAM 17, which releases soluble TREM2 into the extracellular space. This is followed by further intramembrane cleavage of CTF, which releases the intracellular domain (ICD) into the cytosol. Membrane TREM2 can recognise several ligands such as lipids, Aβ, ApoE and DNA, which cause signalling through DAP12 and regulate microglial activity.

1.7. Therapies and Prevention Strategies

AD is a multifaceted disease, with a vast array of potential therapeutic targets. This has made it very challenging for the pharmaceutical industry to develop an effective therapy or preventative treatment. Currently, only drugs that provide symptomatic relief are commercially available, including acetylcholinesterase inhibitors, such as donepezil, galantamine and rivastigmine, and NMDA receptor blockers such as memantine.[122,123] However, as important as these drugs are for improving the quality of life of AD patients, they do not prevent or stop disease progression.

In the past, pharmaceutical companies have tried a variety of disease-modifying therapies that aimed to slow the pathogenic process. In 1999, the first case of active immunotherapy against AD was published. This active vaccination was aimed at clearing Aβ from the brain of AD patients, by making the individuals generate their own antibodies to the amyloid beta antigen in the vaccine. However, 6% of the patients involved in the study developed severe meningoencephalitis,[124] so other avenues were explored.

A crucial rate-limiting step for most neurodegeneration treatments has been the permeablisation of the BBB. The BBB is a network of proteins and endothelial cells that form a semi-permeable membrane that coats capillaries in the brain and prevents the passage of larger molecules into the brain tissue. The BBB is virtually impermeable to biologics due to their size (1-200 kDa), and only a small fraction (< 2%) of small molecule drugs (< 1 kDa) can pass through. Lipid-mediated free diffusion across the BBB requires lipid solubility and a molecular weight less than 400 Da.[125,126] Fortunately, pharmaceutical companies have been developing new ways of crossing the BBB. One promising method relies on fusing the drug with an endogenous peptide that undergoes receptor-mediated transport, most commonly using transferrin or insulin receptors.[82,127] For larger drugs such as biologics, Roche has recently published the 'Brain Shuttle' for transporting antibodies through the BBB.[128]

Small molecule drugs have been tested against a wide range of therapeutic targets. These drugs are less target-specific than biologics, but have better distribution, cell permeabilisation, and can be administered orally. One of the major targets for intervention using small molecule drugs has been γ-secretase, the enzyme involved in the amyloidogenic cleavage of APP. However, many challenges emerged from this target as γ-secretase is responsible for the cleavage of over 50 other proteins. Additionally, it is an important regulator of the proteolysis of Notch.[129] Perturbing these physiological processes has led to severe adverse effects from γ-secretase inhibitors such as Semagacestat and Avagacestat.[130,131] A more recent development focuses on the modulation of γ-secretase rather than inhibition, shifting the cleavage of APP towards the production of less toxic Aβ peptides. Currently in Phase II clinical trials, the γ-secretase modulator EVP-0962 has shown promise, as downstream effects such as Notch cleavage remain unaltered.[122] Small molecule drugs have also been created to target BACE1, the first enzyme to cleave APP. However, Merck's Verubecestat caused an increased risk of adverse effects[132] and Lanabecestat developed by AstraZeneca in partnership with Eli Lilly and Company, failed in Phase III clinical trials for not meeting its primary endpoints.[133] Other BACE inhibitors failed due to low BBB penetration, as well as causing liver toxicity.[134] Further targets for intervention include Aβ-degrading proteases (Aβ-DPs), seeing as Aβ is continuously being degraded and produced in the brain.[135] Improving degradation rates is one approach; inhibiting the inhibitors of Aβ-DPs is another.

More recently, there has been a shift towards passive immunotherapy.[136] Monoclonal antibodies have the advantage of having high specificity, high affinity and low toxicity. These antibodies have been used for targeting hyperphosphorylated tau, microglial activation and Aβ aggregation. Many Aβ antibodies target the N-terminus of the protein, which is free in both monomeric and fibrillar forms. However, binding to the N-terminus does not appear to provide therapeutic benefits. Antibodies such as Solanezumab,[137,138] Crenezumab[139] and Gantenerumab[140] have been designed to bind to the central epitope of Aβ42, however Solanezumab trials have failed and closed, and initial trials for the other two have failed so far. Despite this, two Phase II Crenezumab trials and three Phase III Gantenerumab trials are currently ongoing.[141] One of the major challenges in this area is trying to develop an antibody that binds specifically to the soluble early aggregates, which are believed to be the most cytotoxic. Due to the heterogeneity of Aβ assembly, it remains unclear whether the C-terminus is free in these early aggregates. BAN2401, currently in Phase III clinical trials, is believed to bind specifically to protofibrils.[142] The pharmaceutical company Biogen took a different approach with aducanumab, a monoclonal antibody that selectively targets and dose-dependently reduces amyloid deposition, slowing down cognitive decline.[43,143] Aducanumab failed to reach its primary endpoints in the last two Phase III clinical trials, however a new Phase III trial has been started.[141]

Passive immunotherapies have also been engineered to target molecular chaperones in order to decrease the pathological aggregation of proteins. Another target is the insulin signalling pathway, since the insulin-degrading enzyme (IDE) plays a role in breaking down Aβ42, but is occupied in diabetics, preventing it from carrying out its physiological role. Other targets include microglial activation, genetic risk factors (ApoE, TREM2, APP) and inflammation. TNF inhibitors including monoclonal antibodies (e.g. Infliximab) and recombinant fusion proteins (e.g. Etanercept) have been developed to target neuroinflammation.[82]

Gene therapies are also looking promising for AD, with recent advances in adeno-associated virus (AAV) technology paving the way for new medicines.[144] One of the main advantages of gene therapy for brain diseases is that it does not need to cross the blood-brain barrier like immunotherapies or small molecule drugs. In combination with the CRISPR/Cas9 genome editing tool, several early-onset and late-onset AD gene mutations are being investigated as points of intervention.[145] A recent target for

gene therapy is CD33, which encodes for a microglial receptor, which is upregulated in AD and reduces the uptake and clearance of Aβ.[146] Targeting CD33 in a mouse model of AD with gene therapy has shown significant reduction in amyloid beta accumulation and neuroinflammation.[147] A more recent study has identified that antisense long non-coding RNA (lncRNA) can regulate and suppress production of tau in the brain.[148] Gene therapies are currently being developed to enable the delivery of this lncRNA to brain cells to ultimately reduce the production of tau and therefore tau-mediated toxicity. The first-in-human clinical trial for an AD gene therapy has recently entered Phase 1, which aims to deliver brain-derived neurotrophic factor (BDNF) packaged in an AAV to the entorhinal cortex and protect the cells from degeneration.[149] Furthermore, biotech companies such as Mogrify, are developing technologies to aid *ex vivo* cell therapies and *in vivo* reprogramming therapies, using transcriptomic switches that allow the conversion of any human cell type to any other.[150] Recent successes in gene therapy for other diseases suggest that this may also be a viable strategy for AD, however we still need a better understanding of the mechanisms underlying the disease in order to find better targets.

1.7.1. Clinical Trials

The R&D and clinical trial framework has changed drastically since the 'thalidomide disaster' of 1961, which had severe economic and regulatory ramifications on the pharmaceutical industry.[151] With a rise in drug development costs and stricter regulations for drug approval, it is becoming increasingly more difficult for pharmaceutical companies to get their drugs through clinical trials, which can take several years to decades (**Figure 9**). Moreover, prior to testing on human patients, drugs need to be tested for safety and efficacy through a variety of assays. For this reason, the preclinical testing of drugs is integral to the development of a successful therapy with minimal undesirable side effects. Chapter 3 of this thesis focuses on the development and optimisation of a neuroinflammation assay for the preclinical testing of passive immunotherapies.

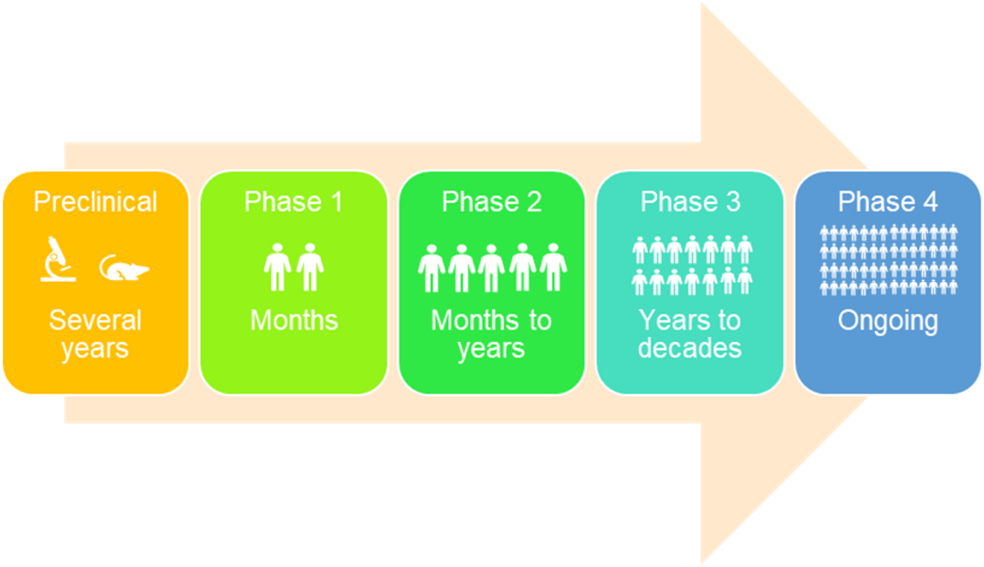

Figure 9: Schematic of clinical trial timeline

Clinical trials have a preclinical stage, which focuses on drug testing using cellular and animal models. In phases 1 – 4 of clinical trials the drug is administered to human patients. This process can take several years to decades.

1.8. Challenges for AD Therapy

Over the past three decades, there have been hundreds of failed AD clinical trials.[152] Despite our increased understanding of the disease pathology, there is still no drug that can stop or prevent disease progression. This is attributed to the disease's multifaceted nature, with pathophysiological changes, symptoms and prevalence, varying greatly from patient to patient. This is further complicated by the fact that the majority of AD cases are expected to be mixed dementias, with the presence of neurodegenerative co-pathologies that include cerebrovascular disease and Lewy body disease.[153] In fact, up to 33% of AD cases may have Lewy related pathology.[154,155] In addition, diseases such as primary age-related tauopathies (PART), which are commonly observed in elderly patients, have similar neurofibrillar pathology to AD, increasing the challenge of AD diagnosis.[156] Furthermore, AD has a long asymptomatic preclinical phase, where patients might not show cognitive dysfunction but can still have the disease.[155,157] More reliable biomarkers and diagnostic tools are required in order to properly diagnose AD, as the distinction between healthy aging and preclinical AD remains unclear. Earlier intervention with existing therapeutics is currently under consideration.[158] Moreover, a lack of follow up

of cognitive ability of patients (i.e. 10 years) after treatment could be contributing to the pre-emptive disqualification of some drugs from reaching the market.

The complexity of AD and in fact all neurodegenerative diseases, make it very challenging to find good therapeutic targets. Protein targets are often present in multiple cell types with varying biological roles, so alterations to the target will often result in unwanted side effects. Fortunately, new methods for identifying cell-type-specific targets are on the rise. One example is Cerevance's Nuclear Enriched Transcript Sort sequencing (NETSseq) platform, which uses immunohistochemistry of human brain tissue to detect specific cell types, and then sorting their nuclei and performing RNA sequencing.[159] This allows for the measurement of the expression of cell-type-specific genes, which has already lead to the discovery of several therapeutic targets for neurodegenerative diseases.

Animal models of the disease, including mice, non-human primates, fruit flies, roundworms, and zebrafish, are commonly used in AD research, as they offer the advantage of allowing preclinical testing *in vivo*. They also allow for cognitive behavioural testing at more sensitive levels than would be possible with human patients. However, it is unclear how accurately these animal models reflect the actual disease pathology, as AD is a uniquely human disease. Genetic intervention is required to get these animal models to mimic the disease, and with most drugs being unsuccessful in clinical trials, the gold standard is working with human cells and tissue.[160]

Recent advances in iPSC models of disease have enabled direct differentiation of iPSCs into various types of brain cells including neurons, astrocytes, microglia, oligodendrocytes, endothelial cells, and pericytes.[161] Cells taken directly from AD patients have given rise to models with endogenous gene expression in vulnerable cell types. Furthermore, genetic manipulation with CRISPR/Cas9 allows for the insertion or removal of AD-specific mutations. The use of mass spectrometry in tandem with iPSC models has provided unprecedented insights into the regulation of specific proteins such as tau and APP/Aβ, and has enabled further validation of these models.[162] Co-cultures of different cell types can help capture the complex interactions between cells, and iPSCs can even be grown in 3D cultures that can generate hallmark AD pathologies.[163–166] Developments in iPSC differentiation protocols, improvements

in the reproducibility of iPSC-derived cell types, and the emergence of increasingly complex 3D co-culture systems, are giving rise to progressively better models of AD.[161]

1.9. Sourcing clinically relevant aggregates

It is widely accepted that small soluble Aβ42 aggregates are toxic through a variety of mechanisms, including the permeabilisation of cell membranes through non-specific binding, and by specific binding to pattern-recognising membrane receptors.[60–63] This can lead to microglial activation and inflammation,[167] a key player in AD pathology.[93,168] Microglial activation increases as the disease progresses, and they become dystrophic at late stages.[53] Through these toxic mechanisms, Aβ42 aggregates have been shown to cause neuronal cell death, synaptic dysfunction, as well as cognitive impairment in AD patients and animal models of AD.[36,37,177,169–176]

Despite only being a small subset of the overall protein aggregates found in brain tissue, it is believed that the soluble aggregates are responsible for most of the toxicity.[178] Soluble aggregates have been found in the brain lysates of AD

patients.[179–181] However, these soluble aggregates occur at low concentrations and hence have been poorly characterised due to a lack of sensitive methods, with many more studies performed on synthetic or recombinant aggregates, since they are available in higher concentrations.[182] It is still unclear how comparable endogenous aggregates from AD patients are to synthetic aggregates or to those from animal models.[183,184] Far less research has been done on the aggregates in human CSF or extracted from post-mortem brain. Brain samples are generally homogenised and hence include large amounts of insoluble aggregates, which are largely inert, as well as soluble aggregates potentially complicating the interpretation of any analysis.

To address these issues, there has been a recent effort to selectively extract the soluble aggregates from human brain tissue using minimally perturbative methods.[178,185] The Klenerman group has previously developed a suite of sensitive methods with the potential to characterise aggregates and measure their properties.[167] These include size-separation of aggregates in these samples and measure their properties as demonstrated by experiments on CSF from AD patients.[186] Soluble aggregate samples have previously been found to contain Aβ42 aggregates as

identified through western blotting, and can cause neurite length retraction on iPSC-derived neurons, as well as block synaptic LTP.[178,187] Furthermore, they can induce neuronal hyperactivation in mouse CA1 hippocampal neurons, as seen with two photon Ca^{2+} imaging.[188,189] Soluble aggregate-induced toxicity is believed to be mediated partly by prion protein (PrP).[190] However, there is no information about the size, structure, or inflammatory potential of the soluble aggregates extracted by soaking post-mortem brain nor how the aggregates differ between different brain regions. Chapter 4 of this thesis explores the implementation of our sensitive techniques to characterise soluble aggregates from early AD brains.

1.10. Project aims

Currently, there is no therapy or preventative strategy for AD. This is partly due to our limited understanding of the endogenous soluble aggregates in AD patients and their role in neuroinflammation, a key player in AD pathology.

The aim of the first project (chapter 3) was to optimise a neuroinflammation assay that would test the inflammatory potential of toxic Aβ aggregates, using a BV2 microglial cell line. In conjunction with a liposome-permeability assay and an immunoprecipitation assay, this assay would act as a platform for the preclinical testing of passive immunotherapies, including a proprietary anti-Aβ42 antibody from MedImmune (now AstraZeneca).

Most neuroinflammation studies have focused extensively on synthetic Aβ, and to a much lesser extent CSF or homogenised brain samples, which do not distinguish between soluble or insoluble aggregates.

Therefore, the aim of the second project (Chapter 4) was to characterise the endogenous soluble aggregates from early AD patients, extracted through soaking brain tissue in artificial CSF buffer. Their size, morphology, inflammatory potential, neurotoxicity, and ability to permeate a lipid membrane, would be characterised using the neuroinflammation assay described in Chapter 3, a neurite-retraction assay, a liposome-permeability assay, AD-PAINT, AFM, and single-molecule pull-down (SiMPull) imaging. To assess regional variability in the brains of AD patients, soluble aggregates would be extracted from eight different regions. A better understanding of these aggregates and their mechanisms of action could shed some light on the events

occurring in early AD and could lead to the identification of potential novel therapeutic targets.

2: Materials & Methods

2.1. Sources of Aβ42

Table 1: Sources of synthetic or recombinant Aβ42

Supplier	Buffer	Cat. Code	Synthetic/recombinant	Purification
AnaSpec	SSPE	AS-20276	Synthetic	N/A
Bachem	NH_4OH	4014447	Synthetic	N/A
Bachem	HFIP	4014447	Synthetic	N/A
Abcam	HFIP	ab120301	Synthetic	N/A
Abcam	GuHCl	ab120301	Synthetic	FPLC
CoH	GuHCl	N/A	Recombinant	FPLC

SSPE = saline-sodium phosphate-EDTA, *NH_4OH* = ammonium hydroxide, *HFIP* = 1,1,1,3,3,3-hexafluoro-2-propanol, *GuHCl* = guanidine hydrochloride, *CoH* = Chemistry of Health (Department of Chemistry, Cambridge), *N/A* = not applicable

2.2. Preparation of synthetic Aβ42

2.2.1. AnaSpec - SSPE

AnaSpec Aβ42 was prepared as described previously.[191–193] Briefly, lyophilised peptides were dissolved in saline-sodium phosphate-EDTA (SSPE) buffer (150 mM NaCL, 10 mM $Na_2H_2PO_4$ x H_2O and 10 mM Na_2EDTA), adjusted to pH 12 using NaOH. This was followed by 30 min of sonication over ice (Bandelin Sonorex, Berlin, Germany) and then flash freezing into 10 µL aliquots.

2.2.2. Bachem – NH_4OH

Bachem Aβ42 was prepared following manufacturer's instructions. The peptide was dissolved in 1% v/v NH_4OH/PBS and then diluted in PBS to a concentration of 100 µg/mL. This was followed by vortexing gently for 1 min, then flash freezing into 10 µL aliquots.

2.2.3. Bachem & Abcam - HFIP

Abcam and Bachem Aβ42 were dissolved in HFIP and vortexed gently. The solution was then dried under a nitrogen stream, re-dissolved in 100% HFIP to a concentration of 1 mg/mL. After a 5-min sonication, they were dried under a nitrogen stream. The HFIP treatment was then repeated two more times and left to dry overnight in the fume hood. The samples were then flash frozen and split into 10 µL aliquots.

2.2.4. Abcam - GuHCl

Abcam Aβ42 lyophilised powder was dissolved in 6 M GuHCl and purified using a Superdex 75 10/300 GL column (GE Healthcare Bio-Sciences AB SE-751 84 Uppsala, Sweden), as previously described.[194–196] This was carried out by Dr. Patrick Flagmeier. Protein concentration was then measured using a BCA assay.

2.3. Preparation and purification of recombinant Aβ42

Recombinant Aβ42 (MDAEFRHDSGYEVHHQKLVFFAEDVGSNKGAIIGLMVGGVVIA) was expressed in the *Escherichia coli* BL21 Gold (DE3) strain and purified as described previously.[194] This was done by members of the Chemistry of Health building, Cambridge. Monomeric Aβ42 was dissolved in 6 M GuHCl, then purified using a Superdex 75 10/300 GL column, as previously described.[195,196] This was carried out by Dr. Patrick Flagmeier. Protein concentration was then measured using a BCA assay.

2.4. Measuring Aβ42 aggregation kinetics

Aggregation kinetics of the recombinant Aβ42 were measured using Thioflavin T (ThT), a benzothiazole salt amyloidophilic dye that fluoresces when bound to beta-sheet structures.[197] Samples of Aβ42 monomer were diluted in phosphate-buffered saline (PBS) and added to 20 µM ThT in low-binding Eppendorf tubes (Eppendorf AG, Hamburg, Germany). The samples were prepared on ice, to prevent any protein self-assembly, and pipetted into a 96-well half-area, clear-bottom, low-binding polyethylene glycol coating plate (Corning 3881, Kennebuck ME, USA). The samples were loaded at 80 µL per well, at different concentrations of protein (usually 10 µM, 5 µM, 2 µM, and 0 µM). The plate was then placed in a plate reader (Fluostar Omega; BMG Labtech, Ortenberg, Germany) at 37 °C, under quiescent conditions. Measurements were taken using the bottom reading mode (440nm excitation filter, 480nm emission filter). Aggregation of Aβ42 for neuroinflammation and liposome

experiments was carried out in the plate reader in the same manner, excluding the addition of ThT, for desired times based on the previous ThT kinetics curves.

2.5. AD brain tissue

Fresh frozen brains from AD patients and non-AD controls (**Table 2**) were received whole from the Addenbrooke's post mortem room, or from other centres around the country. Transport and consent details were reviewed and handled by the Cambridge Brain Bank. Processing of tissue was carried out in Addenbrooke's hospital, where regions of interest were removed from the left cerebral hemisphere and frozen at -80 °C. The AD brains analysed in this study were diagnosed as being Braak stage III by histopathologists, based on tau protein pathology.

2.5.1. Extraction of soluble aggregates from human brain tissue

Soluble aggregates were obtained by following a previously established protocol with a few adaptations.[178] Briefly, human brain tissue was chopped into 300 mg pieces using a razor blade and incubated with gentle agitation in 1.5 mL of artificial cerebrospinal fluid (aCSF) buffer (124 mM NaCl, 2.8 mM KCl, 1.25 mM NaH_2PO_4, 26 mM $NaHCO_3$; pH 7.4, supplemented with 5 mM EDTA, 1 mM EGTA, 5 µg/mL leupeptin, 5 µg/mL aprotinin, 2 µg/mL pepstatin, 20 µg/mL Pefabloc, 5 mM NaF) at 4 °C for 30 min. Samples were centrifuged at 2,000 $g_{(av)}$ at 4 °C for 10 min and the upper 90% of the supernatant was collected and centrifuged at 14,000 $g_{(av)}$ for 110 min at 4 °C. The upper 90% of the supernatant was extracted and dialysed using Slide-A-Lyzer™ cassettes (Thermo Scientific, Cat. 66330) with a 2 kDa molecular weight cut off, against 100-fold excess of fresh aCSF buffer with gentle agitation at 4 °C. Buffer was changed three times over the course of 72 hr dialysis. The prep was carried out under sterile conditions, using autoclaved LoBind Eppendorf tubes and pre-sterilised pipette tips to reduce endotoxin contamination. Samples were aliquoted into small volumes, snap frozen and stored in a -80 °C freezer and thawed only once prior to experimentation. This was optimised initially by me and Helen Dakin at Addenbrooke's hospital and was then carried out solely by Helen for future batches.

2.5.2. Patient Information

Table 2: Patient information & neuropathologic change scoring

Patient Information							AD Neuropathologic Change (ABC Score)		
Patient	**ID No.**	**Age at PM**	**PMI (hrs)**	**Gender (M/F)**	**Cause of Death**	**Braak Stage**	**A Stain for Aβ/ amyloid plaques**	**B Stain for NFTs**	**C Stain for NPs**
AD1	NP17 -216	77	55	F	Burkitt's Lymphoma	III	2	3	1
AD2	NP17 -194	71	70	M	Pneumonia	III	0	2	0
AD3	NP17 -020	88	44	M	End stage dementia	III	1	3	1
Control	NP17 -256	72	-	F	Malignant tumour of spinal cord	-	0	1	0

AD = Alzheimer's disease, *C* = control (non-AD), *PM* = post-mortem, *PMI* = post-mortem interval, *M* = Male, *F* = Female, *NFT* = Neurofibrillary tangles, *NP* = Neuritic plaques.

Information from three Braak stage III AD patients and one non-AD patient whose brain tissue has been analysed in this study. Neuropathologic scoring is defined according to the National Institute on Aging – Alzheimer's Association guidelines.[198]

2.6. Neuroinflammation assay

2.6.1. Cell culture

BV2 cells derived from immortalised murine neonatal microglia (European Collection of Authenticated Cell Cultures) and immortalised wild type and TLR4$^{-/-}$ (NR-9458) macrophage cell lines (BEI Resources, USA), were all grown in T25 flasks in Dulbecco's modified eagle medium (DMEM) (Gibco, Life Technologies, Cat. 21063-029) with 10% v/v foetal bovine serum (FBS) (Sigma-Aldrich, St. Louis, MO, Cat. F0926), 100 U/mL penicillin/100 µg/mL streptomycin (Gibco, Life Technologies, Cat. 15140-122), 2 mM L-glutamine (Gibco, Life Technologies, Cat. 25030-024), 1% v/v sodium pyruvate and 1% v/v HEPES buffer. They were grown in a humidified environment, incubated at 37 °C, with 5% CO_2, 95% air. Filtered pipette tips were used throughout, that were sterile, and RNAase, DNAase, DNA and pyrogen free (STARLAB, S1126-7810). Cells were not used for experimentation past passage 8 to increase reproducibility of data.

2.6.2. Synthetic Aβ42 neuroinflammation

Cells were plated in flat-bottom 48-well plates (Corning, Costar, Cat. 10065370) in DMEM (10% v/v FBS) at a density of 50,000 cells/well (300 µL per well). 24 hr after plating, the cells were washed with fresh pre-warmed (37 °C) media and kept in phenol red-containing DMEM 1% v/v FBS. Cells were treated with aggregated synthetic Aβ (Abcam) in a 1:4 dilution. LPS (Invivogen San Diego, CA, Cat. Tlrl-3pelps) at 10 ng/mL was used as a positive control. PBS in a 1:4 dilution was used as a vehicle control. The supernatant was collected every 24 hr for analysis and the wells were washed with fresh media and replaced with fresh solution. The supernatant was stored in a -80 °C freezer and thawed only once before being measured with a mouse TNFα DuoSet ELISA (R&D Systems, MN, USA, Cat. DY410) using a plate reader (CLARIOstar, BMG Labtech, Ortenberg, Germany) at 450 nm. Experiments were carried out over 24-120 hr. Three wells were used for each condition to estimate variation.

2.6.3. Brain-derived soluble aggregate neuroinflammation

Cells were plated in flat-bottom 96-well plates (Corning, Costar, Cat. CLS3997) in DMEM (10% v/v FBS) at a density of 25,000 cells/well (150 µL per well). 24 hr after plating, the cells were washed with fresh pre-warmed (37 °C) media and kept in phenol red-containing DMEM 1% v/v FBS. Cells were treated with soluble aggregates in a 1:5 dilution. LPS at 10 ng/mL was used as a positive control and aCSF buffer in a 1:5 dilution was used as a vehicle control. The supernatant was collected every 24 hr for analysis and the wells were washed with fresh media and replaced with fresh solution. The supernatant was stored in a -80 °C freezer and thawed only once before being measured with a mouse TNFα DuoSet ELISA using a plate reader at 450 nm. Experiments were carried out over 96-120 hr. Three wells were used for each sample of soluble aggregates to estimate variation.

2.7. Cytotoxicity measurements

Cell supernatant collected from the neuroinflammation assay (BV2 cells) was stored at -80 °C. A lactate dehydrogenase (LDH) assay (Abcam, Colorimetric, Cat. ab102526) was used to detect the concentration of LDH (mU/mL) in the supernatants. Cells treated with RIPA lysis buffer (Thermo Scientific, Cat. 89900) were reported as 100% cytotoxicity (100%), whereas vehicle control cells of the same density were

reported as 0% cytotoxicity. The supernatants were thawed only once before taking measurements.

2.8. Preparation of cells for TNFα imaging

This assay was based on previously established protocols, with several adaptations made to accommodate our BV2 cell line.[199,200] Briefly, BV2 cells were plated at 200,000 cells/mL on imaging slides (Ibidi, µ-Slide 4 well, Cat. 80426), 700 µL per well. They were then treated with 50 ng/mL LPS and 1 µM TNFα protease inhibitor-0 (TAPI-0) for 2 hr, followed by fixation using 2% v/v paraformaldehyde (PFA) for 20 min at 4 °C. The cells were then blocked with blocking solution (PBS with 0.5% w/v BSA, 4 µg/mL rat anti-mouse CD16/32 [Insight Biotechnology, FCγ II/III receptor block, Cat. 553141], 5% v/v rabbit serum [Gibco, Cat. 16120099]) for 2 hr at room temp. Cells were then stained with 10 µg/mL rat anti-mouse TNFα antibody Alexa Fluor® 647 antibody (BioLegend, Clone MP6-XT22, Cat. 506314) and washed four times with PBS before imaging.

2.9. Immunoprecipitation experiments

2.9.1. Synthetic Aβ42

Immunoprecipitation was carried out as described previously, with a few adaptations.[201] Briefly, Dynabeads® Protein A (Invitrogen, Cat. 10002D) and Dynabeads® Protein G (Invitrogen, Cat. 10004D), were mixed in a 1:1 ratio in low-binding eppendorfs (Eppendorf AG, Hamburg, Germany), in conjunction with the proprietary MedImmune antibody and isotype control antibody (NIP-228), to pull down Aβ. The MedImmune antibody was added at a concentration of 0.2 nM and 20 nM, and NIP-228 at 20 nM to 2 nM monomeric Aβ (Abcam, GuHCl). Free-Aβ in solution was measured using an amyloid beta 42 human ELISA kit (Invitrogen, KHB3441).

2.9.2. Soluble aggregate samples

Immunoprecipitation with soluble aggregate samples was similar to using synthetic Aβ, with a few adaptations. Briefly, Dynabeads® Protein A and Dynabeads® Protein G were mixed in a 1:1 ratio in low-binding eppendorfs, in conjunction with an APP-binding antibody (6E10, Mouse IgG1, Biolegend, Cat. SIG-39320) and isotype control antibody (Ultra-LEAF™, MG1-45, Biolegend, Cat. 401408) to pull down Aβ-containing fragments. The antibodies were added at a concentration of 20 µg/mL. 400 µL of soluble aggregate samples from the HPC and VAC regions were then added to the

mix. The eppendorfs were placed on a magnetic rack to pull down the magnetic beads, along with the antibody and binding targets. The neuroinflammation assay was then carried out on soluble aggregates with or without immunodepletion of Aβ-containing fragments.

2.9.3. Antibodies used for immunoprecipitation experiments

Table 3: Antibody information

Antibody	Type	Target	Host species	Species reactivity	Buffer	Source
Abet0380-GL (MedImmune antibody)	IgG_1	Aβ 1-42	Human	Human	25 mM Histidine, 7% sucrose, pH 6.0	MedImmune
NIP228	IgG_1	Isotype control	Human	Human	25 mM Histidine, 7% sucrose, pH 6.0	MedImmune
6E10	IgG_1	APP or Aβ 1-16	Mouse	Human	PBS	BioLegend
MG1-45	IgG_1	Isotype control	Mouse	Human	PBS	BioLegend
4G8	IgG_{2b}	Aβ 17-24	Mouse	Human, dog	PBS	BioLegend
A15126D	IgG_{2b}	α-synuclein 117-122	Mouse	Human	PBS	BioLegend

Table of the antibodies used for immunoprecipitation experiments.

2.10. Neurite retraction assay

2.10.1. Primary mouse hippocampal neurons

Primary mouse hippocampal neurons were extracted from mouse pups and plated in 96-well plates (IncuCyte® ImageLock, 4379) at a density of 30,000 cells/well in neurobasal media (supplemented with 1% v/v Pen/Strep, 1% v/v Glutamax, 2% v/v B27, 1% v/v N2). A 50% media change (25% fresh media, 25% sample) was carried out after 72 hr. The plate was placed in IncuCyte® S3 live cell imaging system and monitored for 84 hr. Four images were taken per well, every four hr. Neurite length was measured using NeuroTrack software with the following settings: Segmentation Mode: Brightness; Segmentation Adjustment: 1; Min Cell Width (μm): 7; Area (μm^2) min: 95; Neurite Filtering: Best; Neurite Sensitivity: 0.55; Neurite Width (μm): 1.

2.10.2. Red Lentivirus synapsin promoter

Primary mouse hippocampal neurons were transduced with the IncuCyte® Neurolight Red Lentivirus (Sartorius, 4807) following the manufacturer's instructions with a few adaptations. Briefly, the lentivirus reagent was added to the cells 4 hr after plating, followed by a 95% media replacement 24 hr later. A 50% media replacement then took place every 3 days.

2.10.3. LUHMES cells

Lund Human Mesencephalic (LUHMES) cells were purchased from the American Type Culture Collection (ATCC) (Cat. CRL-2927) and were cultured according to the ATCC guidelines. Briefly, the cells were grown in a T75 flask pre-coated with 50 µg/mL poly-L-ornithine (Sigma, Cat. P3655) and 1 µg/mL Human Fibronectin (Sigma, Cat. F-0895) in DMEM:F12 (Invitrogen, Cat. 31330038), supplemented with L-glutamine, N2 supplement (Invitrogen, Cat. 17502-048), and basic recombinant human Fibroblast Growth Factor (b-FGF) (Sigma, Cat. F0291). Experiments were carried out after 4 days of differentiation in DMEM:F12 medium containing N2 supplement, 2 ng/mL human recombinant GDNF (R&D Systems, Cat. 212-GD), 1 mM dibutyryl cAMP (Sigma, Cat. D0260) and 1 µg/mL tetracycline (Sigma, Cat. 87128). Cells were plated at a density of 1 x 10^5 cells/mL (100 µL per well) and treated with soluble aggregates in a 1:5 dilution. Lipopolysaccharide (LPS) (Invivogen San Diego, CA, Cat. Tlrl-3pelps) at 10 ng/mL was used as a positive control and aCSF buffer in a 1:5 dilution was used as a vehicle control. The plate was placed in an IncuCyte® S3 live cell imaging system right after treatment and monitored for 48 hr. Four images were taken per well (~600 cells per field of view), every hour, with three wells per condition, totaling ~7,200 cells imaged per condition per experiment. Two biological replicates were carried out. Neurite length was measured using NeuroTrack software with the following settings: Segmentation Mode: Brightness; Segmentation Adjustment: 0.7; Adjust size (pixels): 1; Min Cell Width (µm): 25; Area (µm^2) min: 500; Neurite Filtering: Best; Neurite Sensitivity: 0.25; Neurite Width (µm): 4.

2.11. Liposome-permeabilisation assay

The liposome-permeabilisation assay was carried out by Dr Patrick Flagmeier, Dr Suman De, and Zengjie Xia.

The membrane permeabilisation assay was performed as described previously.[194] Briefly, liposomes composed of 16:0-18:1 PC and 18:1-12:0 biotin PC (100:1) (Avanti Lipids), with an average diameter of 200 nm, were prepared using extrusion and freeze-thaw cycles. Vesicles filled with 100 μM Cal-520 dye were bound to a glass surface coated with PLL-g-PEG and PLL-g-PEG biotin (10:1) (Susos AG), via a biotin-neutravidin linkage. A series of 9 different images were taken of 30 μL Ca^{2+} containing buffer alone to measure the background for each set (F_{blank}). The same volume of soluble aggregates was then incubated on the glass coverslip for 15 min and imaged in the exact same fields of view (F_{sample}). The same fields of view were then re-imaged after the addition of 10 μL of ionomycin ($F_{ionomycin}$). By first determining the intensity of each individual vesicle, the average Ca^{2+} influx was calculated using the following formula:

$$\left(\frac{F_{sample} - F_{blank}}{F_{ionomycin} - F_{blank}}\right) \times 100\%$$

Imaging was carried out using a home-built total internal reflection fluorescence (TIRF) microscope, fitted with a 488 nm laser (Toptica, iBeam smart, 200 mW, Munich, Germany), which was used to excite the samples. The laser beam was expanded and collimated using two Plano-convex lenses on the back-focal plane of the 60X, 1.49NA oil immersion objective lens (APON60XO TIRF, Olympus, product number N2709400) to a spot of adjustable diameter. An EmCCD camera (Photometrics Evolve, EVO-512-M-FW- 16-AC-110) was used to image the dye fluorescence emissions collected by the objective.

2.12. Aptamer-DNA PAINT (AD PAINT) imaging

AD PAINT imaging was carried out by Dr John Danial and Dr Jason C. Sang.

AD PAINT imaging was performed as described previously, with a few adaptations.[202] Briefly, round slides were cleaned for 1 hr with argon plasma. A multiwell chamber coverslip (CultureWell CWCS-50R-1.0) was then added to the slide. The wells were cleaned with PBS 1% v/v Tween 20 for 1 hr before adding 5x diluted soluble aggregate samples in PBS for 1 hr. The wells were washed twice with fresh PBS and replaced

with imaging mix (2 nM imaging strand (sequence CCAGATGTAT-CY3B), and 100 nM aptamer-docking strand (sequence GCCTGTGGTGTTGGGGCGGGTGC-GTTATACATCTA) in PBS). All buffers were passed through a 0.02 µm filter (Anotop25, Whatman, Cat. 516-1501) before use. Prior to imaging, a clean coverslip was used to seal the wells in order to prevent evaporation. Imaging was performed on a home-built TIRF microscope using a 1.49 N.A., 60x objective (UPLSAPO, 60X, TIRF, Olympus) and a perfect focus system. More details about the microscope set up and data analysis are described in Whiten et al.[202]

2.13. Atomic force microscopy (AFM) imaging

AFM imaging was carried out by Dr Francesco Simone Ruggeri.

Brain-derived soluble aggregates were diluted 10x in PBS buffer and imaged on freshly cleaved mica substrates using AFM. 10 µL diluted samples were deposited on the substrate at room temperature. The samples were incubated for 10 min, followed by rinsing with 1 mL milliQ water. The samples were then dried using a gentle flow of nitrogen gas. AFM maps of 3-D morphology of all the samples were acquired in regime of constant phase change, with 2-4 nm/pixel resolution using a NX10 (Park Systems, city, South Korea) operating in non-contact mode.[203] This set up was equipped with a silicon tip with a nominal radius of <10 nm and spring constant of 5 N/m (PPP-NCHR). For each sample, we scanned an area between 250-500 μm^2. The lower limit was used for samples where aggregated species were found and the upper limit for the samples without aggregates. Scanning Probe Image Processor (SPIP) (version 6.7.3, Image Metrology, Denmark) software was used for image flattening and single aggregate statistical analysis. The average level of noise for each image was measured using SPIP software and was smaller than 0.1 nm.[204] All the measurements were performed at room temperature.

2.14. Single-molecule pull-down (SiMPull) imaging

SiMPull imaging was carried out by Derya Emin, Yu P. Zhang, and Dr Evgenia Lobanova

Glass coverslips covalently mounted with polyethylene glycol (PEG) were used for SiMPull experiments. Coverslip preparation was carried out as described previously, with a few modifications.[205] Briefly, glass coverslips (26X76 mm, thickness 0.15 mm, Thermo Scientific) were washed ultrasonically (cleaner USC100T, VWR), in a series of solvents (10 min in 18.2-MΩ/cm Milli-Q water, 10 min in acetone, then 10 min in

methanol (MeOH)). The washed coverslips were then etched by 1 M potassium hydroxide (KOH) under 20 min ultrasonication and rinsed with a series of solvents (MeOH, 18.2 MΩ-cm Milli-Q water, then MeOH). The processed coverslips were dried using nitrogen flow and cleaned with argon plasma for 15 min (Femto Plasma Cleaner; Diener Electronic). The coverslips were then silanised with 5 mL of 3-aminopropyl triethoxysilane (Fisher Scientific UK, Cat. 10677502), 8.3 mL acetic acid (AcOH) in 166.7 mL MeOH for 20 min, with 1 min ultrasonication at the start and mid-point of reaction (10 min after the start point). The silanised coverslips were then rinsed in MeOH, 18.2 MΩ-cm Milli-Q water, followed by MeOH and dried using nitrogen flow. 50-well polydimethylsiloxane (PDMS) gaskets (Sigma, GBL103250-10EA) were then attached to the cleaned and silanised coverslips. To passivate the wells, 9 µl of a 100:1 aqueous mixture of succinimidyl valeric acid PEG (MPEG-SVA-5000) (110 mg/mL, Laysan Bio Inc.) and Biotin-PEG-SVA-5000 (1.1 mg/mL, Laysan Bio Inc.) were added, with additional 1 µL of 1 M sodium bicarbonate ($NaHCO_3$) (pH 8.5). The coverslips were incubated with PEG solution overnight in a humid chamber and then rinsed with 18.2 MΩ-cm Milli-Q water and dried with nitrogen flow. The passivated wells were treated by adding 9 µl of MS(PEG)4 methyl-PEG-NHS-Ester (10 mg/mL, Thermo Scientific, Cat. 22341), with additional 1 µL of 1 M $NaHCO_3$ (pH 8.5). The coverslips were incubated with PEG solution overnight in a humid chamber and then rinsed with 18.2 MΩ-cm Milli-Q water and dried with nitrogen flow. PEGylated glass coverslips were stored in a desiccator at −20 °C until needed.

For the experiment, neutravidin (0.2 mg/mL) was added to the coverslip for 5 min, followed by two wash steps with 0.05% (v/v) PBST and once with 1% (v/v) PBST. Afterwards biotinylated 6E10 (Signet, Cat. 9340-02, 10 nM) was added for 10 min, followed by two wash steps with 0.05% (v/v) PBST and once with 1% (v/v) PBST. The soluble aggregates were added for at least 1 hr at room temperature followed by two wash steps with 0.05% (v/v) PBST and once with 1% (v/v) PBST. The coverslips were blocked using blocking solution containing 0.1% (w/v) bovine serum albumin (BSA) (Thermo Scientific, Cat. AM2616), 10% (v/v) salmon sperm (Thermo Scientific, Cat. 15632011) and 0.1% (v/v) PBST for 1 hr at room temperature. The coverslips were then incubated with labelled 6E10 (cat. 80302, 500 pM) for 45 min, followed by three washing steps with 0.05% (v/v) PBST. To properly seal the imaging chamber and

prevent evaporation, 3 µL of PBS was added to each well and sandwiched with a second coverslip.

To determine the number of fluorescent molecules in each image, a z-stack was generated in ImageJ. The images were cropped to 380 x 380 pixels and the contrast was adjusted. Using the negative control as a baseline, a threshold was applied to all images, and single molecules above this threshold were counted.

2.15. Primary cell culture

2.15.1. Culturing of rat primary astrocytes for neuroinflammation assay

Primary rat astrocytes were collected from 1-7 days old Sprague-Dawley rat pups, which were grown and culled at the Department of Veterinary Medicine, Cambridge. The protocol for harvesting and culturing this mixed glial prep was carried out as previously described with slight modifications.[206,207] Briefly, the brain was removed and placed in a petri dish filled with Hank's balanced salt solution (HBSS). Then the brain was carefully rolled onto lens paper to remove visible blood vessels and pressed through a filter into a falcon tube using a spoon. 2 mL of media with 10% v/v Hyclone™ FBS (GE Life Sciences, Cat. SV30160.03) was added onto the filter. The remaining tissue was then pushed through the filter, followed by the addition of 3 mL of media. The falcon tube was centrifuged at 1,500 $g_{(av)}$ for 5 min. The supernatant was removed and re-suspended in 30 mL of media, followed by careful trituration. Another 15 mL of media was then added, and the solution was plated out in three T75 flasks, 15 mL per flask. These were then incubated at 37 °C, 5% CO_2. The mixed-glial prep was composed almost entirely of astrocytes 2 weeks after plating.

2.15.2. Culturing of human primary astrocytes for neuroinflammation assay

Human primary astrocytes were purchased from ScienCell Research Laboratories (SC-1800) (1 x 10^6 cells/vial) and provided by our collaborators at the Institute of Neurology, University College London. These cells were grown in astrocyte medium (ScienCell Research Laboratories, SC-1801), in T75 flasks, in an incubator at 37 °C, 5% CO_2.

2.15.3. Culturing of mouse primary neurons for neurite retraction assay

The brains from the mouse embryos were removed and placed into a petri dish containing HBSS. The hippocampi and cortices were isolated, the meninges removed,

and the tissue was transferred to a falcon tube with 15 mL HBSS on ice. 500 µL of trypsin was added to the falcon tube and incubated at 37 °C in a water bath for 15 min. Under a sterile fume hood, the HBSS/trypsin solution was replaced with fresh pre-warmed neurobasal media (NBM) and washed twice. The tissue was then resuspended in 1 mL NBM (Thermo Fisher Scientific, cat. 21103049) supplemented with with 2% v/v B27 (Thermo Fisher Scientific, 17504044), 1% v/v N2, 1% v/v Pen/Strep and 1% v/v GlutaMax. The cells were then counted and plated in 96-well plates (Greiner, 655090) coated with Poly-D-Lysine (PDL) (Greiner, A3890401). There was a 30% media change at 4 DIV, then every 2-3 days after. This was done by Robyn McAdam at AstraZeneca.

2.15.4. Culturing of mouse primary microglia for neuroinflammation assay

Brains were removed from the mouse pup heads (using scissors and forceps) and kept in growth medium (DMEM with GlutaMax supplemented with 10% v/v FBS and pen/strep, on ice in a petri dish). The meninges were removed by rolling on sterile filter paper. All brains were placed in fresh growth medium and triturated vigorously using a 10 mL pipette up and down a 50 mL falcon tube, for 5-10 min, then filtered through a cell strainer (40 micron). They were then centrifuged at 250 $g_{(av)}$ for 2 min and the cells were resuspended in a total volume of 40 mL per flask, with 4 brains per flask. Cells were left for 1 week to adhere and for the astrocyte layer to proliferate. The microglia gradually form a layer on top of this confluent layer. To increase the number of microglia in the mixed glial prep, 5 ng/mL murine GM-CSF (from R+D systems) was added to enhance microglia proliferation. The cells were left in the GM-CSF-enriched medium for 1 week. Microglia were removed by “shaking” overnight in an orbital shaker incubator (37 °C, 100 revolutions per minute). HEPES was added to the medium (50 mM final) just prior to shaking cells overnight. Following shaking, the supernatant was collected from the flasks (containing the dissociated microglia). The microglia were centrifuged at 250 $g_{(av)}$ for 2 min and resuspended in medium without GM-CSF, counted, and plated in 96-well plates.

2.16. Immunostaining for neurons, astrocytes, and microglia

Cells were washed with PBS (50 µL per well for a 96-well plate) and fixed for 10 min at room temperature with a solution of 4% PFA v/v in PBS (50 µL per well for a 96-

well plate). The cells were washed again with PBS before adding the following primary antibody solutions:

Table 4: Table of primary antibodies used for immunostaining

Antigen	Description	Cell Type	Working concentration	Host Species	Source
NeuN	Expressed in neuronal nuclei	Neurons	1.6 µg/mL	Rabbit	Abcam ab177487
β-III Tubulin	Expressed almost exclusively in neurons and testis cells	Neurons	1 µg/mL	Mouse	Abcam ab78078
GFAP	Astrocyte-specific expression among glial cells	Glia	21.6 µg/mL	Chicken	Abcam Ab4674
Iba1	Microglial and macrophage-specific expression	Glia	0.5 µg/mL	Rabbit	WAKO 019-19741

The primary antibodies were prepared in PBS supplemented with 0.2% v/v Tween 20.

The primary antibody solution was incubated in the plate overnight at 4 °C, followed by three washes with PBS (100 µL per well for a 96-well plate). The following secondary antibody solutions were then added:

Table 5: Table of secondary antibodies used for immunostaining

Antibody	Working concentration	Host Species	Source
Anti-mouse 488 (FITC)	0.2 µg/mL	Goat	Invitrogen A11001
Anti-rabbit 647 (Cy5)	0.2 µg/mL	Goat	Invitrogen A21244
Anti-rabbit 488 (FITC)	0.2 µg/mL	Goat	Invitrogen A11034
Anti-chicken 647 (Cy5)	0.2 µg/mL	Goat	Invitrogen A21449

The secondary antibodies were prepared in PBS supplemented with 0.2% v/v Tween 20.

The secondary antibody solution was incubated at room temperature for 1 hr, before being removed and replaced with 40 µL of Hoechst stain in blocking solution (1:10000) and incubated for 10 min at room temperature. The cells were washed 3 times with PBS (100 µL per well for a 96-well plate) and imaged with an Olympus epifluorescence microscope.

2.17. Protein measurements

Table 6: Protein measurements using different commercially available kits

Target	Method	Species Reactivity	Product code	Source
TNFα	ELISA	Mouse	DY410	R&D Systems
Aβ42	ELISA	Human	KHB3441	Invitrogen
Aβ42	ELISA (ultrasensitive)	Human	KHB3544	Invitrogen
Total protein	BCA	Mammalian/ non-specific	23225	Thermo Fisher Scientific
TNFα, IL-1β, IL-6, MCP-1, RANTES, MIP-1a, MIP-1b	ELISA - multiplex	Mouse	Customised on website	Meso Scale Delivery
β-galactosidase	Immunostaining	Mammalian/ non-specific	C10850	Invitrogen

Various commercially available kits were used to measure the concentrations of various protein targets.

2.17.1. Western blot

Samples were diluted in Bolt LDS Sample Buffer (Thermo Fisher Scientific, Cat. B0008), Bolt Reducing Agent (Thermo Fisher Scientific, Cat. B0009), and distilled water to appropriate concentration. They samples were then heated at 70 °C for 10 min. A pre-cast 1.0 mm 4 - 12% gradient 15-well Bolt Bis-Tris Plus gel (Thermo Fisher Scientific, Cat. NW04125BOX) was set up in a Mini Gel Tank (Thermo Fisher Scientific) with SDS Running Buffer (50 mL of 20X Bolt MES SDS Running Buffer [Thermo Fisher Scientific, Cat. B0002], 950 mL of distilled water, and 2.5 mL of Bolt Antioxidant [Thermo Fisher Scientific, Cat. BT0005]). A Chameleon Duo pre-stained Protein Ladder (LI-COR, Cat. 928-60000) was loaded into the appropriate wells, and electrophoresis was set to run at 200 V. The proteins separated on the gel were transferred onto a low-fluorescence PVDF membrane using the iBlot 2 Dry Blotting System (Thermo Fisher Scientific) with iBlot 2 Transfer Stacks (Invitrogen, Cat. IB24001). The membrane was blocked using 10 mL of Intercept Blocking Buffer in PBS (LI-COR, Cat. 927-90001) for 1 hr at room temperature, and then washed with PBS supplemented with 0.2% Tween (v/v), and incubated with 6E10 primary antibody (BioLegend, Cat. 803004) at 1 µg/mL, diluted in blocking buffer, overnight at 4 °C on

a shaker. This was then washed and replaced with IRDye 800CW Donkey anti-Mouse IgG secondary antibody (LI-COR, Cat. 926-32212) diluted 1:10000 in blocking buffer and incubated for 1 hr in room temperature on a shaker. The membrane was then washed and imaged on an Odyssey CLx Imaging System (LI-COR Biosciences).

2.18. Statistical analysis

GraphPad Prism v9 was used to carry out statistical analyses for all experimental data except for AFM data. Unpaired two-tailed t-tests have been used to test the null hypothesis, in cases where two independent, normally distributed samples needed comparing. An alpha value of ($p < 0.05$) was chosen to represent significant differences in the data (* = $P \leq 0.05$, ** = $P \leq 0.01$, *** = $P \leq 0.001$). In cases where more than two independent variables needed comparing, a one-way analysis of variance (ANOVA) was used. This was followed by a Tukey post hoc test when comparing the mean of each variable to the mean of every other variable, or a Dunnett post hoc test when comparing the mean of each variable to the mean of one control variable. Kolmogorov-Smirnov tests have been used when comparing non-normally distributed cumulative distributions (AD PAINT and SiMPull data). To assess the variability between independent repeats of the experiment and between patients, multiple comparisons tests were carried out. Individual statistical values are reported in the figure legends.

Scanning Probe Image Processor (SPIP) software was used for image flattening and single aggregate statistical analysis for AFM imaging data. AFM data was plotted using OriginPro® 2021. Mann-Whitney two-tailed tests were used to compare the medians of the non-normally distributed data sets. Individual statistical values are reported in the figure legends.

Patient samples were blinded prior to experimentation and were only unblinded after data analysis. Region selection for all imaging experiments was automated, ensuring randomisation and elimination of human bias. Furthermore, data analysis parameters (e.g. thresholding) were kept consistent within each data set. Data gathered by ELISA or MSD was analysed using MARS data analysis software. A four-parameter fit was fitted to the data, as per the kit manufacturer's instructions. Schematics/graphics were created using ChemDraw v19.0 and Microsoft PowerPoint.

3: Preclinical Testing of Passive Immunotherapies

3.1. Introduction

It is widely reported that Aβ aggregates can cause neuroinflammation, a key player in AD pathology. The sustained activation of glial cells leads to the overproduction of proinflammatory cytokines and chemokines, which contribute to neurodegeneration. TNFα is the cytokine most strongly associated with AD pathology, due to its involvement in the aggregation of Aβ42.

There are multiple ways of assessing neuroinflammation *in vitro*. These include performing immunocytochemistry to image specific glial markers, using quantitative real-time PCR to measure gene expression of inflammatory markers, performing live-cell phagocytosis or cell viability assays, and by measuring the release of cytokines and chemokines from stimulated glial cells using ELISA or Western blotting.[167,208–210] These assays are generally performed on microglial or astrocytic cell lines, primary cells, or iPSC-derived cells. Primary and iPSC-derived cells are generally more clinically relevant as they better recapitulate endogenous glial cell properties, however cell lines are more commonly used as they are easier to obtain and culture, while still maintaining important glial properties.[211]

In this chapter, a neuroinflammation assay has been optimised that allows the measurement of TNFα production from an Aβ42-treated microglial cell line using an ELISA. This assay can be employed as a preclinical platform for drug testing against Aβ-mediated inflammation. A proprietary anti-Aβ42 antibody from MedImmune (now AstraZeneca) has undergone preclinical testing using a variety of assays to measure its effects on Aβ42-driven inflammation and liposome permeability.

3.2. Neuroinflammation assay

For the optimisation of the neuroinflammation assay, a widely reported microglial-like cell line was used due to its convenience and ease of handling. BV2 is a well-characterised, immortalised murine microglial cell line that is often used when primary microglia are not available. Similar to primary microglia, they are widely reported to produce an inflammatory response to LPS, show physiological regulation of nitric oxide (NO) production, respond to IFN-γ from T-cells and can stimulate other glial cells.[212] The experimental set up of the neuroinflammation assay was as follows:

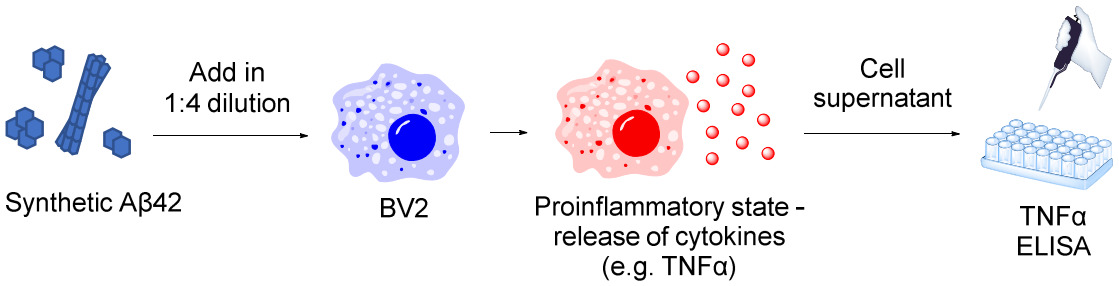

Figure 10: Schematic of neuroinflammation assay

Aggregated synthetic Aβ42 was added in a 1:4 dilution to BV2 cells, triggering proinflammatory cytokine release. Levels of TNFα in the cell supernatant were then measured by ELISA, acting as a marker of inflammation. A vehicle control was always included as a negative control, and LPS was added as a positive control for inflammation.

3.2.1. LPS optimisation

LPS, which is found in the outer membrane of gram-negative bacteria, is often used as a positive control for inflammation experiments as it causes TLR4 activation. To determine the appropriate concentration of LPS to use for the neuroinflammation assay, an LPS dose-response was carried out. The cell supernatant was also tested using a lactose dehydrogenase (LDH) assay to test cell viability.

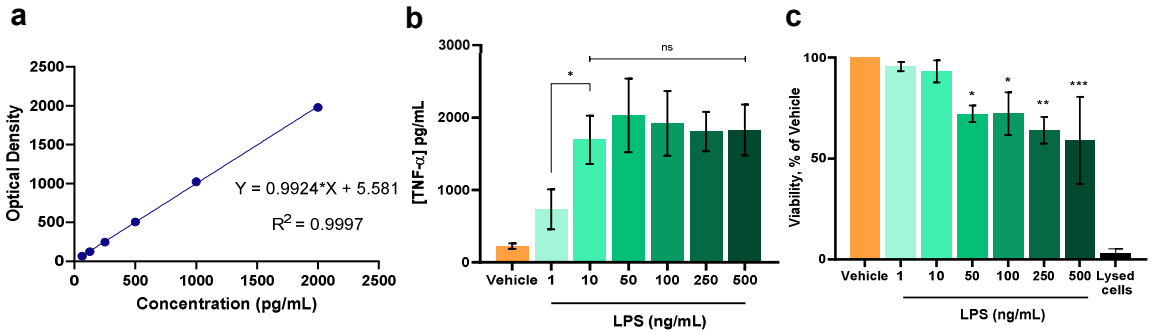

Figure 11: LPS dose-response

(**a**) Standard curve showing the linear range of the TNFα assay (~62.5 - 2,000 pg/mL). A 4-parameter fit has been used to calculate the levels of TNFα in the samples. (**b**) BV2 cells were treated with various concentrations of LPS for 24 hr. BV2 cells were plated at 50,000 cells/well in 48 well plates. Vehicle control was DMEM + endotoxin-free water used to dilute the LPS. TNFα production was measured by ELISA. Error bars represent the mean ± SD of three wells. (One-way ANOVA: $F(6\ 14) = 12.05$, $p < 0.001$. Post hoc Tukey test: 1 vs 10: $p = 0.049$; 10 vs 50: $p = 0.89$; 10 vs 100: $p = 0.98$; 10 vs 250: $p > 0.99$; 10 vs 500: $p > 0.99$; 50 vs 100: $p > 0.99$; 50 vs 250: $p = 0.98$; 50 vs 500: $p = 0.99$; 100 vs 250: $p > 0.99$; 100 vs 500: $p > 0.99$; 250 vs 500: $p > 0.99$). (**c**) LDH cytotoxicity assay used on cell supernatant to measure cell viability. Error bars represent the mean ± SD of three wells. (One-way

ANOVA: $F(6, 14) = 8.502$, $p < 0.001$. Post hoc Dunnett test: Vehicle vs 1: $p = 0.98$; Vehicle vs 10: $p = 0.89$; Vehicle vs 50: $p = 0.02$; Vehicle vs 100: $p = 0.02$; Vehicle vs 250: $p = 0.002$; Vehicle vs 500: $p < 0.001$).

LPS at 10 ng/mL caused a significant increase in TNFα response. However, increasing the concentration past 10 ng/mL had no significant effect, similar to what has been previously reported with another microglial cell line.[213] Furthermore, concentrations higher than 10 ng/mL caused significant cell death. LPS-induced BV2 cell death has been previously reported using MTT assays measuring mitochondrial dysfunction, fluorescence microscopy using calcein (for live cells) and ethidium homodimer (nuclear stain for dead cells), and Greiss assays for measuring iNOS and NO production.[214] 10 ng/mL was therefore selected as the optimal LPS concentration for future experiments.

3.2.2. FBS optimisation

Initial experiments had relatively high basal levels of TNFα after 24 hours, ~200 pg/mL (**Figure 11a**). This suggested that the cells were stressed, most likely due to the presence of endotoxin contamination, which could compromise the integrity of the data. The FBS in cell media is a potential source of endotoxin, with endotoxin levels varying greatly from batch-to-batch and between suppliers, and can trigger an inflammatory response in macrophages.[215] Two types of FBS, HyClone™ (SV30160.03) and Sigma (F0926) were therefore tested to determine whether FBS endotoxin was contributing to the high basal levels of TNFα.

Furthermore, it is common to reduce or completely remove serum before experiments involving cytokine measurements.[75] The reason for this is that FBS contains a wide range of proteins that could potentially elicit an inflammatory response. In addition, FBS increases cell proliferation, which can cause over confluency in longer experiments. To determine the optimal concentration of FBS for these experiments, three conditions were tested: serum-free, 1% FBS, and 10% FBS.

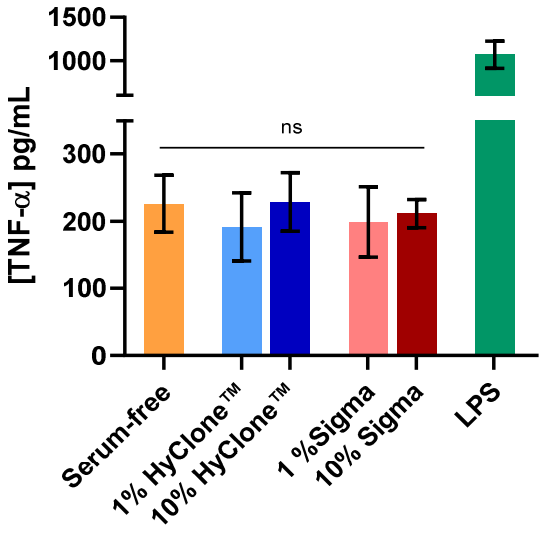

Figure 12: FBS optimisation

BV2 cells were plated in three serum conditions: serum-free, 1% FBS and 10% FBS. Two types of FBS were tested, HyClone™ FBS and Sigma FBS. TNFα production was measured by ELISA after 24 hr. Prior to experimentation, the cells were grown in 10% HyClone™ FBS supplemented DMEM for two weeks. BV2 cells were plated at 50,000 cells/well in 48 well plates. Error bars represent the mean ± SD of three wells. (One-way ANOVA: $F(4, 10) = 0.4246$, $p = 0.79$. Post hoc Tukey test: Serum-free vs 1% HyClone: $p = 0.86$; Serum-free vs 10% HyClone: $p > 0.99$; Serum-free vs 1% Sigma: $p = 0.93$; Serum-free vs 10% Sigma: $p > 0.99$; 1% HyClone vs 10% HyClone: $p = 0.83$; 1% Sigma vs 10% Sigma: $p > 0.99$).

Both HyClone™ and Sigma FBS induced similar levels of TNFα production. Furthermore, there was no significant difference between the inflammation produced from cells plated in 10% FBS, 1% FBS, or serum-free conditions. This suggested that FBS-endotoxin may not be the source of the elevated basal levels of TNFα.

Other potential sources of endotoxin contamination included non-sterile cell culture reagents and sub-optimal cell culture practices. Non-filtered pipette tips and benchtop tubes were replaced with autoclaved pre-sterilised filtered pipette tips and LoBind Eppendorf tubes. Cell media was made fresh every two weeks instead of monthly and supplemented with HEPES buffer to reduce changes in pH. To confirm whether these conditions had an effect on basal TNFα levels, the FBS experiments were repeated with and without the improved sterile conditions.

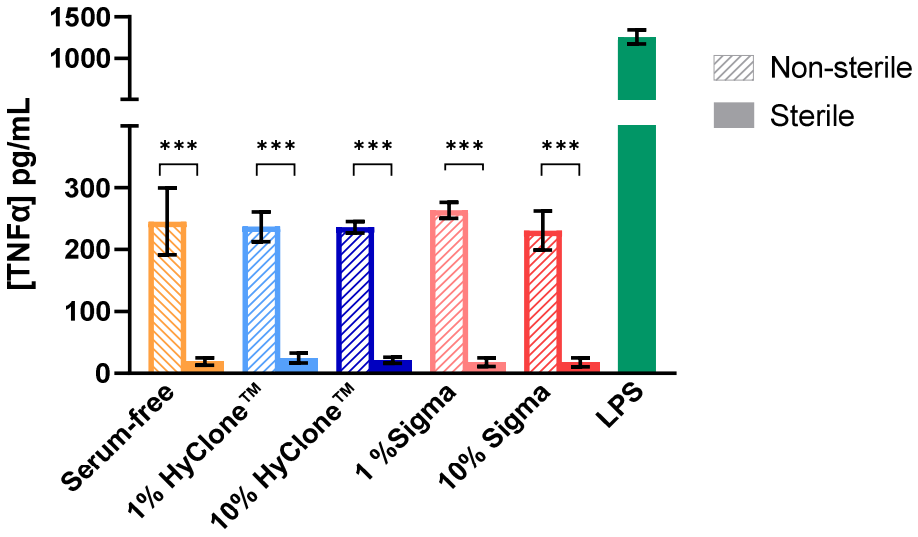

Figure 13: Further FBS optimisation with and without improved sterile conditions

BV2 cells were plated in three serum conditions: serum-free, 1% FBS and 10 % FBS. Two types of FBS were tested, HyClone™ FBS and Sigma FBS. TNFα production was measured by ELISA after 24 hr. Prior to experimentation, the cells were grown in 10% HyClone™ FBS supplemented DMEM for two weeks. BV2 cells were plated at 50,000 cells/well in 48 well plates. Solid filled bars represent the conditions with the improved sterile changes ('sterile'), and the striped bars represent the conditions without ('non-sterile'). Error bars represent the mean ± SD of three wells. (One-way ANOVA: $F(0, 20) = 82.91$. Post hoc Tukey test: Serum-free (non-sterile) vs Serum-free (sterile): $p < 0.001$; 1% HyClone (non-sterile) vs 1% HyClone (sterile): $p < 0.001$; 10% HyClone (non-sterile) vs 10% HyClone (sterile): $p < 0.001$; 1% Sigma (non-sterile) vs 1% Sigma (sterile): $p < 0.001$; 10% Sigma (non-sterile) vs 10% Sigma (sterile): $p < 0.001$).

As seen previously (**Figure 12**), there was no significant difference between the three different FBS concentrations, or the two different types of FBS. However, the implementation of the improved sterile conditions significantly reduced the basal TNFα response. This suggested that the high basal levels of TNFα were due to non-sterile conditions and reagents (non-filtered pipette tips and non-autoclaved Eppendorf tubes), not the FBS type or concentration.

3.2.3. Post-experimental handling of samples

Centrifugation and/or sterile filtering of cell supernatant to remove cell debris is often carried out prior to sample analysis.[216] To determine whether these steps were necessary before ELISA analysis, the frozen supernatant from an experiment where BV2 cells were treated with 1 ng/mL LPS and 10 ng/mL LPS for 24 hours, was collected and passed through these conditions. An ELISA was then carried out to detect whether these conditions had an effect on TNFα measurements.

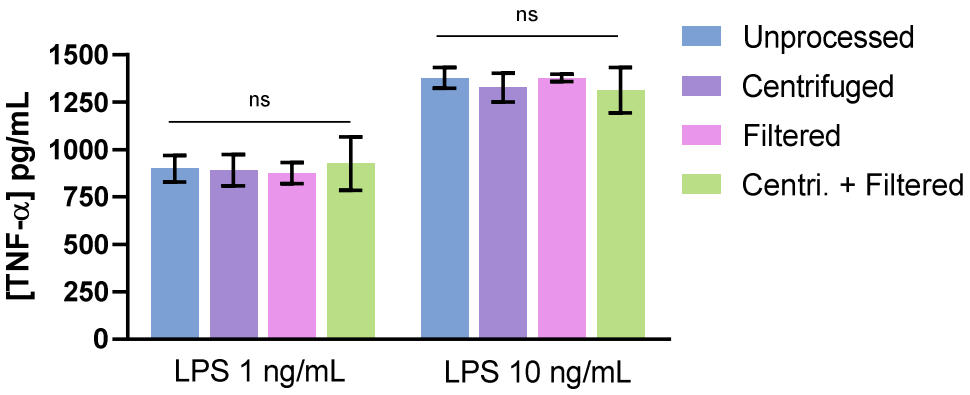

Figure 14: Centrifugation and sterile filtering

Cell supernatants from a previous experiment were either centrifuged at 14,000 $g_{(av)}$ at 4 °C for 10 min, or filtered with a 0.22 µm sterile filter, or both. Supernatant was thawed only once before ELISA analysis. Error bars represent the mean ± SD of three technical repeats. (One-way ANOVA for LPS 1 ng/mL: $F(3, 8) = 0.1482$, $p = 0.93$. One-way ANOVA for LPS 10 ng/mL: $F(3, 8) = 0.5774$, $p = 0.65$).

Centrifuging and/or sterile filtering cell supernatant before ELISA analysis did not appear to affect TNFα measurements. This suggested that cell debris and other cell contents did not impede the ELISA TNFα antibody from binding to its target protein, or generally interfere with the assay. For this reason, centrifugation and sterile filtering of cell supernatants before ELISA experiments was not deemed necessary and was not carried out for future experiments.

Before moving to more clinically relevant samples, synthetic Aβ42 aggregates were used for assay optimisation, due to their availability at high concentrations.

3.2.4. Finding the optimal source and preparation of Aβ42

Synthetic Aβ is notoriously difficult to work with, with difficulties in controlling the aggregations leading to reproducibility issues.[217] Sources of synthetic Aβ can vary

greatly in their aggregation kinetics depending on the supplier, as well as between batches. In addition, there are numerous preparation protocols, which can greatly influence aggregation kinetics. It was therefore important to find a source of Aβ with reliable aggregation kinetics, that could reproducibly produce an inflammatory response. Three Aβ sources were characterised, following their manufacturer's preparation instructions:

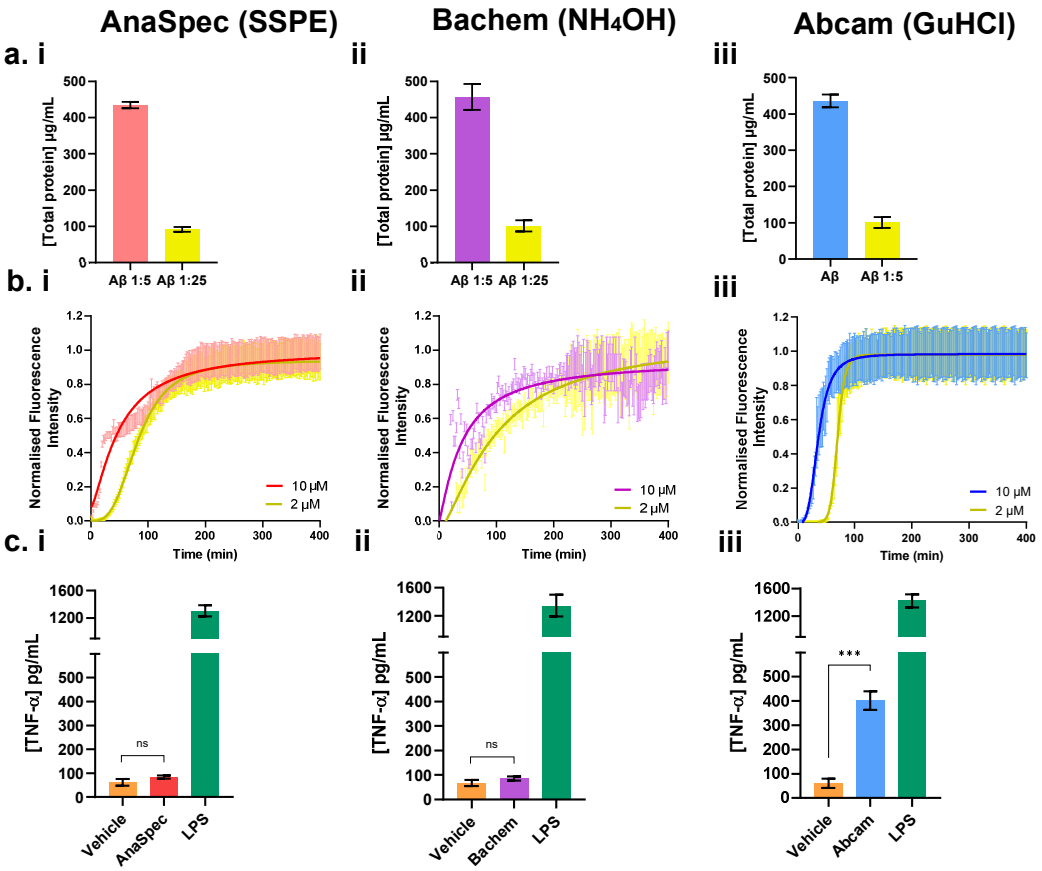

Figure 15: Determining optimal batch of Aβ42

Three different Aβ sources were tested: (i) AnaSpec dissolved in SSPE buffer, (ii) Bachem dissolved in NH_4OH and (iii) Abcam dissolved in GuHCl. (**a**) Aβ concentrations measured with BCA assay to calculate stock concentration and to confirm the concentrations required for kinetics studies. Error bars represent the mean ± SD of three technical repeats. (**b**) Aβ measured with BCA was diluted 10-fold and kinetics were measured with ThT. Measurements were taken every 2 min. A 4-parameter fit has been applied to the data. Error bars represent the mean ± SD of three technical repeats. (**c**) BV2 cells were treated with early Aβ aggregates (2.5 µM) for 24 hr and TNFα levels were measured with an ELISA. The vehicle controls were SSPE, NH_4OH, and GuHCl, respectively. Error bars represent the mean ± SD of three wells. (Unpaired two-tailed t-test: n = 3 for all. Vehicle vs AnaSpec: $t_4 = 2.537$, $p = 0.06$; Vehicle vs Bachem: $t_4 = 2.059$, $p = 0.11$; Vehicle vs Abcam: $t_4 = 13.79$, $p < 0.001$).

Of the three Aβ sources tested, the batch from Abcam was the only one that produced a significant inflammatory response in BV2 cells (**Figure 15c**). The vehicle control did not produce a strong response, suggesting that the GuHCl itself was not responsible for this response. Moreover, aggregation kinetics were measured using ThT, a benzothiazole salt amyloidophilic dye that fluoresces when bound to beta-sheet structures.[197] The kinetics of the Abcam batch were more consistent with the characteristic sigmoidal shape of Aβ aggregation, than the other two, and were reproducible when repeated. The 10 μM kinetics in the AnaSpec and Bachem batches did not have a visible lag phase, suggesting that they contained seeds, speeding up aggregation (**Figure 15b**). The Abcam Aβ was therefore used for future Aβ experiments due to its strong inflammatory response and consistent aggregation kinetics.

It should be noted that a batch of the Bachem and Abcam Aβ42 were also prepared using HFIP treatment, as per the manufacturer's instructions. However due to significant protein loss from the nitrogen stream drying step, the HFIP method was not used again.

A large batch of Abcam Aβ was purchased, prepared in GuHCl, and passed through a column to ensure that there were no seeds in solution that could affect aggregation. Fast protein liquid chromatography (FPLC) was carried out by Dr. Patrick Flagmeier, as described previously.[194] It was then re-characterised using SDS-PAGE, BCA, and ThT-based kinetics (**Figure 16**).

3.2.5. Abcam Aβ42 characterisation

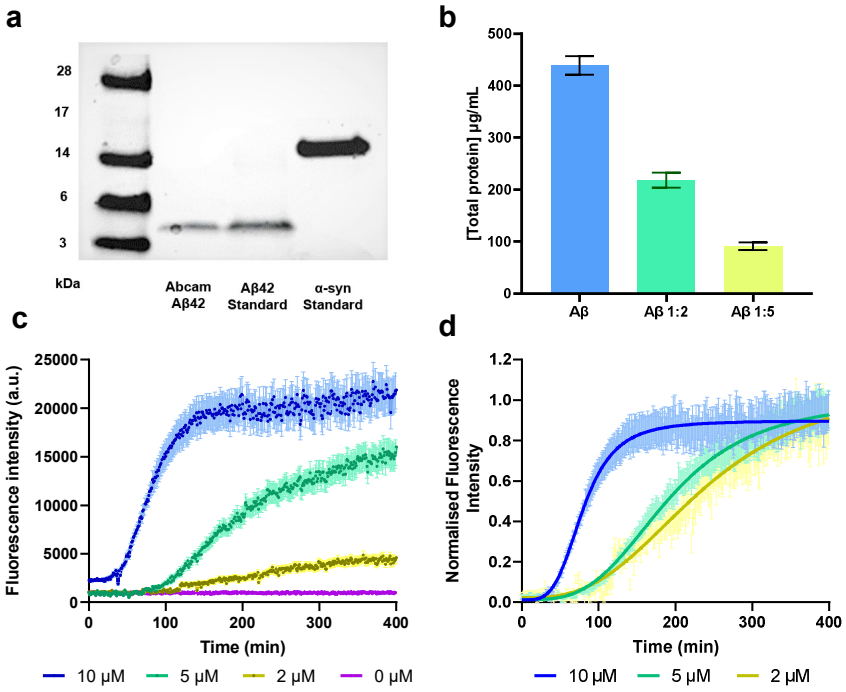

Figure 16: Abcam Aβ42 characterisation after FPLC

Characterisation of Abcam synthetic Aβ42 using (**a**) SDS PAGE to determine the molecular weight and (**b**) BCA assay measurements (total protein concentration) of various dilutions of the Abcam Aβ sample, that were then diluted 10-fold for kinetics studies. Error bars represent the mean ± SD of three technical repeats. (**c**) Raw data of Aβ aggregation kinetics measured with ThT. Error bars represent mean ± SD of three technical repeats. (**d**) Normalised fluorescence intensity (with background subtraction), 4-parameter fit has been applied to each data set. Error bars represent mean ± SD of three technical repeats.

The molecular weight of the Abcam Aβ was confirmed to be around 4.5 kDa with SDS-PAGE (**Figure 16a**). A BCA assay was used to measure the stock concentration of the protein (~100 µM), as well as two dilutions (50 µM and 20 µM) (**Figure 16b**). These concentrations were diluted 10-fold and their aggregation kinetics were measured using ThT.

In order to reliably get monomers, early aggregates, or fibrils, three time points were selected and imaged (**Figure 17**). These time points were then used for future experiments. Aliquots of stock Aβ were flash-frozen and kept in -80 °C for future experimentation.

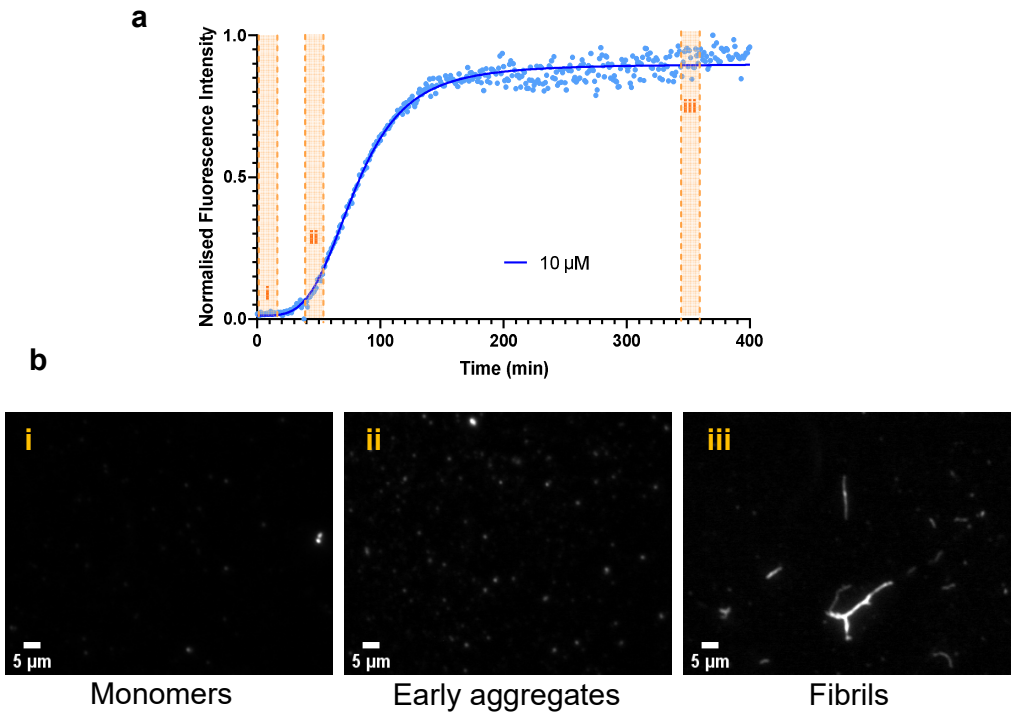

Figure 17: Aβ42 aggregation time points

(**a**) Normalised ThT fluorescence intensity (with background subtraction and 4-parameter fit) of 10 µM synthetic Aβ42, showing the three time points that were chosen to represent Aβ42 (i) monomers, (ii) early aggregates, and (iii) fibrils. Points represent the mean from three wells; error bars not shown. (**b**) Representative ThT images of Aβ (i) monomers, (ii) early aggregates and (iii) fibrils using TIRF microscopy. Concentrations for imaging were 100 nM Aβ and 25 µM ThT.

3.2.6. Aβ42 time and concentration optimisation for neuroinflammation assay

Now that a source of Aβ had been characterised and shown to elicit a strong inflammatory response in BV2 cells, the time durations of future experiments needed to be optimised. BV2 cells were treated with a high concentration of Aβ42 (2.5 µM) to ensure a strong response, for up to 48 hours, with supernatant collected at 3, 6, 24, 36, and 48-hour time points. TNFα levels in the supernatant were measured with a TNFα ELISA.

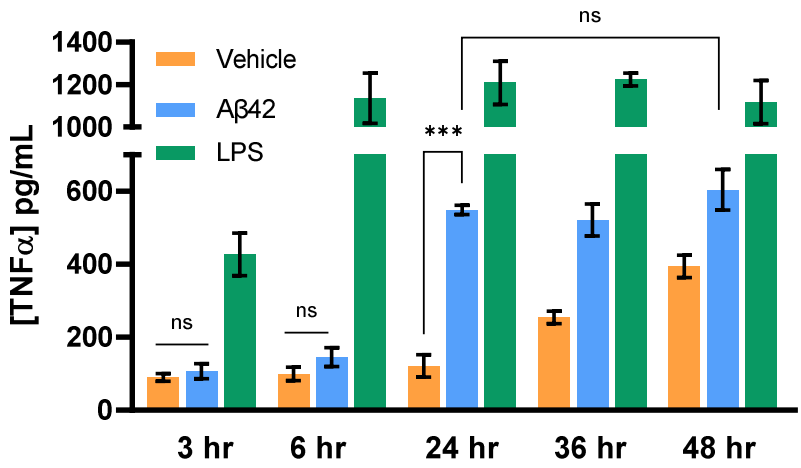

Figure 18: Aβ42 optimisation

BV2 cells, plated at 50,000 cells/well, were treated with 2.5 μM synthetic Aβ42 for 3, 6, 24, 36, and 48 hr, without media changes. Error bars represent the mean ± SD of three wells. (One-way ANOVA: $F(9, 20) = 95.01$, $p < 0.001$. Post hoc Tukey test: $n = 3$ for all: Vehicle (3 hr) vs Aβ42 (3 hr): $p > 0.99$; Vehicle (6 hr) vs Aβ42 (6 hr): $p = 0.87$; Vehicle (24 hr) vs Aβ42 (24 hr): $p < 0.001$; Vehicle (36 hr) vs Aβ42 (36 hr): $p < 0.001$; Vehicle (48 hr) vs Aβ42 (48 hr): $p < 0.001$. Aβ42 (24 hr) vs Aβ42 (36 hr): $p > 0.99$; Aβ42 (24 hr) vs Aβ42 (48 hr): $p = 0.71$; Aβ42 (36 hr) vs Aβ42 (48 hr): $p = 0.22$).

There was no significant TNFα production in the first 6 hours. 24 hours was the first time point at which there was significant TNFα production, with no significant change at the 36 or 48-hour time points. This suggested that 24 hours was the optimal time of treatment with Aβ42 at 2.5 μM, to get a strong inflammatory response. It should be noted however, that 2.5 μM is much higher than the physiological levels of Aβ42. Lower concentrations of Aβ may require longer treatment before getting a significant inflammatory response. However, the inflammatory response of the vehicle control increased with time (**Figure 18**), especially after the 24-hour time point, most likely due to the cells not having any media changes. To reduce this non-Aβ mediated response, cell supernatants were collected and replaced with fresh media (including Aβ42) every 24 hours, in long-term experiments (lasting over 24 hours).

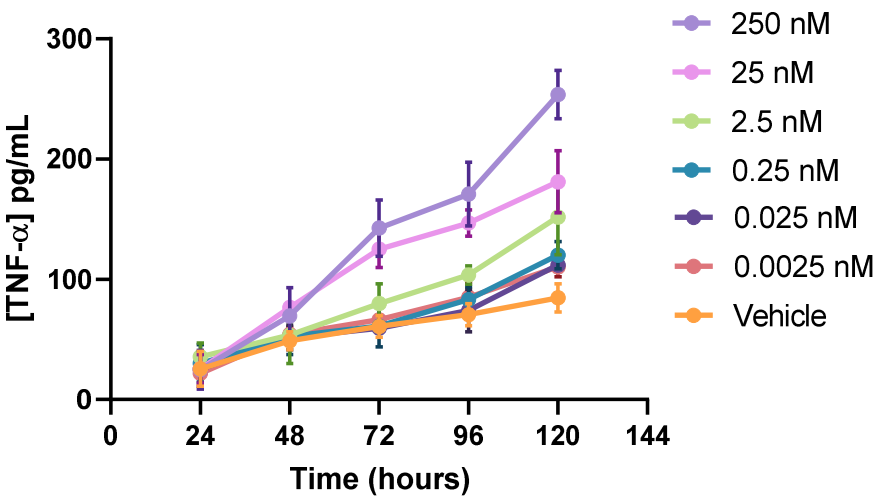

Figure 19: BV2 response to low concentrations of Aβ aggregates

Timecourse of BV2 cells treated with various concentrations of synthetic Aβ42 (Abcam), that was aggregated at 10 μM for 40 min at 37 °C in a microplate under quiescent conditions. Media was collected and changed every 24 hr. LPS concentration used was 10 ng/mL (not shown). Error bars represent the mean ± SD from three wells.

High (micromolar) concentrations of Aβ42 can cause a strong TNFα response in BV2 cells within 24 hours (**Figure 18**). However, when using lower and more physiological concentrations of Aβ42, the TNFα response took longer than 24 hours to be detected (**Figure 19**). The response was concentration-dependent, and interestingly also appeared to increase with time, suggesting a microglial sensitisation over time. The baseline signal also increased with time, most likely due to cell proliferation throughout the course of the experiment. However, aggregate-treated cells had a steeper increase in TNFα production, as has been previously reported in similar experiments with Aβ-treated BV2 cells.[218]

Now that the neuroinflammation assay was optimised for use with synthetic Aβ42, it was ready to be used for the validation of passive immunotherapies.

3.3. Preclinical testing of MedImmune Aβ42 antibody (MedI ATB)

MedImmune (now AstraZeneca) had a proprietary antibody that bound preferentially to Aβ42 than Aβ40, by binding to the C-terminus. This antibody had a mutation in the Fc domain so that it wouldn't bind to Fc-receptors on phagocytes, reducing the possibility of the inflammatory response being mediated by stray microglia recognising the Fc domain. This antibody required further preclinical testing, which provided an opportunity to implement the newly optimised neuroinflammation assay.

The concentration of the MedI ATB was measured using a BCA assay.

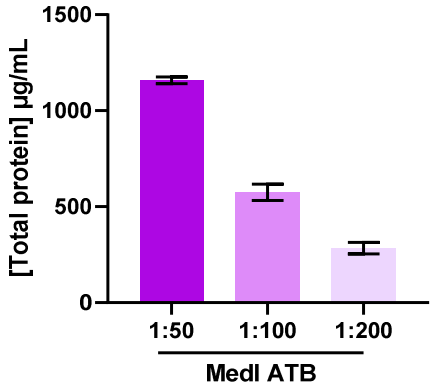

Figure 20: Measuring MedI ATB concentration

Serial dilution of MedImmune antibody concentrations measured using BCA assay. Neat antibody and 1:25 dilution not shown as they exceeded the sensitivity range of the assay (2,000 µg/mL) and could not be detected. Error bars represent the mean ± SD of three technical repeats.

Stock concentration of MedI ATB was calculated to be ~58.43 mg/mL (389.5 µM).

3.3.1. Immunoprecipitation

To test the MedImmune antibody's selectivity for Aβ42, an immunoprecipitation assay was carried out, following a previously reported protocol with a few adaptations.[201]

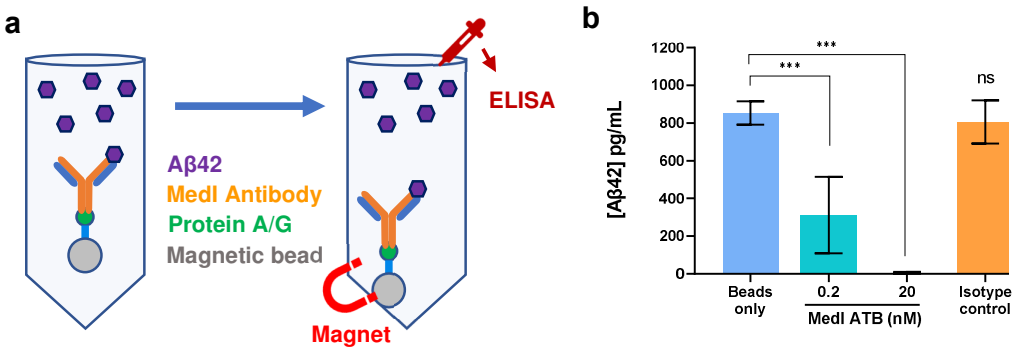

Figure 21: Aβ42 immunoprecipitation with MedI ATB42

(**a**) Schematic of immunoprecipitation assay. Magnetic beads covered in Proteins A & G were added to 2 nM Aβ42. Proteins A & G are surface proteins found in the cell wall of bacteria, which bind to a wide range of immunoglobulins. They differ in their binding strength to antibodies from different species and subclasses. In this way, beads mimic fragment crystallisable (Fc) receptors found on effector cells, which normally bind to the Fc region of antibodies that are attached to infected cells or invading pathogens. In the case of this assay, binding to the Fc region of the antibody left the antigen-binding fragments (Fab) free to bind to their protein targets. The beads, and by extension the antibody and bound protein, could then be pulled down using a magnet. The free-roaming protein in the solution was then measured using an ELISA. (**b**) Two concentrations of the MedI ATB were added to 2 nM Aβ42. Free Aβ in solution was measured using a human Aβ42 ELISA. Beads only control was magnetic beads without antibody. Isotype control was NIP228 at 20 nM. Error bars represent the mean ± SD of three independent experiments. (One-way ANOVA: $F(3, 44) = 137.9$, $p < 0.001$. Post hoc Dunnett test: Beads only vs 0.2 MedI ATB: $p < 0.001$; Beads only vs 20 MedI ATB: $p < 0.001$; Beads only vs Isotype control: $p = 0.66$).

The MedI ATB was able to bind and significantly pull-down the Aβ42 in solution at 0.2 nM and 20 nM (**Figure 21b**). To rule out non-specific binding, an isotype control antibody (NIP228) was used and did not significantly reduce the concentration of Aβ42 in solution. This was further supported with a beads-only control (without antibody) that did not significantly reduce the free Aβ42 in solution. The Aβ42 samples used were not aggregated and were therefore mostly monomeric.

3.3.2. Testing MedI ATB with neuroinflammation assay

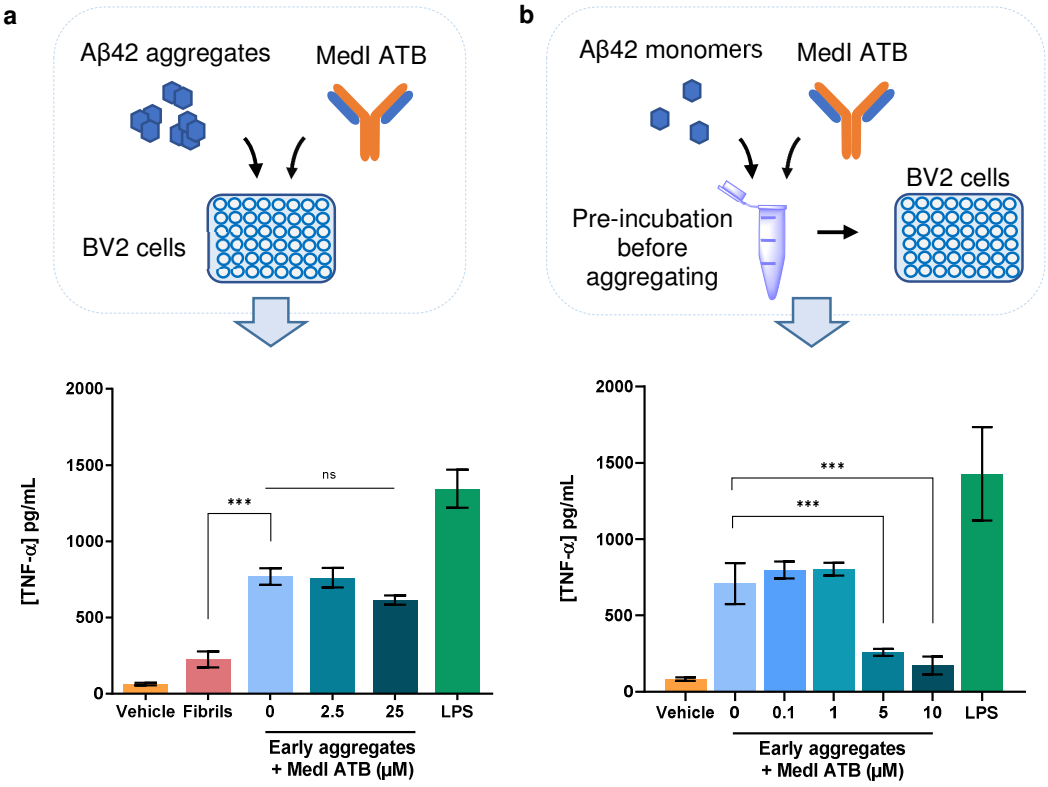

Figure 22: Neuroinflammation assay with MedImmune antibody

(**a**) BV2 cells treated with MedI ATB and 2.5 μM Aβ42 simultaneously. TNFα concentration in cell supernatant was measured 24 hr after treatment with TNFα ELISA. Error bars represent the mean ± SD of three wells. (One-way ANOVA: $F(6, 14) = 189.8$, $p < 0.001$. Post hoc Tukey test: Fibrils vs 0 μM: $p < 0.001$; 0 μM vs 2.5 μM: $p > 0.99$; 0 μM vs 25 μM: $p = 0.19$; 2.5 μM vs 25 μM: $p = 0.28$). (**b**) BV2 cells treated with pre-incubated MedI ATB and Aβ42; final concentration of Aβ42 was 2.5 μM. MedI ATB was added in various concentrations (as seen in graph) to 10 μM Aβ42 monomer solution for 15 min at room temp under quiescent conditions before following standard aggregation protocol for producing aggregates (10 μM Aβ42, ~45 min at 37 °C in 96 well microplate under quiescent conditions). Final concentrations of MedI ATB were a 4-fold dilution of the values presented on the graph. TNFα concentration in cell supernatant was measured 24 hr after treatment with TNFα ELISA. Error bars represent the mean ± SD of three wells. (One-way ANOVA: $F(5, 12) = 74.64$, $p < 0.001$. Post hoc Tukey test: 0 μM vs 5 μM: $p < 0.001$; 0 μM vs 10 μM: $p < 0.001$).

Early aggregates caused significantly higher TNFα production than fibrils (**Figure 22a**), suggesting that early aggregates are the more toxic species. Furthermore, adding the MedI ATB (at various concentrations) and the Aβ42 aggregates simultaneously did not have a significant effect on TNFα levels compared to Aβ42 aggregates alone. This suggested that the MedI ATB was unable to effectively

bind to the Aβ42 aggregates, which would have quickly started adopting a fibrillar form at 37°C. However, pre-incubation of MedI ATB (5 μM and 10 μM) with monomeric Aβ42 prior to aggregation, significantly reduced the levels of TNFα (**Figure 22b**). This suggested that the MedI ATB was able to bind to monomeric and early aggregate species, potentially affecting aggregation kinetics, but was not able to effectively bind to Aβ42 fibrils. To confirm whether the MedI ATB had an effect on aggregation kinetics, ThT kinetics were measured using various concentrations of MedI ATB (**Figure 23**).

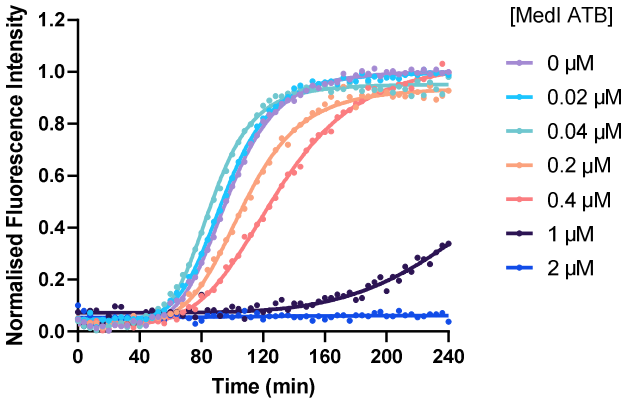

Figure 23: Aβ42 aggregation kinetics + MedI ATB

Normalised ThT kinetics of 2 μM recombinant Aβ42, with various concentrations of MedI ATB. Each dot represents the mean of three technical repeats. Error bars not shown.

An increase in MedI ATB concentration caused a delay in Aβ42 aggregation by increasing the length of the lag phase. This confirmed that the MedI ATB had an effect on aggregation kinetics and could explain the significantly reduced inflammatory response in cells treated with pre-incubated MedI ATB and Aβ42 monomer compared to those treated with Aβ42 aggregates alone (**Figure 22b**).

Recombinant Aβ42 was used for this particular experiment instead of synthetic as it was carried out in conjunction with the liposome assay; an assay that had been previously optimised with recombinant Aβ42 by Dr Patrick Flagmeier and Dr Suman De.[194]

3.3.3. Liposome assay

The liposome assay was carried out by Dr Patrick Flagmeier and Dr Suman De.

The liposome assay measures a protein's ability to permeate a lipid membrane. Seeing as the permeabilisation of cell membranes through non-specific binding is one of the toxic mechanisms of Aβ aggregates, we investigated whether the MedI ATB would be capable of preventing this permeabilisation.

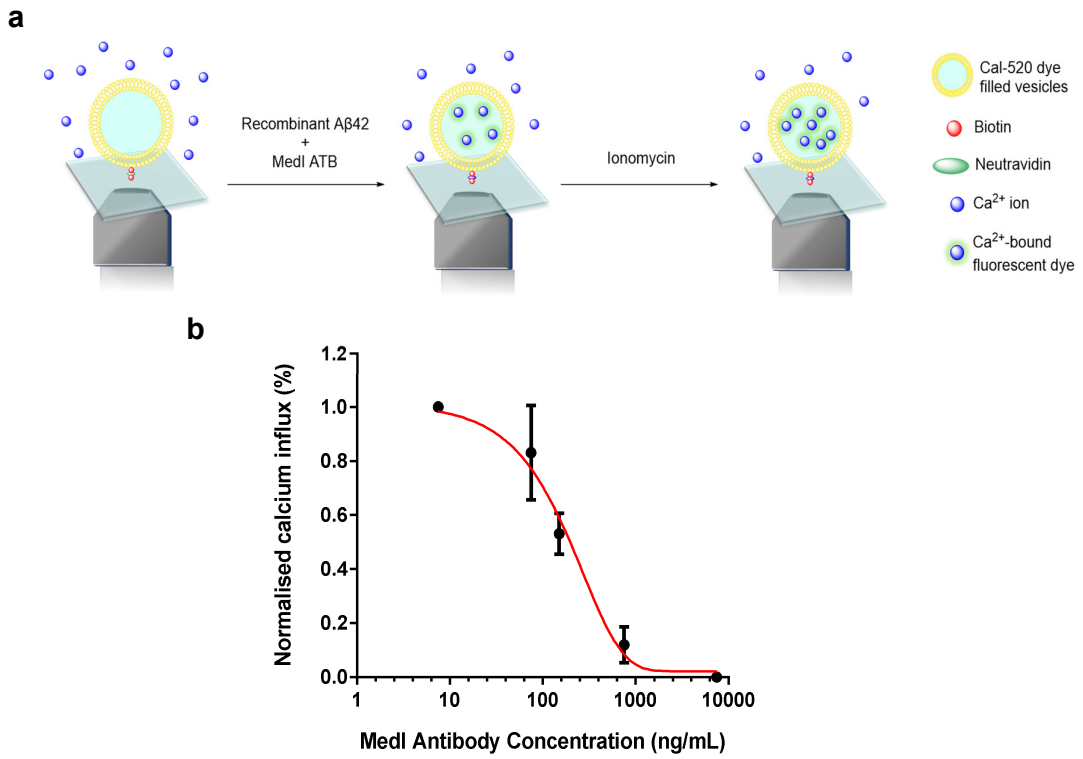

Figure 24: Liposome permeabilisation assay

(**a**) Schematic of liposome permeabilisation assay carried out by Patrick and Suman. (**b**) Results from liposome permeabilisation assay, using 5 nM recombinant Aβ42 early aggregates (based on kinetics from **Figure 23**). MedI ATB concentrations for liposome assay: 0, 7.5, 75, 150, 750, 7500 ng/mL (0, 0.05, 0.5, 1, 5, 50 nM). 9 fields of view were analysed for each condition. A 4-parameter fit has been applied to the data (red line). Error bars represent the mean ± SD from two independent experiments.

The antibody reduced calcium influx in a concentration-dependent manner, due to the binding and prevention of Aβ42 aggregates from penetrating the liposomes. The half maximal inhibitory concentration (IC_{50}) of the MedI ATB was 165.1 ng/mL.

3.4. Improvements to the neuroinflammation assay

3.4.1. Primary cells

In an effort to increase the neuroinflammation assay's relevance to the actual disease condition, the BV2 immortalised cell line was substituted with primary rat astrocytes (cultured from 1-7 day old rat pups from the Department of Veterinary Medicine) and commercially available human primary astrocytes (ScienCell Research Laboratories, SC-1800) supplied by the Institute of Neurology at University College London. However, initial experiments at the Department of Chemistry had high basal levels of TNFα, suggesting endotoxin contamination, so experiments with primary cells were continued at AstraZeneca, which was better equipped for sensitive tissue culture experiments. At AstraZeneca, primary mouse microglial cells were cultured from mouse pups.

As these cells were from a mixed glial prep, immunocytochemistry was used to ensure that most cells were microglial.

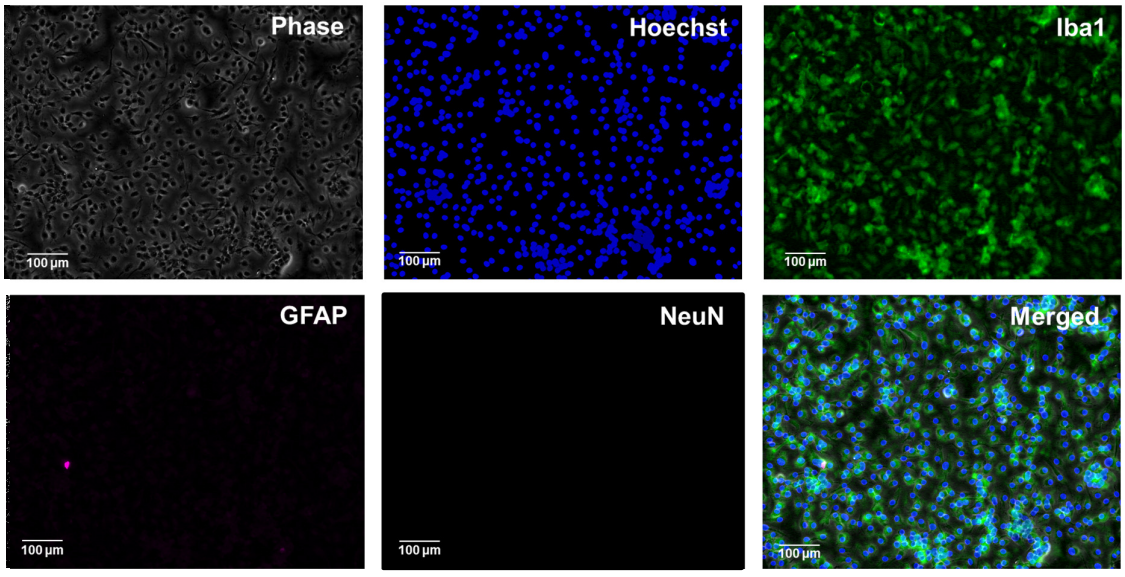

Figure 25: Primary mouse microglia immunostaining

Primary mouse microglia (50,000 cells/well) were immunostained with Hoechst (nuclear stain), Iba1 (microglial stain), GFAP (astrocytic stain) and NeuN (neuronal stain).

Immunostaining confirmed that the cells were mostly microglial. The inflammatory response of these cells was then tested using a Meso scale Delivery (MSD) multiplex ELISA. An MSD ELISA allows for the testing of several analytes simultaneously, using

proprietary plates that have several electrodes and corresponding linkers per well. This works similarly to a sandwich ELISA, except the secondary antibody is conjugated with a SULFO-TAG that can be read by an MSD proprietary plate reader.

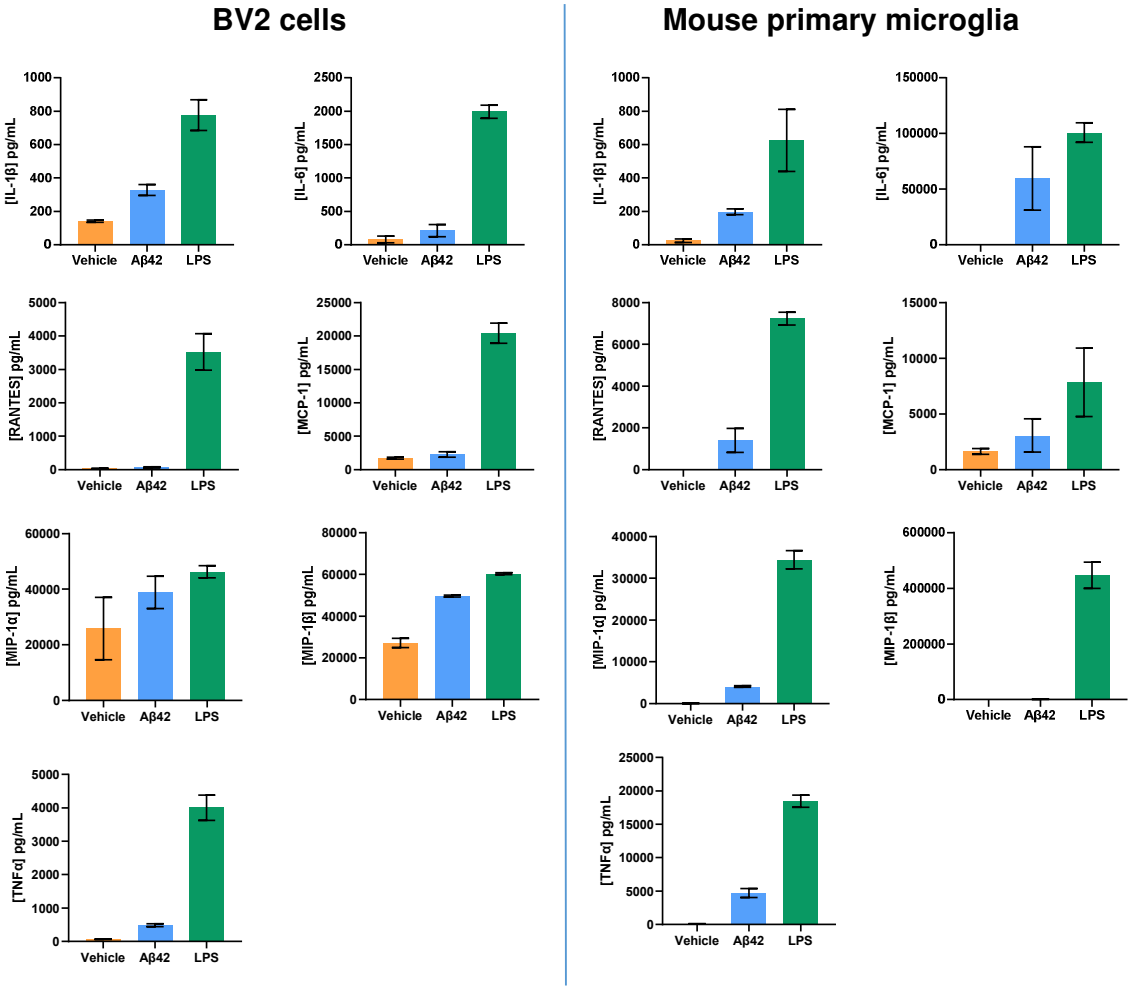

Figure 26: Inflammatory response from BV2 cells vs primary mouse microglia

BV2 cells and primary mouse microglia were treated with 2.5 μM Abcam Aβ42 or 10 ng/mL LPS for 24 hr. An MSD multiplexed ELISA was carried out on a panel of 7 cytokines/chemokines including IL-1β, IL-6, RANTES, MCP-1, MIP-1α, MIP-1β, TNFα. Error bars are mean ± SD of three wells from one biological repeat.

An MSD inflammatory panel was used as an exploratory means to better understand the signalling mechanisms involved in Aβ42-induced inflammation. RANTES, otherwise known as CCL5, is a pro-inflammatory chemokine heavily implicated in AD.[219] The production of RANTES is TRIF-signalling dependent, so the increase in RANTES production in the primary microglia suggests that Aβ42 activates the TRIF

signalling pathway of TLR4 activation (**Figure 26**). Surprisingly, there were quite a few differences between the responses of the two cell types, particularly concerning RANTES and MIP-1β. Perhaps a Luminex screen, a fluorescent bead-based immunoassay that allows for multiplex detection of up to 100 analytes simultaneously would have been a less biased approach as it would have scanned a larger number of inflammatory markers, however this was not available at the time.

3.4.2. Imaging TNFα on the cell membrane

The neuroinflammation assay described in this chapter allows for the bulk measurement of TNFα in the cell supernatant of stimulated microglial cells. While this provides useful information about the neuroinflammatory potential of the stimulants, this assay does not provide an indication of how many cells were activated, or to what extent. Moreover, this assay takes between 24 hours (for high concentrations of toxic aggregates) and 120 hours (for lower concentrations). By directly imaging TNFα on the membrane of these cells, we can directly quantify levels of TNFα per cell, at a much shorter time scale. TNFα is normally cleaved from the membrane by TACE, however this can be prevented by the addition of a metalloprotease inhibitor, such as TAPI-0 (**Figure 27**).

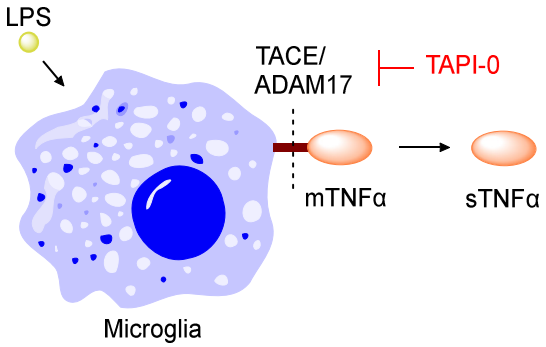

Figure 27: TACE-inhibition

mTNFα = membrane TNFα, *sTNFα* = soluble TNFα, *TAPI-0* = TNFα protease inhibitor

LPS-stimulation causes the trafficking of TNFα to the cell membrane where it is cleaved by TACE (or ADAM17). This cleavage can be inhibited by the metalloprotease inhibitor TAPI-0, preventing the release of soluble TNFα from the membrane. TNFα on the membrane can then be imaged using a fluorescent TNFα antibody.

Cells were plated at a density of 100,000 cells/well in Ibidi treat 8-well imaging slides. At this density, there were enough cells that it was easy to locate them with a confocal

microscope, but not enough to cause cell clumping. Initial experiments using non-fixed cells had significant non-specific binding from the TNFα antibody.

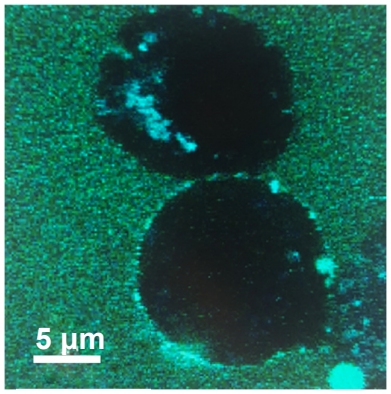

Figure 28: Non-specific binding from TNFα antibody

Representative image of untreated cells labelled with TNFα antibody, taken on a fluorescence-lifetime imaging (FLIM) confocal microscope.

Non-specific binding was reduced by fixing the cells with 2% PFA and blocking with a blocking solution (PBS with 0.5% v/v BSA, 4 µg/mL rat anti-mouse FcγRII/III, 5% v/v rabbit serum).

Autofluorescence was detected at 488 nm in untreated cells without antibody, TAPI-0, or LPS (**Figure 29**). Since most cell autofluorescence is detected at shorter wavelengths, the anti-mouse Alexa Fluor (AF) 488 TNFα antibody was replaced with an AF 647 antibody.

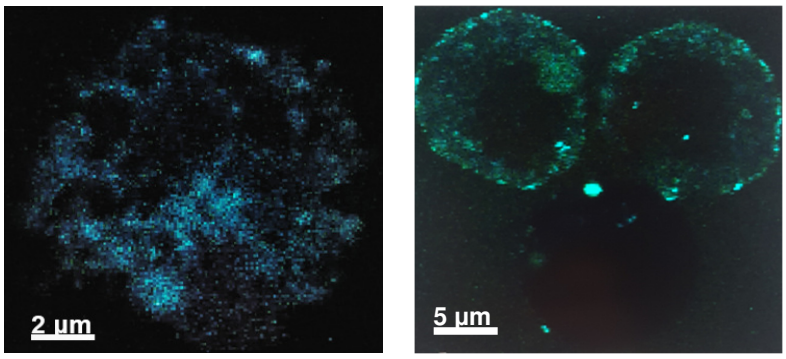

Figure 29: Cell autofluorescence at 488 nm

Substantial autofluorescence was detected from BV2 cells at 488 nm.

Fixing and blocking the cells, as well as switching to the AF 647 antibody, greatly reduced non-specific binding and cell autofluorescence, resulting in cleaner images. An LPS dose-response was carried out to optimise LPS concentration and timescale of these experiments (**Figure 30**).

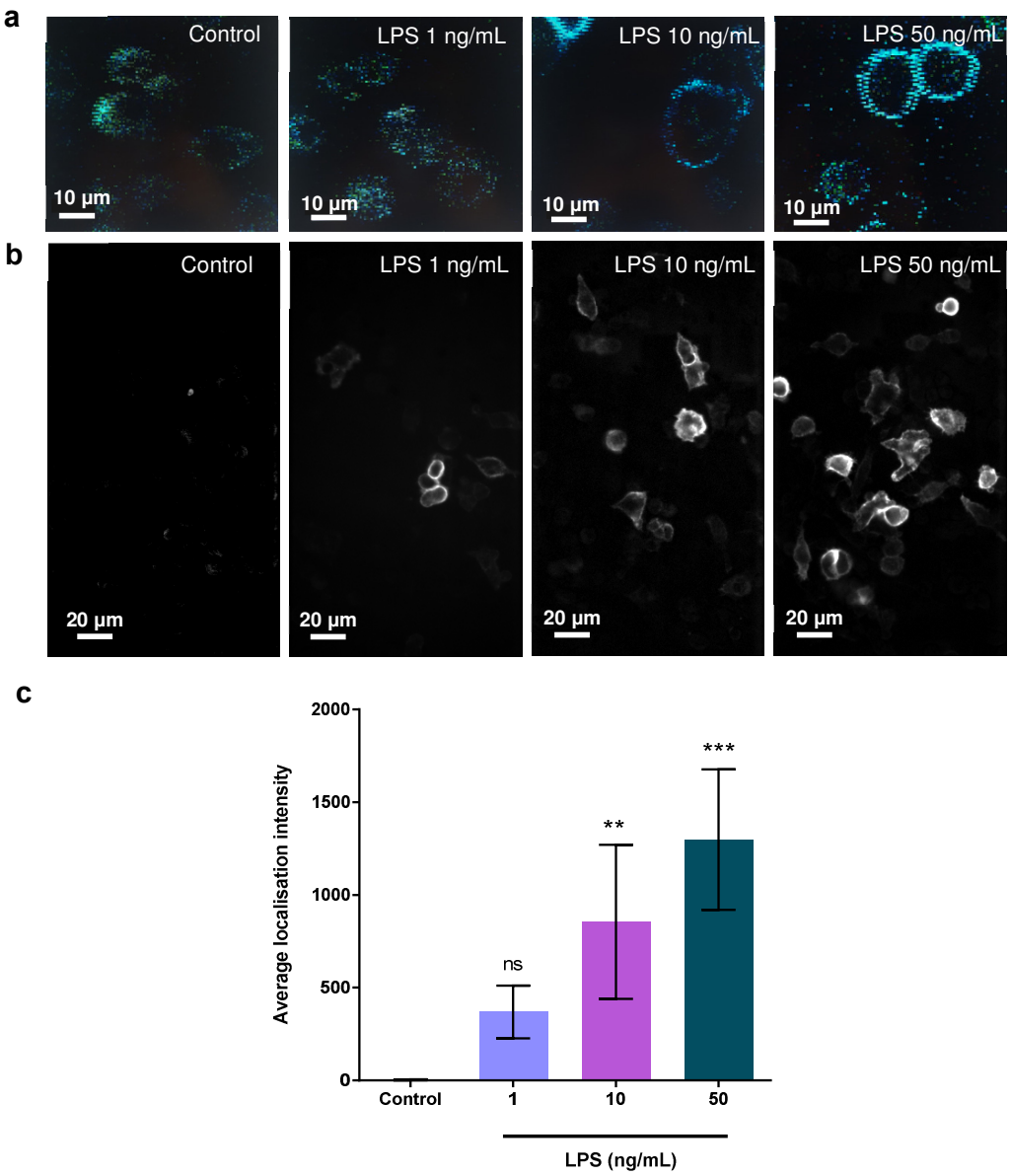

Figure 30: LPS-dose response

(**a**) Representative images of BV2 cells treated with various concentrations of LPS for 2 hr before being fixed and imaged using a confocal FLIM microscope. Reagent concentrations used were 1 µM TAPI-0 and 10 µg/mL (66.7 nM) Alexa Fluor 647 anti-mouse TNFα antibody. (**b**) The same cells were then imaged with an epifluorescence microscope at a lower magnification to increase the number of cells per image. (**c**) The epifluorescence microscope images were analysed in ImageJ by applying a

threshold to the control image with the highest fluorescence intensity. This threshold was then applied to the LPS conditions and the number of localisations above the threshold were counted. Error bars represent the mean ± SD of 10 images. (One-way ANOVA: $F(3, 28) = 17.41$. $p < 0.001$. Post hoc Dunnett test: Control vs 1: $p = 0.27$; Control vs 10: $p = 0.005$; Control vs 50: $p < 0.001$).

Cell autofluorescence and non-specific binding were greatly reduced, and clear bright fluorescent rings were detected in the confocal slices. Two hours of LPS treatment at 10 or 50 ng/mL was sufficient for TNFα detection.

3.5. Conclusions and future work

In this chapter a neuroinflammation assay has been optimised to measure the TNFα release from Aβ42-treated BV2 cells. The conditions that required optimisation included the LPS concentration used as a positive control, the FBS source and concentration, the post-experimental handling of cell supernatant (prior to analysis), as well as the source of Aβ42, its concentration and time course for inflammation. This assay has the sensitivity to detect down to picomolar concentrations of Aβ42 (**Figure 19**). The optimisation of this assay using synthetic Aβ42 was crucial before moving on to more clinically relevant human biofluid samples, of which only low volumes are available. The development of this assay for the analysis of human AD soluble aggregates will be covered in Chapter 4. In future experiments, the conventional one-target ELISA can be substituted with a multiplex ELISA to measure levels of multiple cytokines and chemokines simultaneously.

The current neuroinflammation assay has a few limitations, namely that there is an increase in baseline signal over time, and that the TNFα ELISA experiments are very time-intensive (**Figure 19**). An alternative neuroinflammation assay has been proposed to address these limitations, that uses fluorescence imaging of TNFα directly on the cell membrane. Future experiments could combine this TNFα imaging method with an ImageStream® Flow Cytometer to get more quantitative and higher-throughput measurements, by sorting cells based on fluorescence (TNFα release). The cells could be treated with synthetic Aβ and brain-derived soluble aggregates to assess their agonism on the pathway. Alternatively, instead of using a flow cytometer, unlabelled TNFα antibodies could be coupled with a non-toxic dye (e.g. Incucyte® Fabfluor-488 antibody labeling dyes) and the cells could be imaged live using an Incucyte® live-cell imaging system. Another idea would be to stain Aβ42 aggregates with a pH-sensitive fluorophore (e.g. Incucyte® pHrodo® Red Cell Labeling Kit for

Phagocytosis) and assess microglial phagocytosis of Aβ42, similarly to what has been reported previously.[220] Furthermore, instead of using BV2 immortalised cells for these experiments, switching to primary mouse microglia would make the assay a more relevant model of neuroinflammation. However, microglial genes are not very well conserved between mice and humans, resulting in large biochemical and pharmacological differences. Some examples include TLR, FCγ, and SIGLEC receptors which are highly expressed in human but not mouse microglia, different expression of several transcription factors, disparities in cell proliferation and NO production, varied responses to species-specific cell surface antigen presentation proteins, and opposite responses to certain drugs such as valproic acid and propentofylline.[221–223] There is also limited overlap of microglial genes regulated during ageing, suggesting a difference in the way mouse and human microglia age.[222] For these reasons, using primary human microglia or iPSC-derived microglia would be more clinically relevant as they would better reflect the human condition.

A proprietary anti-Aβ42 MedImmune antibody, that binds to the C-terminus of the Aβ42 peptide, has been tested using a variety of assays to measure its effects on the inflammatory response, liposome permeability, and its binding efficiency. The immunoprecipitation experiment in conjunction with the neuroinflammation experiments, suggested that the antibody has a high affinity for monomeric and early aggregated species of Aβ42, and a potentially lower affinity for Aβ42 fibrils. This was seen through the reduction of TNFα production when the antibody was pre-incubated with monomeric Aβ42, slowing down aggregation kinetics (**Figure 23**), but not having an effect when added simultaneously with Aβ42 aggregates to the cells (**Figure 22d**), which would have quickly adopted fibrillar structures at 37°C, suggesting that the epitope is hidden in the fibrillar aggregates. This is supported by a conformational analysis of the Aβ42 peptide, suggesting that the C-terminus may be embedded in the core of Aβ fibrils.[224] Another explanation could be that the antibody is ineffective due to the length of the aggregates, which require complete coverage by antibodies in order to block the inflammatory response. This explanation is unlikely however as the antibody was added at a concentration 1000-fold higher than the IC50 (165.1 ng/mL, ~1.1 nM) determined using the liposome assay. The liposome assay also showed that the antibody can reduce calcium influx caused by Aβ42-mediated liposome permeabilisation in a concentration-dependent manner (**Figure 24**).

Seeing as the antibody can bind to monomeric and early aggregate species of Aβ42 and slow down aggregation, this antibody could potentially be administered as a preventative drug to patients with mild cognitive impairment and therefore at risk of developing AD, or early AD patients before symptom onset. Early administration could potentially slow the aggregation of inflammatory Aβ42 aggregates by blocking the C-terminus, which may play an important role in the structural stability and assembly of Aβ42.[225] This antibody would most likely not be very effective in patients with more advanced AD, as the antibody does not effectively bind Aβ42 fibrils, or reduce aggregate-induced inflammation. Total Aβx-42 concentration, without denaturation, in homogenised AD brain is in the high picomolar - low nanomolar regime, and soluble Aβx-42 is found in low-high picomolar concentrations.[178] The IC_{50} of the MedImmune antibody was calculated to be just over 1 nM using a physiologically relevant concentration of Aβ42 (5 nM). In order to achieve complete inhibition, the antibody would need to be in the brain at a concentration over ~6.6 nM (1 µg/mL), according to the 4-parameter fit (**Figure 24**) and would have to be administered at 1000-fold concentration as antibody concentrations in the brain are generally around a thousand times lower than in the blood, due to poor BBB permeability. Exact antibody concentrations would depend on pharmacokinetic studies on animals, the body clearance of the drug, and the individual weights of the patients.

The neuroinflammation, liposome-permeabilisation, and immunoprecipitation assays, as described in this chapter are now set up for the preclinical testing of more passive immunotherapies in the future.

4: Characterisation of Soluble Aggregates from AD Brain

Parts of this chapter have been adapted from the following soon-to-be published manuscript:

Dimitrios I. Sideris, John S. H. Danial, Derya Emin et al. Soluble amyloid beta-containing aggregates are present throughout the brain at early stages of Alzheimer's disease (accepted in Brain Communications, May 2021).

The liposome assay was carried out by Dr Suman De and Zengjie Xia; AD PAINT was carried out by Dr John Danial and Dr Jason C. Sang; AFM was carried out by Dr Francesco Simone Ruggeri; SiMPull was carried out by Derya Emin, Yu P. Zhang, and Dr Evgenia Lobanova.

4.1. Introduction

Protein aggregation likely plays a key role in the initiation and spreading of Alzheimer's disease through the brain. Soluble aggregates of Aβ are believed to play a key role in this process. However, the aggregates present in humans are still poorly characterised due to a lack of suitable methods required for characterising the low concentration of heterogeneous aggregates present. A variety of sensitive biophysical methods have been employed to characterise the aggregates present in human AD brains at Braak stage III.

AD has a typical pathological progression, starting in the hippocampal/entorhinal cortex regions and spreading to the temporal, parietal, and frontal lobes before affecting the occipital lobe.[18,226] For our initial experiments we decided to study the soluble aggregates from Braak stage III brain tissue, which is at the early stages of disease and therefore before the appearance of global pathology, to assess regional variability within the same patient and between patients.[16,227] After establishing that our assays have sufficient sensitivity to detect the aggregates present, we characterised the soluble aggregates from eight brain regions from three Alzheimer's disease patients. Two distinct regions were then chosen to compare in more detail, the hippocampus (HPC), which is significantly affected early in the disease, and the visual association cortex (VAC), a region affected later in the disease, with the latter acting as an internal control for each brain. The similarities and differences between the soluble aggregates in these regions have been identified by characterising their size, structure, neurotoxicity, inflammatory potential, and capability to permeabilise a lipid membrane.

4.2. Overview of assays used to characterise soluble aggregates

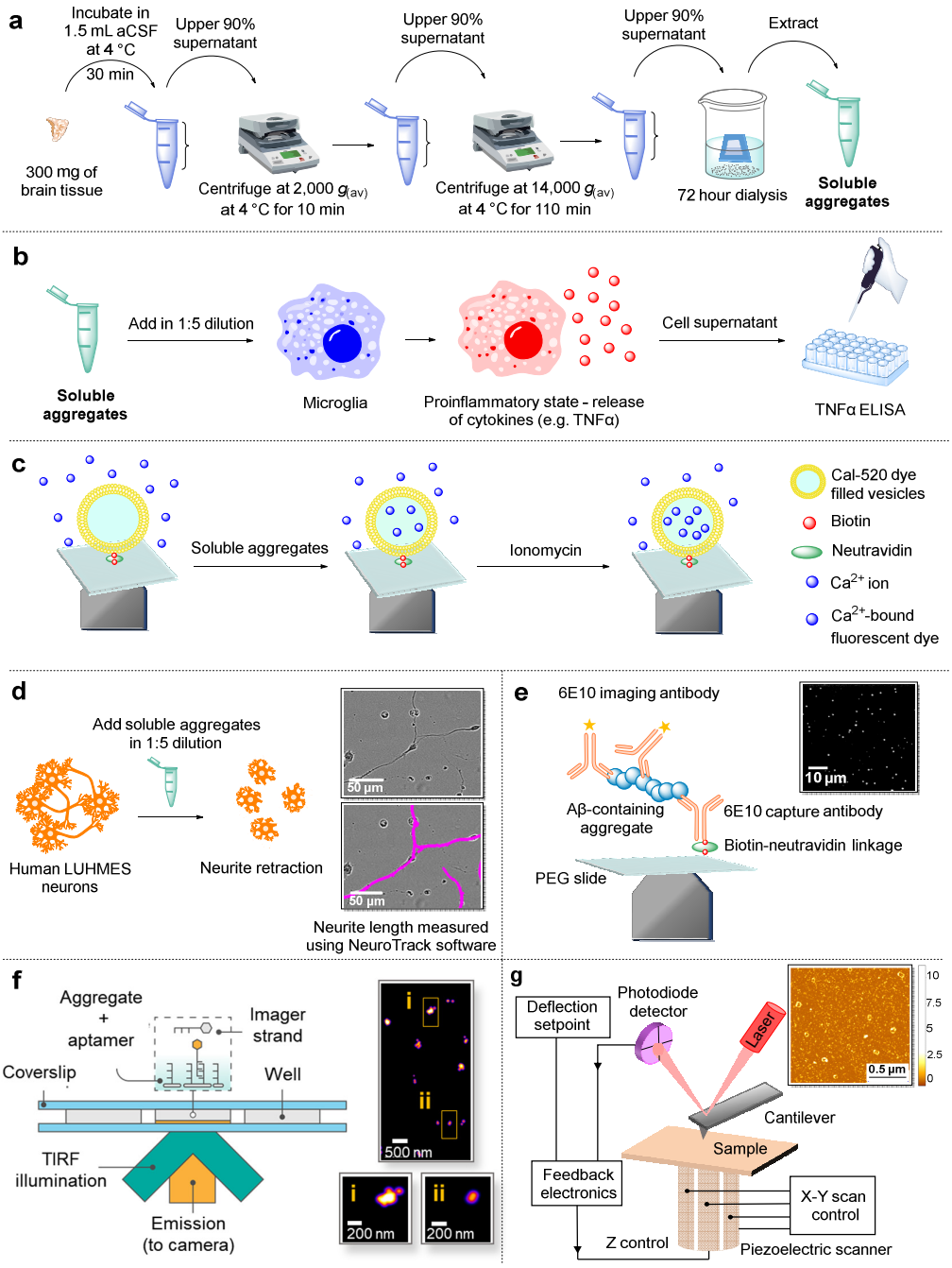

Figure 31: Overview of assays used in this chapter to characterise soluble aggregates

aCSF = artificial cerebrospinal fluid, *TIRF* = total internal reflection fluorescence

(**a**) Extraction of soluble aggregates from human brain tissue through soaking in aCSF. (**b**) Neuroinflammation assay using BV2 cells to measure production of TNFα. (**c**) Liposome assay used to measure the aggregates' ability to penetrate a lipid membrane. (**d**) Neurite length assay used to

measure neurotoxicity. (**e**) Single-molecule pull-down imaging used for the characterisation of Aβ-containing aggregates. (**f**) Aptamer DNA-PAINT imaging used to characterise the size and number of aggregates. (**g**) AFM imaging of 3-D morphology used to characterise morphology and cross-sectional dimensions of the aggregates.

4.3. Optimisation of brain soaking prep

Initially, with the help of our lab technician Helen Dakin at the Dementia Research Institute (DRI) in Addenbrooke's hospital, we reproduced the extraction process of soluble aggregates from soaking brain tissue as previously described (**Figure 32**).[178]

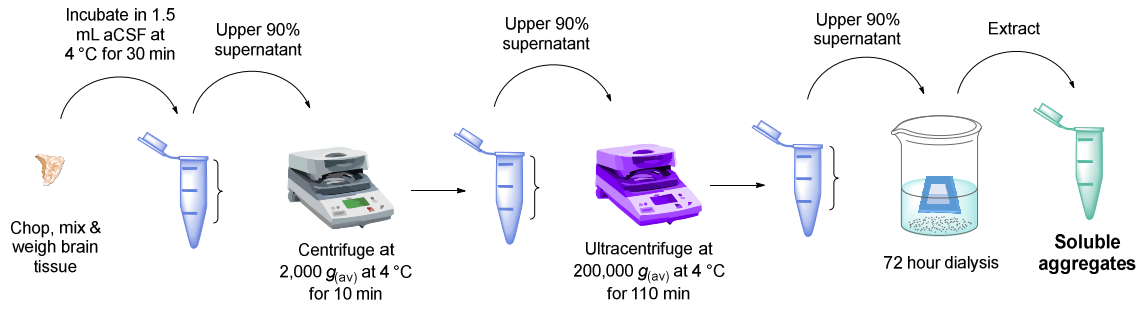

Figure 32: Initial brain soaking prep as previously reported[178]

Brain tissue is chopped, mixed, and weighed before being soaked in aCSF buffer. The soluble aggregates are extracted from the brain tissue after several centrifugation steps, including an ultracentrifugation step, and a 72-hr dialysis.

There were a few steps in the protocol that could be improved for reproducibility and convenience of future preps. A standardised weight of 300 mg was chosen for the brain tissues going forward, to reduce variability between preps. To assess intra-tissue variability, three different cuts of the same brain tissue were passed through the prep and the amount of soluble protein produced was measured (**Figure 33a**).

Furthermore, access to an ultracentrifuge was limited, so the necessity of ultracentrifugation of these samples was assessed by comparing ultracentrifugation and benchtop centrifugation (**Figure 33b**). Moreover, the 72-hour dialysis step increased the length of the brain soaking prep by 3 days, so its necessity was also assessed by comparing dialysed and undialysed samples (**Figure 33c**).

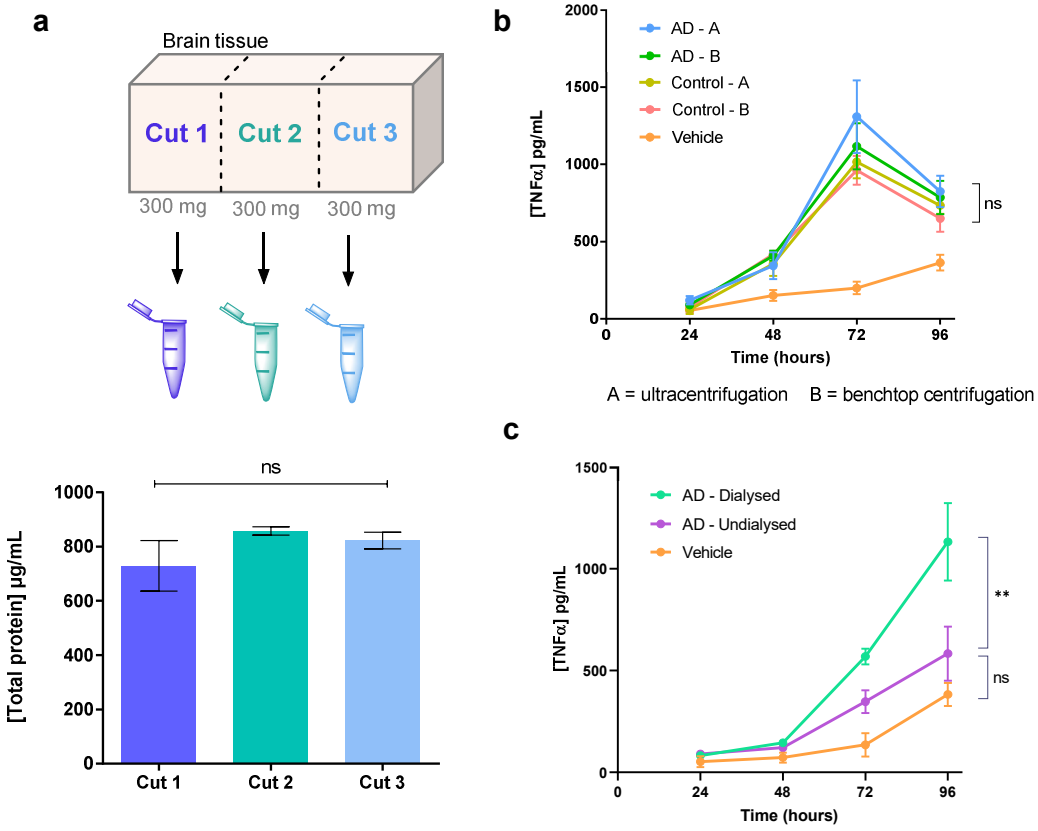

Figure 33: Optimisation of brain soaking protocol

(**a**) Frontal cortex brain tissue from patient AD2 was cut into three 300 mg pieces. The soluble proteins were extracted from these pieces through soaking, and their total protein content was measured with a BCA assay. Error bars represent the mean ± SD of three wells. (One-way ANOVA: $F(2, 3) = 2.663$. Post hoc Tukey test: Cut 1 vs Cut 2: $p = 0.2111$; Cut 1 vs Cut 3: $p = 0.3636$; Cut 2 vs Cut 3: $p = 0.8251$). (**b**) BV2 cells were treated for 96 hr with brain-derived soluble aggregates prepared either with ultracentrifugation or benchtop centrifugation. TNFα responses were measured by ELISA. Error bars represent the mean ± SD of three wells. (One-way ANOVA: $F(3, 8) = 2.069$, $p = 0.18$. Post hoc Tukey test: Control-A vs Control-B: $p = 0.68$; AD-A vs AD-B: $p = 0.95$). (**c**) BV2 cells were treated for 96 hr with soluble aggregates prepared with or without a dialysis step. TNFα responses were measured by ELISA. Error bars represent the mean ± SD of three wells. (One-way ANOVA: $F(2, 6) = 23$, $p = 0.001$. Post hoc Tukey test: Vehicle vs Dialysed: $p = 0.001$; Vehicle vs Undialysed: $p = 0.26$; Dialysed vs Undialysed: $p = 0.007$).

The three different cuts from the same piece of brain tissue did not have significant variability in their total soluble protein content (**Figure 33a**). For this reason, it was assumed that there wasn't significant intra-tissue variability for any of the regions.

Centrifugation was used to remove cell debris. The type of centrifugation did not appear to influence the inflammatory potential of the soluble aggregates (**Figure 33b**). For this reason, the ultracentrifugation step was replaced with benchtop centrifugation at 14,000 $g_{(av)}$.

Dialysis was used to remove any small molecules from the samples that might affect our assays, such as excitatory amino acids and other DAMPs. Dialysed samples were significantly more inflammatory than undialysed samples (**Figure 33c**), possibly due to unremoved anti-inflammatory agents in the undialysed samples. This suggested that this step was critical and was therefore kept for future preps.

4.3.1. Non-AD controls

To identify whether the soluble aggregate-induced inflammation is AD-specific, comparisons should be made with negative (non-AD) control brain. However, finding suitable negative control brain is very challenging, as it requires finding age-matched controls who have not passed away from brain/spinal cord injuries/illnesses that might affect brain cell machinery and also have no AD pathology or cognitive impairment. This is complicated further by the fact that non-demented elderly individuals often present substantial plaques and tangles without cognitive issues.[228–231] It is also important to note that the AD brains analysed in this study were from Braak stage III (early disease) and are therefore not likely to display big differences to age-matched non-demented brains that will also have pathology. This was confirmed by treating BV2 cells with soluble aggregates extracted from our three AD brains, and from one age-matched control brain, for 96 hours.

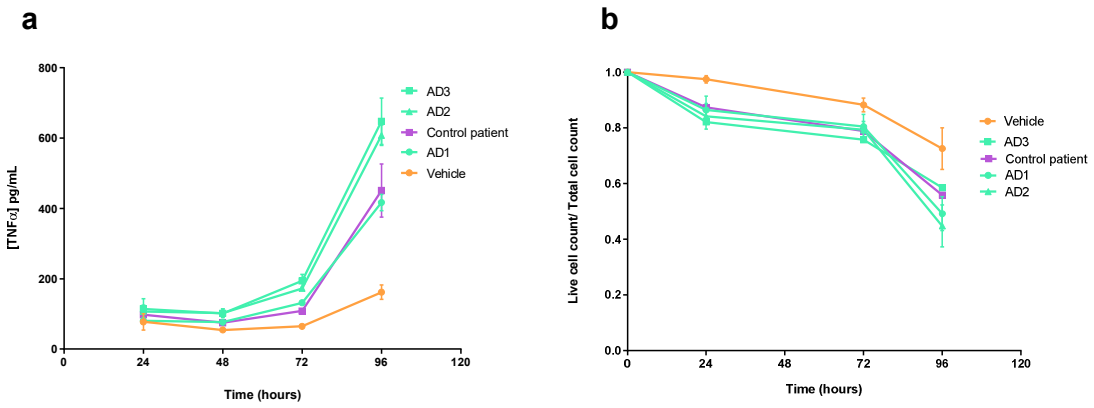

Figure 34: AD brain vs control

(**a**) BV2 cells were treated with frontal cortex-derived soluble aggregates from three AD patients and one non-AD control. TNFα in cell supernatant was measured by ELISA. Error bars represent the mean ± SD of three wells. (**b**) Live and dead cells from the neuroinflammation experiment were counted with Trypan Blue staining. Error bars represent the mean ± SD of three wells.

As expected, great variability was observed in the neuroinflammatory response when comparing between patients and there was no clear difference between AD vs control brain (**Figure 34a**). There also does not appear to be a difference between AD vs control in the live cell counts (**Figure 34b**). It should be noted that the control patient's cause of death was due to a malignant tumour in the spinal cord, and had neurofibrillary tangle pathology (**Table 2**), further highlighting the difficulty in obtaining suitable control brain. Studies focusing on later stages of disease progression (e.g. Braak stage VI), would benefit more from a comparison with age-matched control brain than early disease studies. Due to the complexity of finding suitable negative control brain, and our focus being on the early stages of the disease, negative control brains were not investigated further.

4.3.2. Brain survey

With an optimised brain soaking prep, eight different brain regions from three AD patients were analysed (**Figure 35a**). These regions spanned areas that are typically affected early in disease, and regions that are affected later in disease.

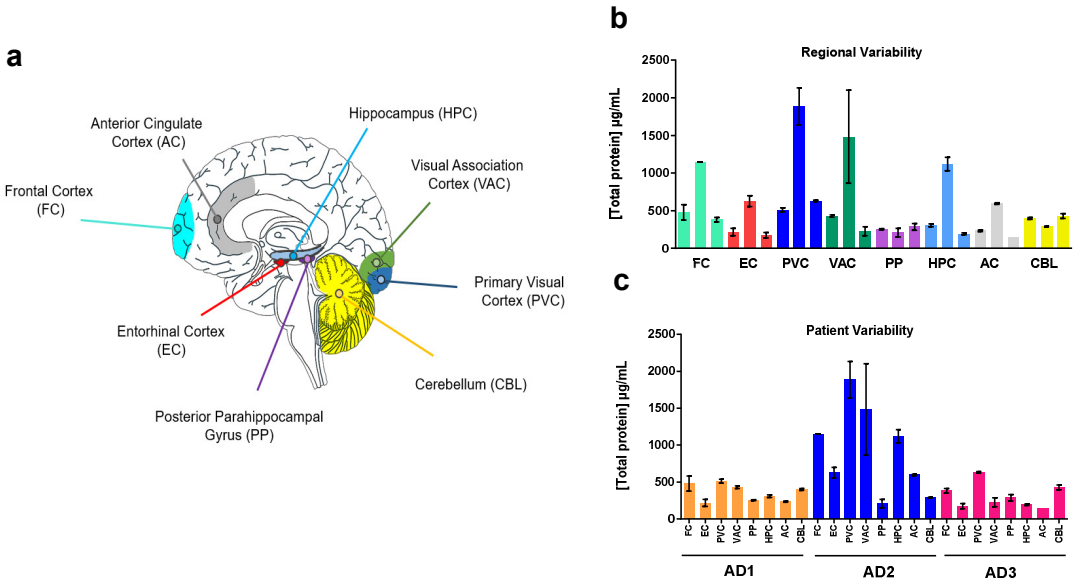

Figure 35: AD brain regions analysed

FC = frontal cortex, *EC* = entorhinal cortex, *PVC* = primary visual cortex, *VAC* = visual association cortex, *PP* = posterior parahippocampal gyrus, *HPC* = hippocampus, *AC* = anterior cingulate cortex, *CBL* = cerebellum

(**a**) Diagram of the 8 regions that were removed, soaked, and used for experimentation, from three AD patients (Braak stage III). Total protein concentrations of these regions were measured with BCA and presented as (**b**) regional variability, where each bar represents a different patient (AD1, AD2, AD3), or (**c**) patient variability, where each bar represents a different brain region. Error bars represent the mean ± SD of three technical repeats.

Great variability was observed in the total protein concentrations of the soluble aggregate samples when comparing region-to-region (**Figure 35b**) or patient-to-patient (**Figure 35c**). For this reason, the soluble aggregate samples were normalised to the brain starting weight (300 mg) instead of their total protein concentration.

4.4. Neuroinflammation assay with soluble aggregates

BV2 cells were treated with the soluble aggregates derived from eight different regions from three AD patients to assess their inflammatory potential.

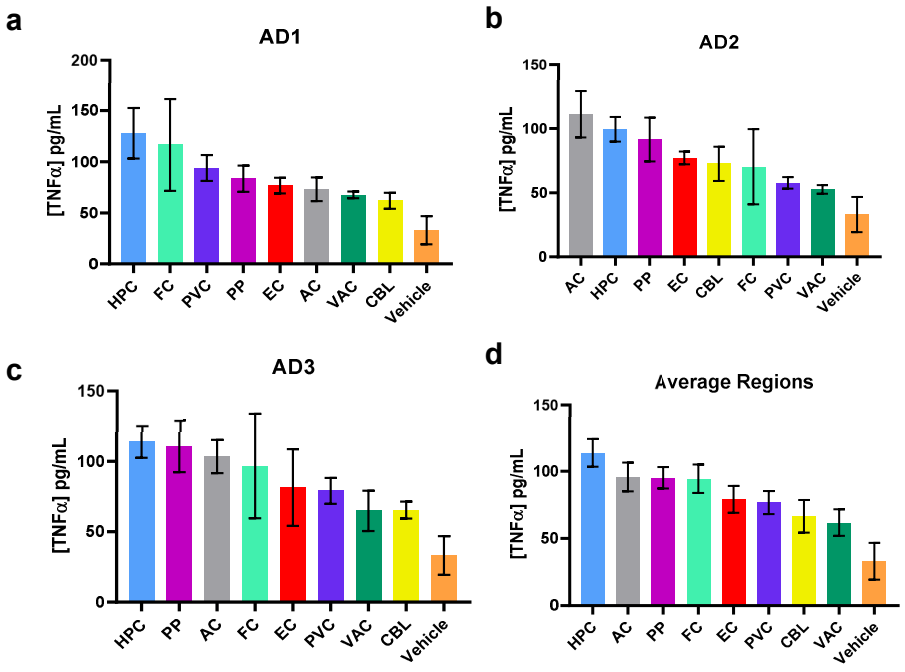

Figure 36: Initial neuroinflammation brain survey

FC = frontal cortex, *EC* = entorhinal cortex, *PVC* = primary visual cortex, *VAC* = visual association cortex, *PP* = posterior parahippocampal gyrus, *HPC* = hippocampus, *AC* = anterior cingulate cortex, *CBL* = cerebellum

The 120 hr timepoint of BV2 cells treated with a 1:5 dilution of soluble aggregate samples from eight brain regions from (**a**) AD1, (**b**) AD2 and (**c**) AD3. (**d**) The average values from the three AD patients. TNFα in the cell supernatant was measured by ELISA. Vehicle control was aCSF at the same dilution as soluble aggregate samples. Error bars represent the mean ± SD from three wells.

The samples from all three AD patients produced similar levels of TNFα and were all higher than the vehicle control **(Figure 36a-c)**. The hippocampal samples appeared to be the most inflammatory overall **(Figure 36d)**. However, the responses were not very strong making it difficult to identify differences between the different regions. To improve this signal, the neuroinflammation assay was re-optimised for use with soluble aggregates.

4.4.1. Cell density optimisation

48-well microplates have a working volume of 300 µL. To reduce the volume of sample required for this assay, the 48-well microplates were replaced with 96-well microplates, with a working volume of 150 µL. This change was crucial for the use of precious clinical samples, where only small volumes were available. 96-well microplates have been used for similar TNFα studies, where BV2 cells were treated with toxic aggregates.[216,232] To determine the optimal density of cells that would provide the strongest response, while maintaining low basal TNFα levels for the vehicle control, cells were plated at various densities and treated with soluble aggregates.

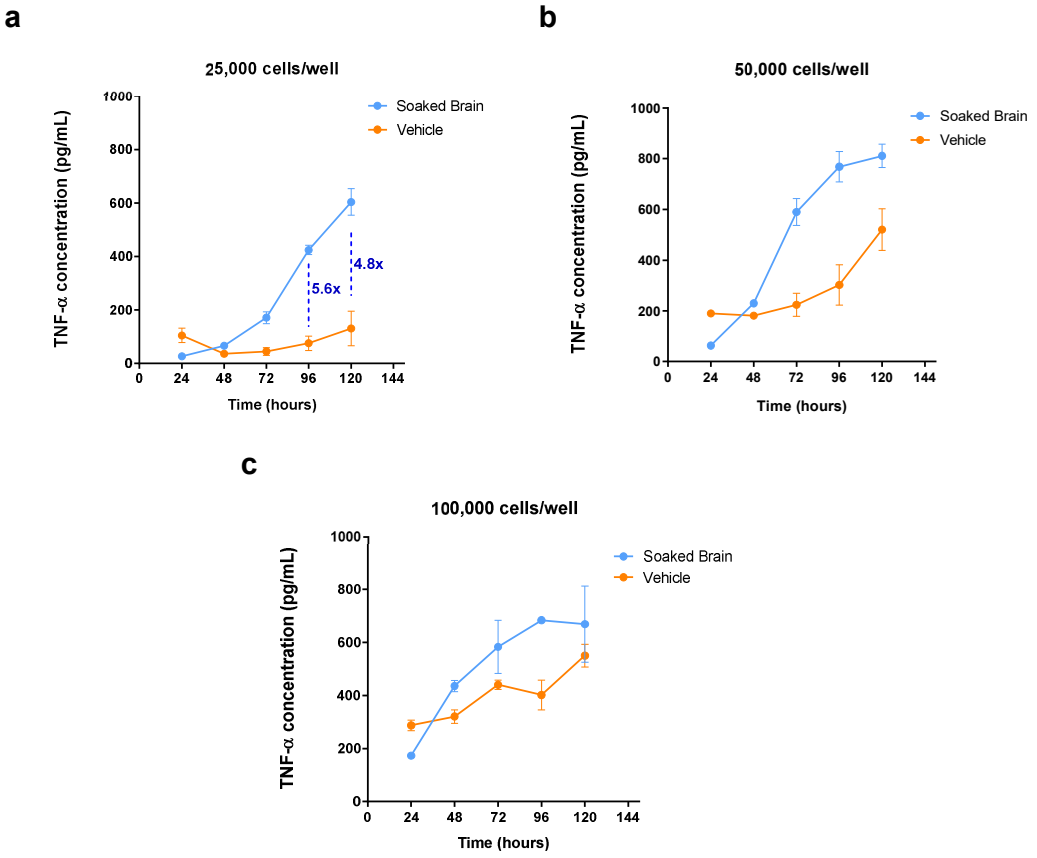

Figure 37: Cell density optimisation

BV2 cells were plated in 96-well microplates in three densities, (**a**) 25,000 cells/well, (**b**) 50,000 cells/well and (**c**) 100,000 cells/well. They were treated with AD hippocampus-derived soluble aggregates at a 1:5 dilution (from patient AD1). Vehicle control was aCSF at 1:5 dilution. Error bars represent the mean ± SD from three wells.

Due to the low concentrations of these soluble aggregate samples, it took longer than 24 hours for a detectable inflammatory response to occur. The vehicle control TNFα levels tended to increase with time, as the cells became more confluent. Cells plated at lower densities had the least stressed vehicle control wells, without compromising the soluble aggregate-derived inflammatory response, thus giving the cleanest signal.

In **Figure 37a,** at the 96-hour time point there was a 5.6-fold difference between the vehicle control and the soluble aggregate-treated cells, and a smaller 4.8-fold difference at the 120-hour time point. Shortening the length of these experiments also reduced the sample volume required for each experiment, as media (containing soluble aggregates) was replaced every 24 hours. For these reasons, 96 hours was chosen as the optimal treatment time for future soluble aggregate experiments, with a cell density of 25,000 cells/well. The brain survey was repeated with the optimised conditions.

4.4.2. Global inflammation in the brain of Braak stage III patients

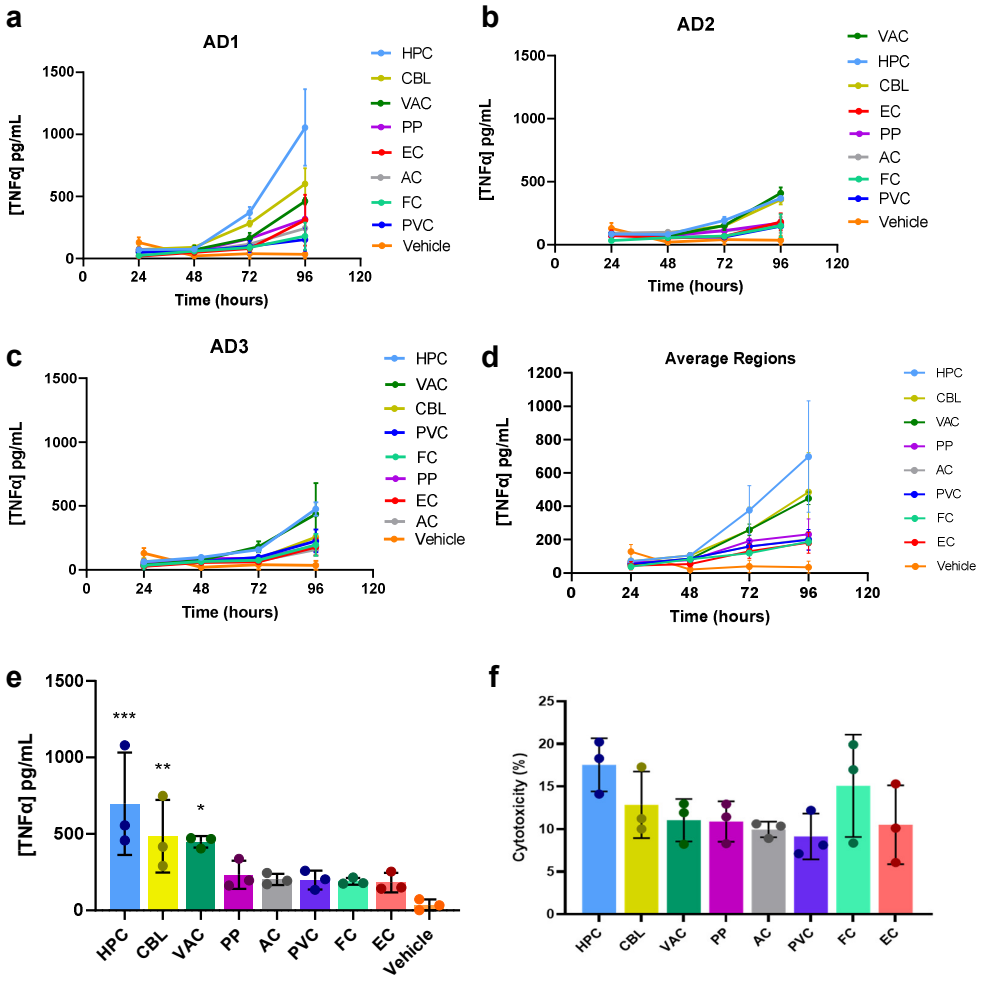

Figure 38: Brain survey neuroinflammation and cytotoxicity

FC = frontal cortex, *EC* = entorhinal cortex, *PVC* = primary visual cortex, *VAC* = visual association cortex, *PP* = posterior parahippocampal gyrus, *HPC* = hippocampus, *AC* = anterior cingulate cortex, *CBL* = cerebellum.

TNFα response from BV2 cells treated with soluble aggregate samples (diluted 1:5) from eight different brain regions, from three patients (**a**) AD1, (**b**) AD2, (**c**) AD3. Error bars are mean ± SD from three wells. (**d**) The TNFα response averaged by region; each point represents an average from three different Alzheimer's disease patients. Vehicle control was aCSF at equal volume to soluble aggregate samples. LPS at 10 ng/mL was used as a positive control (not shown). Connecting lines have been added for visual clarity. Error bars are mean ± SD. (**e**) TNFα measurements from the 96-hr time point of the neuroinflammation assay. Each point represents one of the three Alzheimer's disease patients. Error bars are mean ± SD. Statistical analysis has been carried out relative to the Vehicle control (One-way ANOVA: $F(8, 18) = 5.989$, $p < 0.001$. Post hoc Dunnett test against Vehicle: HPC: $p < 0.001$; CBL: $p = 0.008$; VAC: $p = 0.02$; PP: $p = 0.46$; AC: $p = 0.62$; PVC: $p = 0.64$; FC: $p = 0.69$; EC: $p = 0.74$).

(**f**) Cell viability was assessed from cell supernatant from the 96-hr time point of the neuroinflammation assay using an LDH assay. Each point represents one of three Alzheimer's disease patients. Data set has been normalised to lysed cells (100%) and the supernatant from the vehicle control on day 0 (0%). Error bars are mean ± SD.

Samples from all eight regions appeared to be inflammatory and cytotoxic to varying degrees (**Figure 38**). This suggested that there was global pathology even at Braak stage III. Despite patient-to-patient variability, hippocampal aggregates appeared to be the most (or second most) toxic in all three patients (also seen in **Figure 36**).

Going forward, two regions were chosen and analysed in more detail. These regions were the hippocampus, which is affected early in disease, and the visual association cortex, which is generally affected later in AD progression, and therefore served as an internal control for each brain. Interestingly, there is a subset of AD patients who have posterior cortical atrophy, with the visual cortex being the primary site of amyloid pathology,[233] however it was confirmed by the neuropathologist at the Cambridge Brain Bank, that this was not the case for the patients in this study.

Surprisingly, the soluble aggregates from the entorhinal cortex, an area with strong pathology, were not very inflammatory, and aggregates from the cerebellum, a region that does not develop mature neuritic amyloid plaques, only diffuse plaques in about half of AD patients,[234] were very inflammatory.

The frozen supernatant from the previous 96-hour neuroinflammation experiment (**Figure 38d**) was further analysed using an MSD multiplexed ELISA inflammatory panel (**Figure 39**). Due to space limitations on the 96-well MSD plate, and the cost of these experiments, only HPC and VAC were analysed for all three patients.

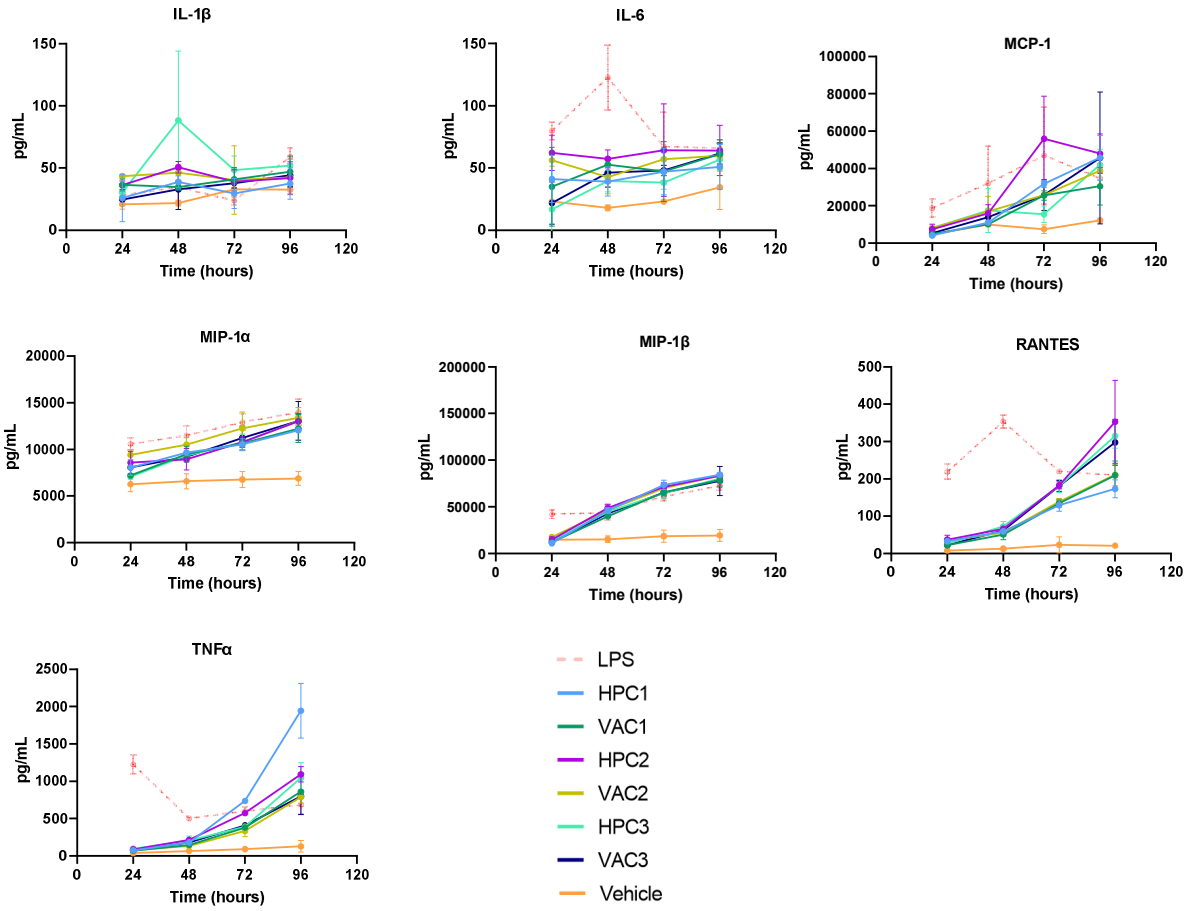

Figure 39: Survey of inflammatory markers

Frozen supernatant from BV2 cells treated with 1:5 HPC and VAC aggregates for 96 hr were analysed using an MSD multiplexed ELISA inflammatory panel. Error bars are mean ± SD from two wells.

Before carrying out the MSD experiment, the supernatant had been freeze-thawed twice; once for carrying out the TNFα brain survey, and once for carrying out the LDH assay. This might have caused the breakdown of certain cytokines and chemokines, especially IL-1β and IL-6, which do not appear to have caused a proper response, compared to **Figure 26**. It should also be noted that MIP-1α and MIP-1β responses were larger than the standard range provided by the kit and might therefore not be entirely accurate.

4.4.3. Neuroinflammation assay with primary mouse microglia

HPC and VAC samples from patient AD1 were added to primary mouse microglia (same batch of cells as **Figure 25**), and the inflammatory response was measured using a TNFα ELISA.

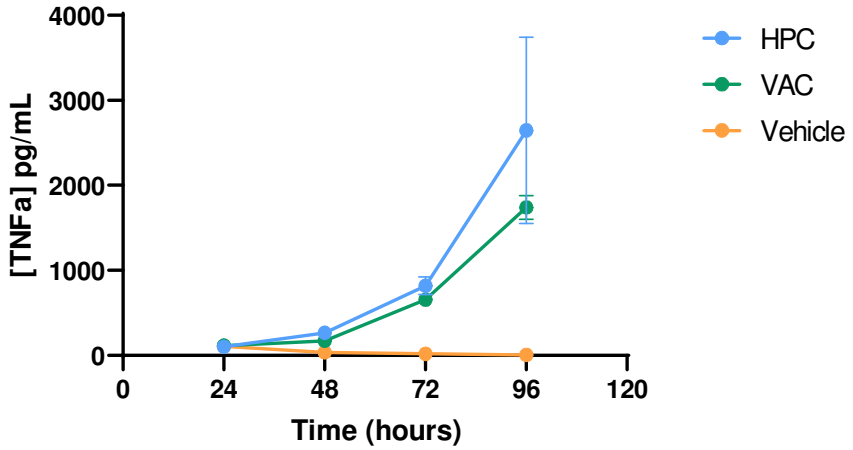

Figure 40: Primary mouse microglia inflammatory response to soluble aggregates

Primary mouse microglia were plated at 50,000 cells/well for 2 days prior to a 96-hr treatment with HPC and VAC (from patient AD1) at a 1:5 dilution. Vehicle control was aCSF buffer at a 1:5 dilution. LPS concentration was 10 ng/mL (not shown). Error bars represent mean ± SD from three wells.

BV2 cells treated with HPC and VAC soluble aggregates (from patient AD1) produced a strong inflammatory response (**Figure 40**). Unfortunately, this experiment could not be repeated with samples from the other two patients due to COVID-19 limited access to primary cells.

These cells were also treated with CellEvent Senescence Green Probe, a stain for β-galactosidase, to measure cell senescence. Microglial cell senescence has been reported to play an important role in AD pathology.[53,235] Cells that undergo senescence are irreversibly arrested at the G1 phase of the cell cycle, however they remain metabolically active. In the case of AD, microglial senescence may impair neuron-sustaining functions and lead to the continuous release of pro-inflammatory cytokines and chemokines.[235]

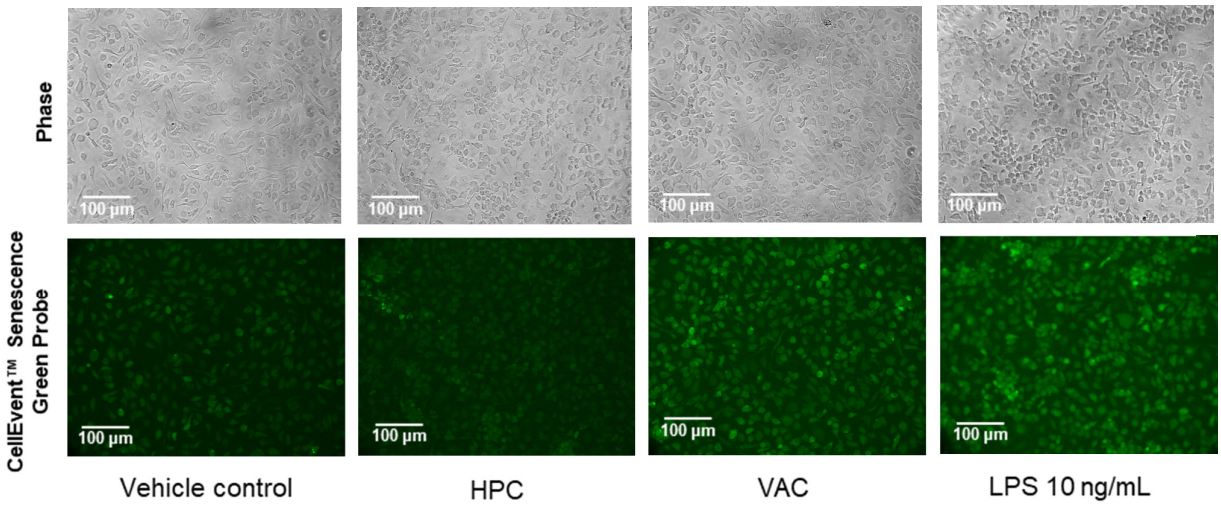

Figure 41: Cell senescence

Primary mouse microglia were plated at 50,000 cells/well for 2 days prior to a 96-hr treatment with HPC and VAC soluble aggregates (from patient AD1) at a 1:5 dilution. Vehicle control was aCSF buffer at a 1:5 dilution.

Treatment with soluble aggregates from HPC and VAC did not appear to cause cell senescence (**Figure 41**). Interestingly, LPS treatment also did not result in cell senescence, contrary to what has been shown previously with several cell types of macrophages.[236–238] Perhaps an anti-cancer drug (i.e. palbociclib) would be a more appropriate positive control for senescence,[239,240] however due to COVID-19, access to primary cells was restricted and primary cell experiments could not be repeated.

4.5. Soluble aggregates are liposome-permeable

This work was carried out by Dr Suman De and Zengjie Xia.

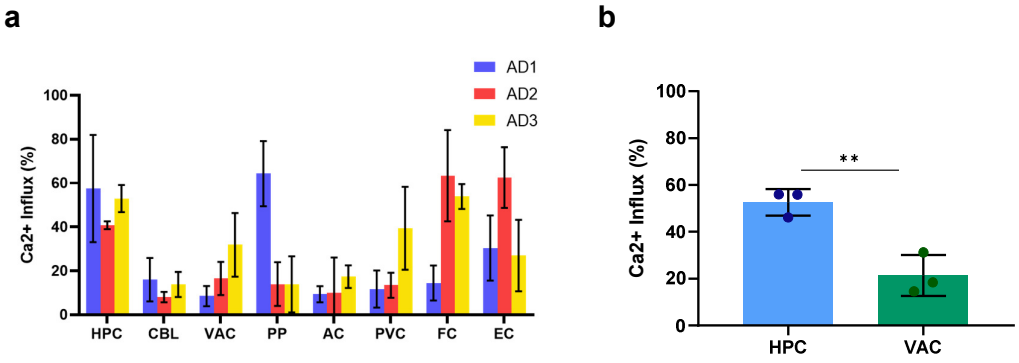

Figure 42: Liposome permeability

(**a**) Ca^{2+} influx of each patient and region measured by liposome assay. Error bars are mean ± SD of 9 fields of view. HPC and VAC samples have been repeated in an independent experiment and show a similar trend. (**b**) Ca^{2+} influx from two repeat experiments, averaged by brain region (HPC and VAC). Each point represents one of three Alzheimer's patients. Error bars are mean ± SD. (HPC vs VAC: n = 3, p = 0.007, t_4 = 5.201).

All brain regions from the three AD patients caused varying amounts of Ca^{2+} influx (**Figure 42a**), a measure of liposome permeability. The HPC samples caused significantly higher Ca^{2+} influx than the VAC samples (**Figure 42b**), suggesting that the HPC aggregates have a property that might make them more liposome-permeable.

4.6. TLR4-mediation of inflammatory response

TLR4 is the receptor most strongly associated with the production of TNFα and plays a central role in AD pathology by regulating neuroinflammation. To determine whether the soluble aggregate-induced TNFα response is mediated through TLR4, TLR4 inhibitors TAK242 and RSLA were tested. TAK242, otherwise known as Cli-095, is a small molecule inhibitor that binds to the intracellular domain of TLR4, specifically the Cys747 residue, preventing TLR4 interaction with adaptor molecules TIRAP and TRAM. RSLA, lipid A from *Rhodobacter sphaeroides* bacteria, is a potent inhibitor of LPS and therefore TLR4 signalling. Prior to using soluble aggregates, the inhibitors were tested with LPS to assess their functionality.

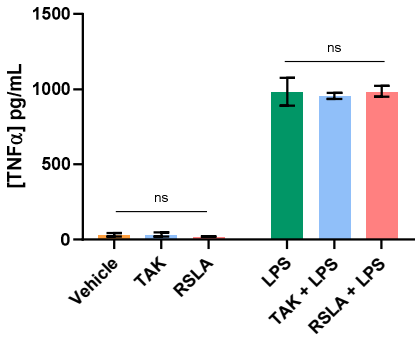

Figure 43: TLR4 inhibitors

BV2 cells plated at 50,000 cells/well were treated with LPS and 1 μM TAK or RSLA for 24 hr. Vehicle was DMSO in distilled water at same dilution as inhibitors. LPS concentration was 10 ng/mL. TNFα in cell supernatant was measured by ELISA. Error bars represent the mean ± SD from three wells. (One-way ANOVA for Vehicle, TAK, RSLA: $F(2, 6) = 1.413$, $p = 0.31$. One-way ANOVA for LPS, TAK+LPS, RSLA+LPS: $F(2, 6) = 0.2522$, $p = 0.78$).

Both TLR4 inhibitors did not reduce the TNFα response from LPS-treated BV2 cells (**Figure 43**). To ensure that the inhibitor concentrations and incubation times were sufficient to get a response, this experiment was repeated with a higher concentration of TAK242 and was also incubated for 4-5 hours prior to the addition of LPS.

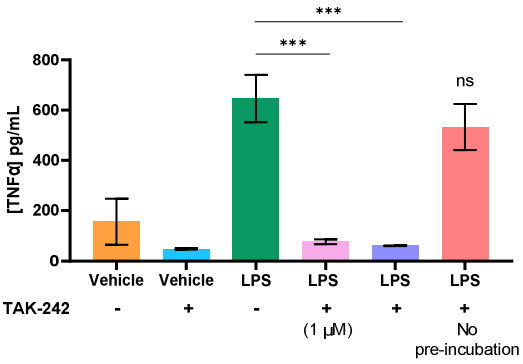

Figure 44: TAK242 longer incubation

BV2 cells plated at 25,000 cells/well were pre-treated with 1 μM (pink) or 3 μM TAK242 for 4-5 hr. Vehicle was DMSO in distilled water at same dilution as TAK242. LPS concentration was 10 ng/mL. Error bars represent the mean ± SD from three wells. (One-way ANOVA: $F(3, 8) = 64.08$, $p < 0.001$. Post hoc Dunnett test: LPS vs LPS 1 μM TAK: $p < 0.001$; LPS vs LPS 3 μM TAK: $p < 0.001$; LPS vs LPS 3 μM TAK with no pre-incubation: $p = 0.16$).

Pre-incubation for 4-5 hours with the inhibitor caused a significant decrease in LPS-induced TNFα production (**Figure 44**). Increasing the concentration to 3 μM but not including a pre-incubation step did not reduce the inflammatory response, suggesting that the pre-incubation step is critical for these experiments.

TLR4 inhibitors are commonly used for short experiments, usually around 24 hours. However, the soluble aggregates require at least 96 hours before seeing a response. For this reason, a longer LPS experiment was carried out to determine whether TAK242 can block the inflammatory response in longer experiments.

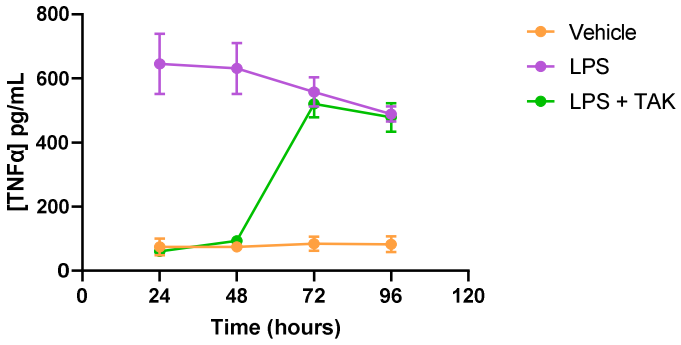

Figure 45: TAK242 long-term inhibition

BV2 cells treated with LPS for 96 hr. Supernatant was collected every 24 hr, cells were washed with PBS, and pre-incubated with 1 μM TAK242 for 5 hr prior to LPS treatment. LPS concentration was 10 ng/mL. Error bars represent mean ± SD from three wells.

TAK242 inhibition was only able to block TNFα production for the first 48 hours (**Figure 45**), suggesting that TAK242 is better suited to shorter experiments. For this reason, TAK242 was not used for future soluble aggregate experiments.

As the TAK242 was not effective at reducing TNFα levels in long-term experiments, a different method for testing TLR4-mediation was explored. TLR4 knockout immortalised bone-marrow derived macrophages (iBMMs) and wildtype iBMMs, obtained from Prof. Clare Bryant's group at the Department of Veterinary Medicine, were treated with soluble aggregates.

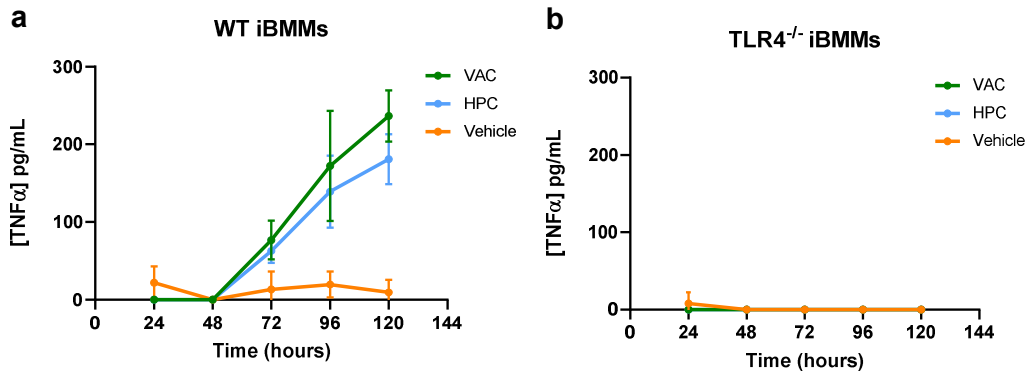

Figure 46: TLR4-mediation

WT = wildtype, *iBMMs* = immortalised bone marrow-derived macrophages, *TLR4*$^{-/-}$ = TLR4 knockout, *VAC* = visual association cortex, *HPC* = hippocampus

TNFα response from (**a**) wildtype and (**b**) TLR4$^{-/-}$ iBMMs treated with 1:5 dilution HPC and VAC soluble aggregates. The samples used were from patient AD3. The vehicle control was aCSF at 1:5 dilution. Error bars are mean ± SD from three wells.

Wildtype iBMMs treated with VAC or HPC samples elicited a significant TNFα response, whereas the TLR4 knockout cells did not (**Figure 46a**), suggesting that this response is mediated by the TLR4 receptor.

4.7. Aβ-containing fragments are likely driving the inflammatory response

The solutions extracted from brain tissue are heterogenous mixtures of proteins. Aβ has been previously shown to be the major toxic species.[178] For this reason, Aβ-containing fragments, as well as Aβ42 specifically, were attempted to be quantified.

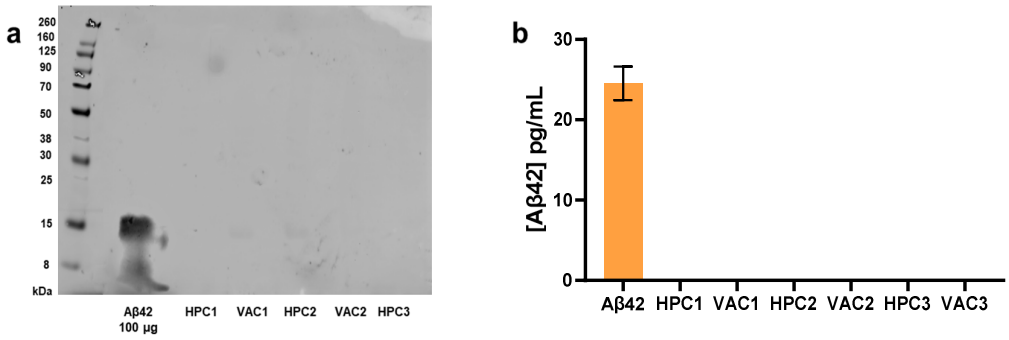

Figure 47: Measuring concentration of Aβ in soluble aggregate samples

(**a**) Western blot using 6E10 primary antibody and Licor Donkey anti-Mouse 800 secondary to detect APP fragments in soluble aggregate samples. 100 µg Abcam synthetic Aβ42 was used as a positive control. (**b**) Aβ42 ELISA used to measure concentration of Aβ42 in the soluble aggregate samples. Abcam synthetic Aβ42 was used as a positive control.

Unfortunately, the levels of Aβ-containing fragments in the soluble aggregate samples were too low to detect using western blot (**Figure 47a**). Due to a dilution error, the synthetic Aβ42 used as a positive control was around 5x greater than the working concentration, resulting in a smear on the gel. This was not repeated due to sample limitations. Aβ42 concentration was also undetectable by ELISA (**Figure 47b**), suggesting that the concentration of Aβ42 in these samples is lower than the sensitivity of the ELISA, most likely in the low picomolar range.

One method for testing whether Aβ-containing aggregates were responsible for the inflammatory response, was to immunodeplete them from the soluble aggregate samples. Before this experiment, the widely used antibodies 6E10 (binds to Aβ-containing fragments, amino acid residue 1-16) and 4G8 (binds to Aβ amino acid residues 17-24) were tested for their efficiency of binding to synthetic Aβ42. Isotype control antibodies were used to rule-out non-specific binding.

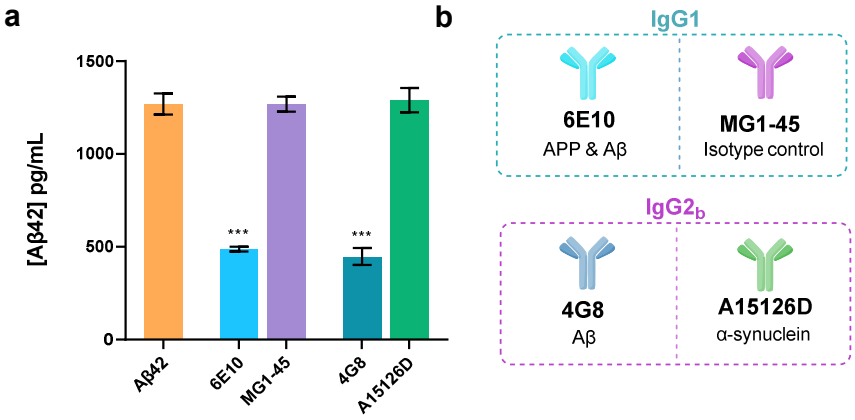

Figure 48: Immunoprecipitation of synthetic Aβ42

(**a**) Immunoprecipitation of monomeric synthetic Aβ42 (Abcam) by 6E10 and 4G8 antibodies. Concentration of each antibody was 20 µg/mL. Aβ42 was measured by a human Aβ42 ELISA. Error bars represent the mean ± SD of three technical repeats. (Unpaired two-tailed t-test, 6E10 vs MG1-45: $n = 3$, $t_4 = 31.56$, $p < 0.001$; 4G8 vs A15126D: $n = 3$, $t_4 = 18.26$, $p < 0.001$).

Both 6E10 and 4G8 antibodies significantly pulled down Aβ42 monomer, to a similar degree. Both antibodies are widely used in literature for similar purposes, however 6E10 was ultimately chosen as 4G8 has been shown to also react with the conformational epitope of non-Aβ aggregated fibrils (including α-synuclein).[241] HPC and VAC samples from the three patients were immunoprecipitated with 6E10, and BV2 cells were then treated with soluble aggregates with and without immunoprecipitation.

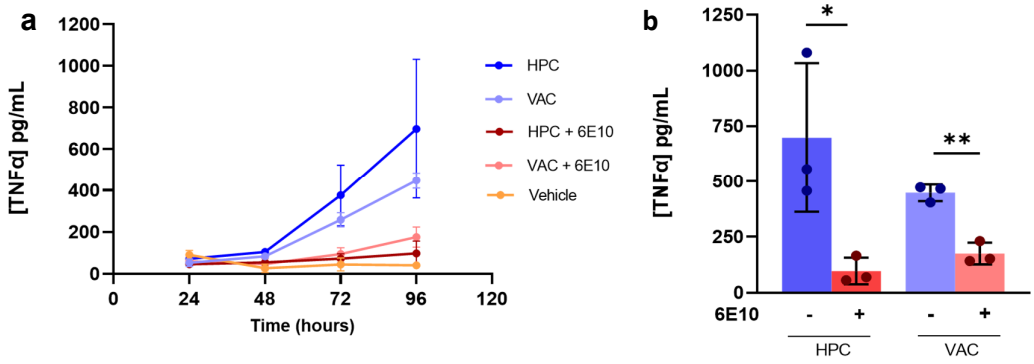

Figure 49: Immunodepletion of Aβ-containing fragments

(**a**) TNFα response measured from BV2 cells treated with 1:5 diluted soluble aggregate samples that have either undergone (red) or not undergone (blue) immunoprecipitation using a 6E10 antibody. Each point represents an average from three patients. Vehicle control was aCSF at equal volume to soluble aggregate samples. LPS at 10 ng/mL was used as positive control (not shown). Error bars are mean ± SD. (**b**) TNFα measured at the 96-hr time point. Each point represents one of three Alzheimer's disease patients. Error bars are mean ± SD. (Unpaired two-tailed t-test, HPC vs HPC + 6E10: n = 3, p = 0.04, t_4 = 3.061; VAC vs VAC + 6E10: n = 3, p = 0.002, t_4 =7.658).

Samples immunodepleted of Aβ-containing fragments using the 6E10 antibody caused a significantly lower inflammatory response than samples that did not undergo immunodepletion for both HPC and VAC (**Figure 49b**). This data is consistent with Aβ-containing fragments playing a role in the soluble aggregate-mediated inflammatory response. To rule out non-specific binding, this experiment was repeated using an isotype control antibody (MG1-45). Only one sample was used from one patient due to limited availability of samples.

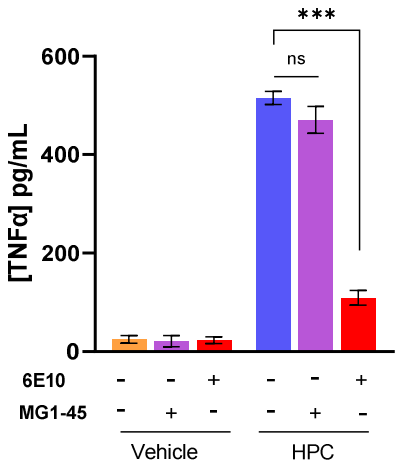

Figure 50: Immunoprecipitation using isotype control antibody

TNFα response at the 96-hr time point, measured from BV2 cells treated with soluble aggregate samples at a 1:5 dilution, that have either undergone a pull-down using a 6E10 antibody (red) or isotype control (purple). Vehicle control was aCSF at equal volume to soluble aggregate samples. LPS at 10 ng/mL was used as positive control (not shown). Error bars are mean ± SD from three wells. (One-Way ANOVA; $F(2, 6) = 385.8$, $p < 0.001$. Post hoc Tukey test: HPC vs HPC 6E10: $n = 3$, $p < 0.001$; HPC MG1-45 vs HPC 6E10: $n = 3$, $p < 0.001$; HPC vs HPC MG1-45: $n = 3$, $p = 0.07$).

The HPC sample that was immunoprecipitated using 6E10 caused a significantly lower TNFα response to the non-immunoprecipitated HPC sample (**Figure 50**). Furthermore, the MG1-45 isotype control antibody did not affect the TNFα response, suggesting that the observed effects are not due to non-specific binding, but most likely due to Aβ-containing fragments in the samples.

4.8. Neurite retraction assay

AD brain-derived Aβ has been shown to disrupt the microtubule cytoskeleton of primary rat hippocampal neurons, causing time-dependent neuritic degeneration.[181] A live-cell imaging assay was optimised to measure the neurite retraction of primary mouse hippocampal neurons, similar to what has been done with human neurons.[242]

4.8.1. Red lentivirus (synapsin promoter)

Primary mouse hippocampal neurons, harvested by Robyn McAdam, were used for the optimisation of this assay. As primary cell preps rarely result in complete single-cultures, it was important to distinguish whether the processes imaged with the IncuCyte® live-cell imaging technology, were neuronal or glial. For this reason, the cells were transduced with Neurolight Red Lentivirus Reagent, a lentiviral-based vector encoded with a red fluorescent protein (mKate2) driven off a synapsin promoter, according to the manufacturer's instructions. They were then imaged using the IncuCyte® at 20x magnification.

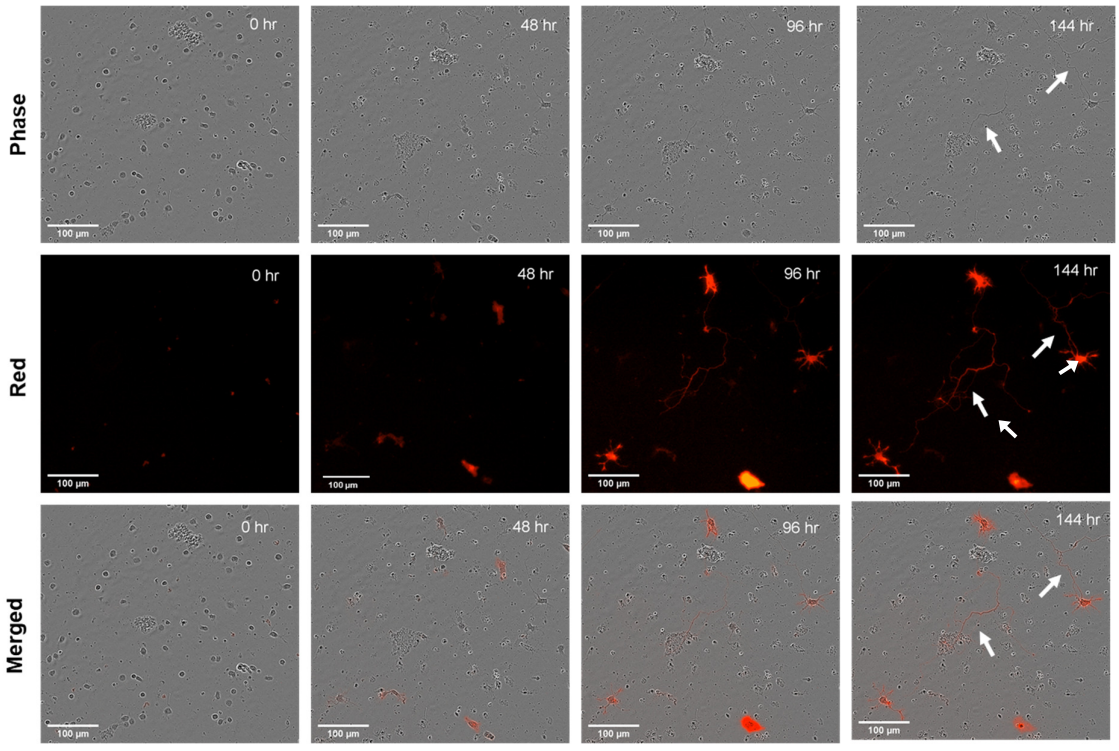

Figure 51: Red lentivirus

Primary mouse hippocampal neurons plated at a density of 10,000 cells/well were lentivirally transduced with IncuCyte® Neurolight Red Lentivirus Reagent for 144 hr. White arrows are highlighting some major neuronal processes.

The cells were plated at a density of 10,000 cells/well, which appeared to be too low as it led to cell death. However, it was possible to assess the lentivirus' ability to pick up neurites on the few viable cells. The red channel picked up most of the major and minor neuronal processes, similar to what was seen using phase-contrast. It took about 2 days after transduction for the red fluorescence to become visible. It should be noted however that the red fluorescence was quite weak and was not easily detected using the built-in NeuroTrack software. The red channel images in **Figure 51** have had background subtraction and contrast enhancement through ImageJ in order to make the neurites more visible for the reader. The lentivirus reagent was not noticeably better at picking up neuronal projections than phase-contrast, so phase-contrast alone was used going forward for neurite length experiments.

4.8.2. Cell density optimisation

To determine the optimal cell density for this assay, a range of cell densities were plated and imaged for 72 hours. Three wells were used for each condition.

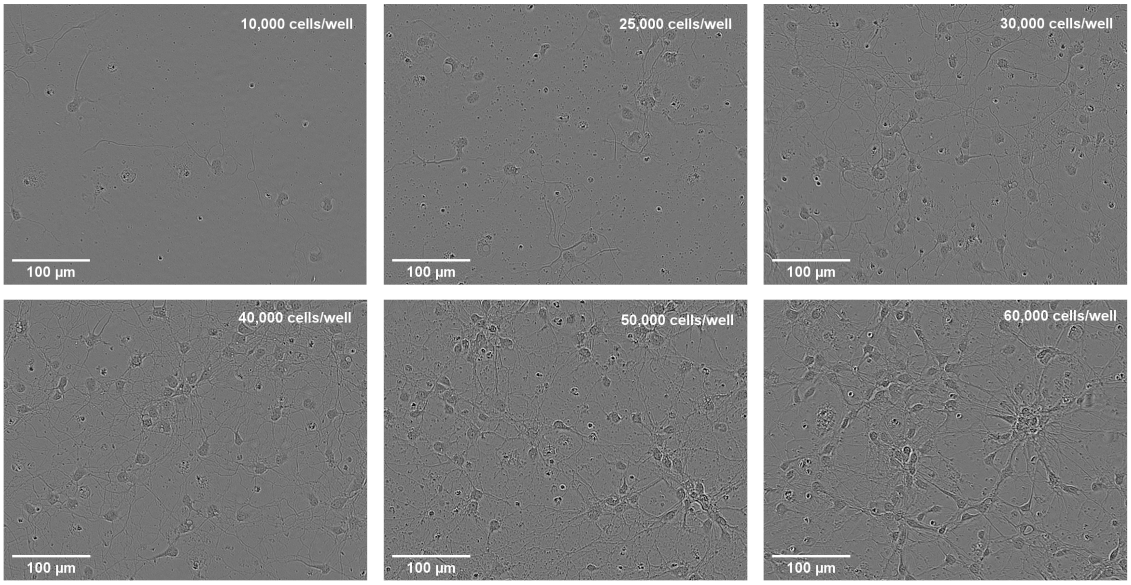

Figure 52: Neurite retraction cell density optimisation

Representative IncuCyte® (phase) images of 3 DIV primary mouse hippocampal neurons at densities ranging from 10,000 – 60,000 cells/well.

In the lower cell densities (10,000 and 25,000 cells/well), the cells were very scarce and did not have many projections between them. In the higher cell densities (40,000 - 60,000 cells/well) the cells began clumping, making it difficult to accurately detect neurites with the NeuroTrack software. For these reasons, future experiments used a density of 30,000 cells/well, which had an even distribution of cells in the well with enough cells for healthy neurite growth but not too many to cause cell clumping.

4.8.3. Soluble aggregates cause neurite retraction in primary mouse neurons

With the imaging protocol and cell density optimised, the assay was carried out using HPC soluble aggregates. The neurite length was measured after 80 hours using the NeuroTrack software.

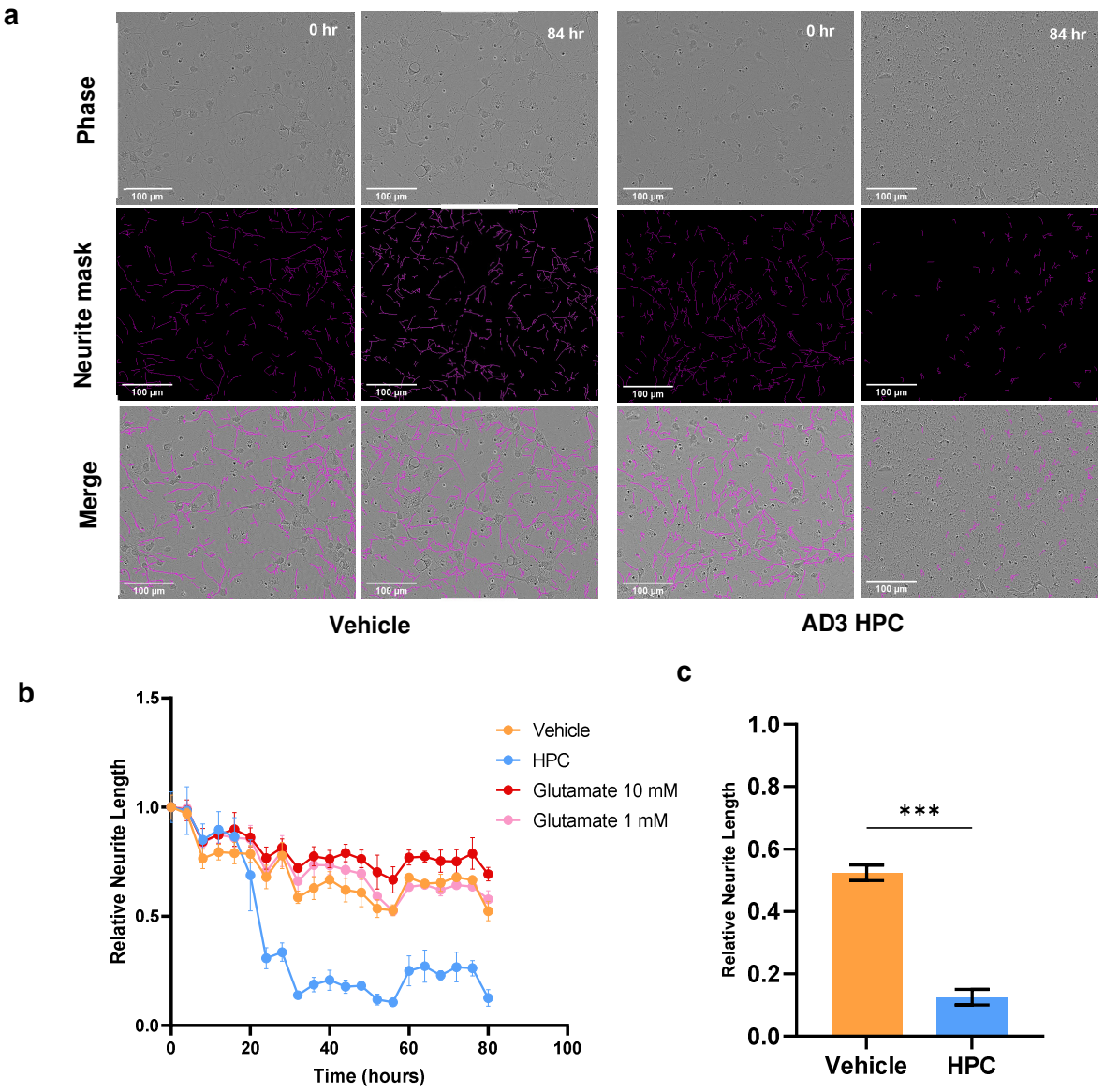

Figure 53: Neurite retraction assay

(**a**) Representative images of primary mouse hippocampal neurons treated with vehicle control or HPC aggregates (from patient AD3) for 80 hr. Vehicle control was aCSF at equal volume to soluble aggregate samples. (**b**) Relative neurite length, normalised to neurite length at the 0-hr time point. Error bars are mean ± SD from three wells. (**c**) The 80-hr time point. Error bars are mean ± SD from three wells. (Unpaired t-test: Vehicle vs HPC: n = 3, $t_4 = 19.57$, $p < 0.001$).

Treatment of primary mouse hippocampal cells with HPC soluble aggregates caused significant neurite retraction over 80 hours (**Figure 53c**). This suggested that the soluble aggregates were neurotoxic, similar to what has been previously reported with Braak stage VI soluble aggregates.[178] However, the glutamate which was added as a positive control for neuron-specific degeneration, did not cause significant reduction in neurite length. This is most likely due to the cells being treated at 4 DIV (days *in vitro*), which might be too early for maturation and synaptogenesis. Mouse hippocampal neurons have been reported to have maximal levels of expressed synaptic markers at 10 DIV.[243] Similarly, rat hippocampal neurons have increased synaptophysin levels and mean synaptic firing rate between 7 DIV and 14 DIV.[244] Experiments with primary mouse hippocampal neurons could not be repeated due to COVID-19 limited access.

4.8.4. Validation of neurite length assay with a human cell line

This response was also validated in a human cell line, Lund human mesencephalic (LUHMES) cells. These are human embryonic neuronal precursor cells that undergo proliferation due to the expression of a tetracycline-regulatable (Tet-off) v-*myc* transgene and can be differentiated into mature dopaminergic neurons with the addition of tetracycline.

4.8.5. Optimisation of neurite length assay with LUHMES neurons

A preliminary experiment was carried out with 10,000 cells/well.

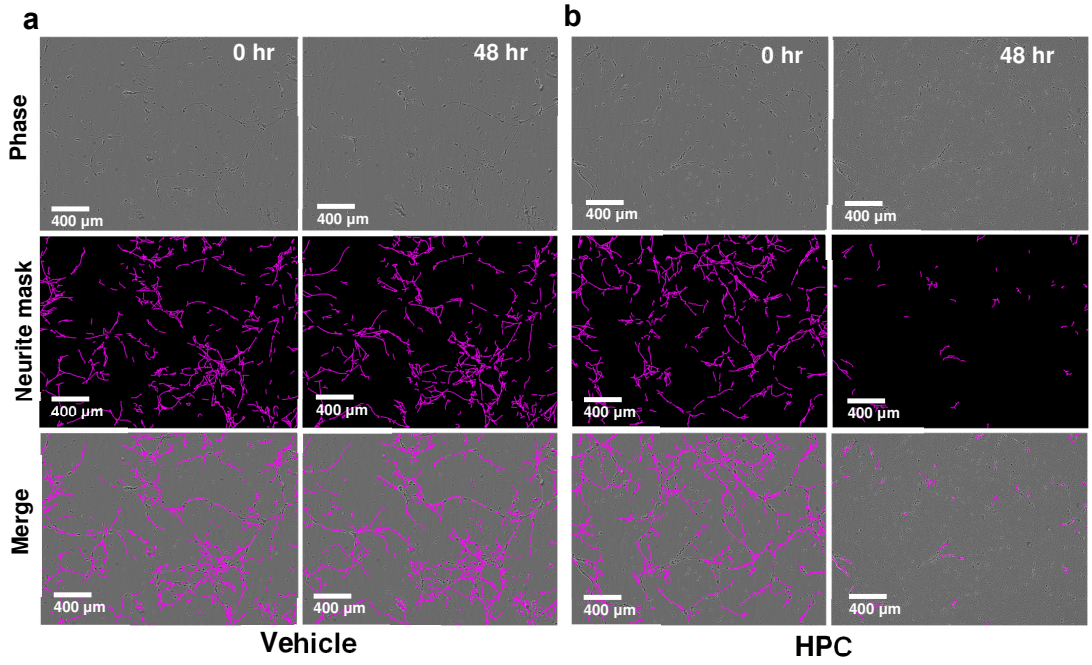

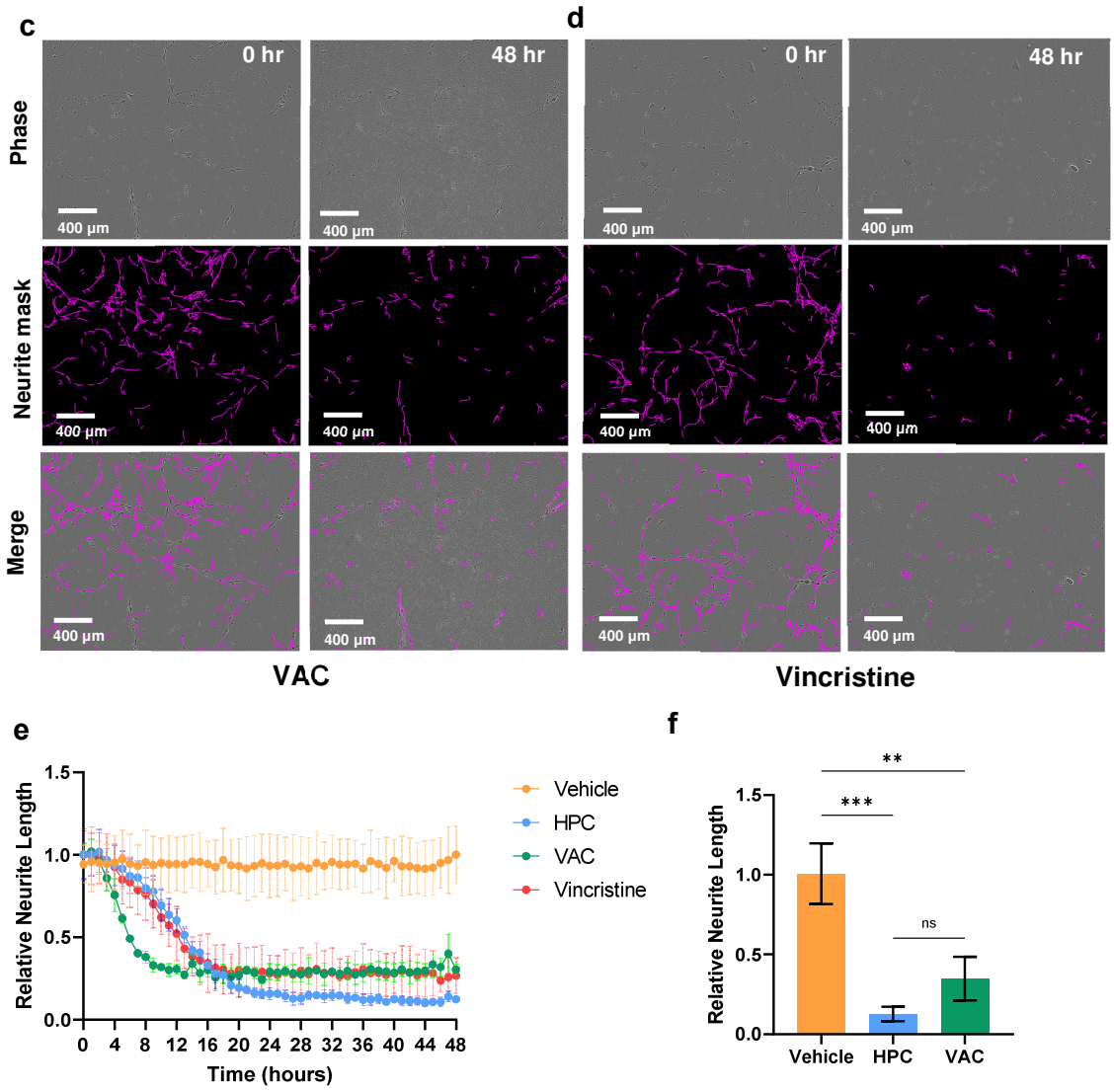

Figure 54: Neurite length assay optimisation with LUHMES neurons

Representative images of the neurite length of LUHMES neurons (6,000 cells/well) treated with (**a**) vehicle control, (**b**) HPC from AD1, (**c**) VAC from AD1 or (**d**) vincristine at 0 and 48-hr time points. (**e**) Relative neurite length of LUHMES neurons at 10,000 cells/well, treated with vehicle, soluble aggregates, or vincristine. Normalised to neurite length at the 0-hr time point. Vehicle was aCSF at same dilution as soluble aggregate samples, and vincristine (50 nM) served as a positive control for neurite retraction. Error bars are mean ± SD from three wells. (**f**) Statistical analysis of the 48-hr time point. Error bars are mean ± SD from three wells. (One-way ANOVA: $F(2, 6) = 33.05$, $p < 0.001$. Post hoc Tukey test: $n = 3$ for all: Vehicle vs HPC: $p < 0.001$; Vehicle vs VAC: $p = 0.003$; HPC vs VAC: $p = 0.2$).

This preliminary experiment showed that 48 hours was sufficient for soluble aggregate-mediated neurite retraction. Furthermore, the cell density of 10,000 cells/well was enough to get a good spread throughout the well, without overcrowding.

4.8.6. Soluble aggregates cause neurite retraction in LUHMES neurons

The LUHMES neurons were treated with HPC and VAC soluble aggregates from all patients for 48 hours.

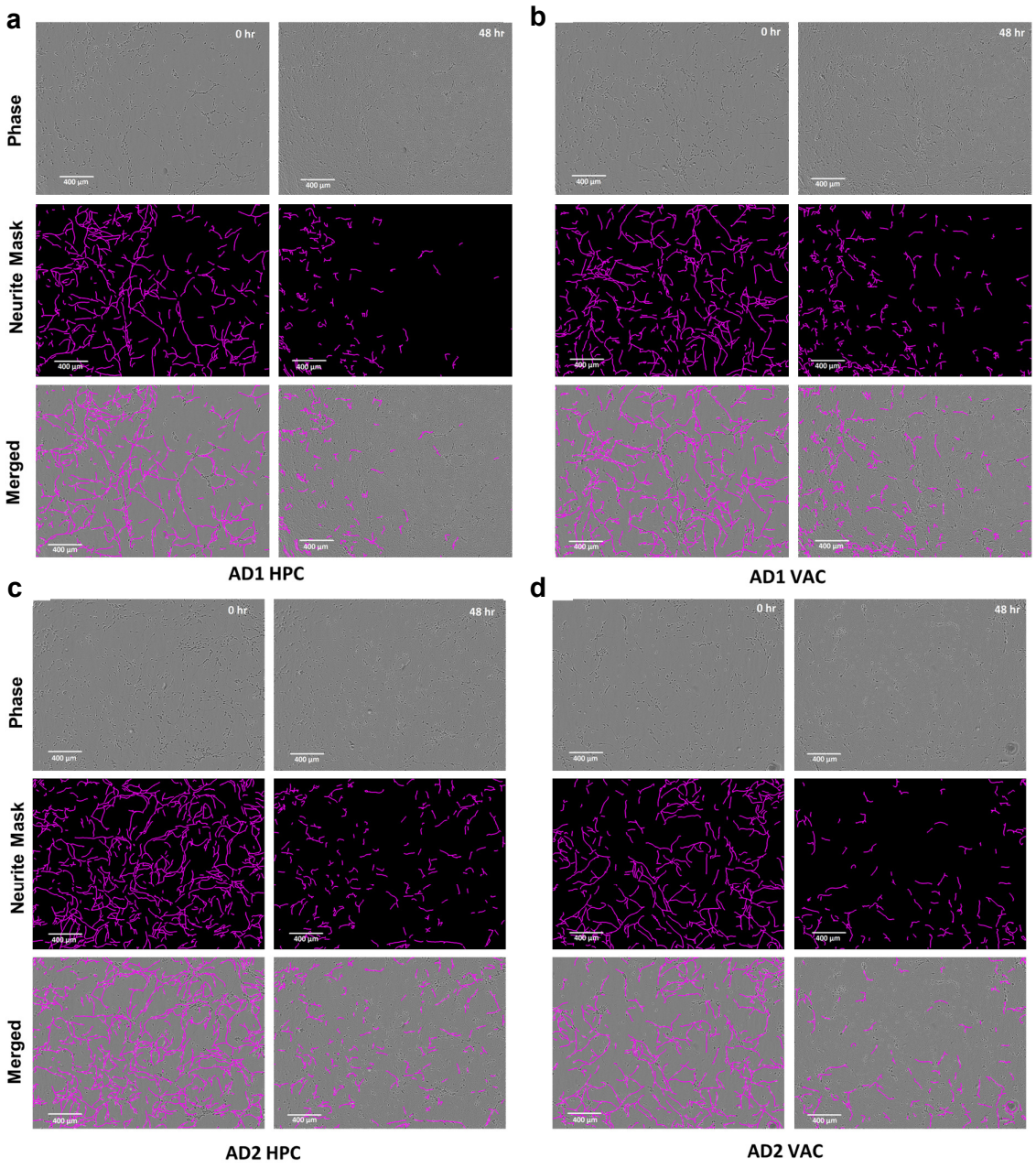

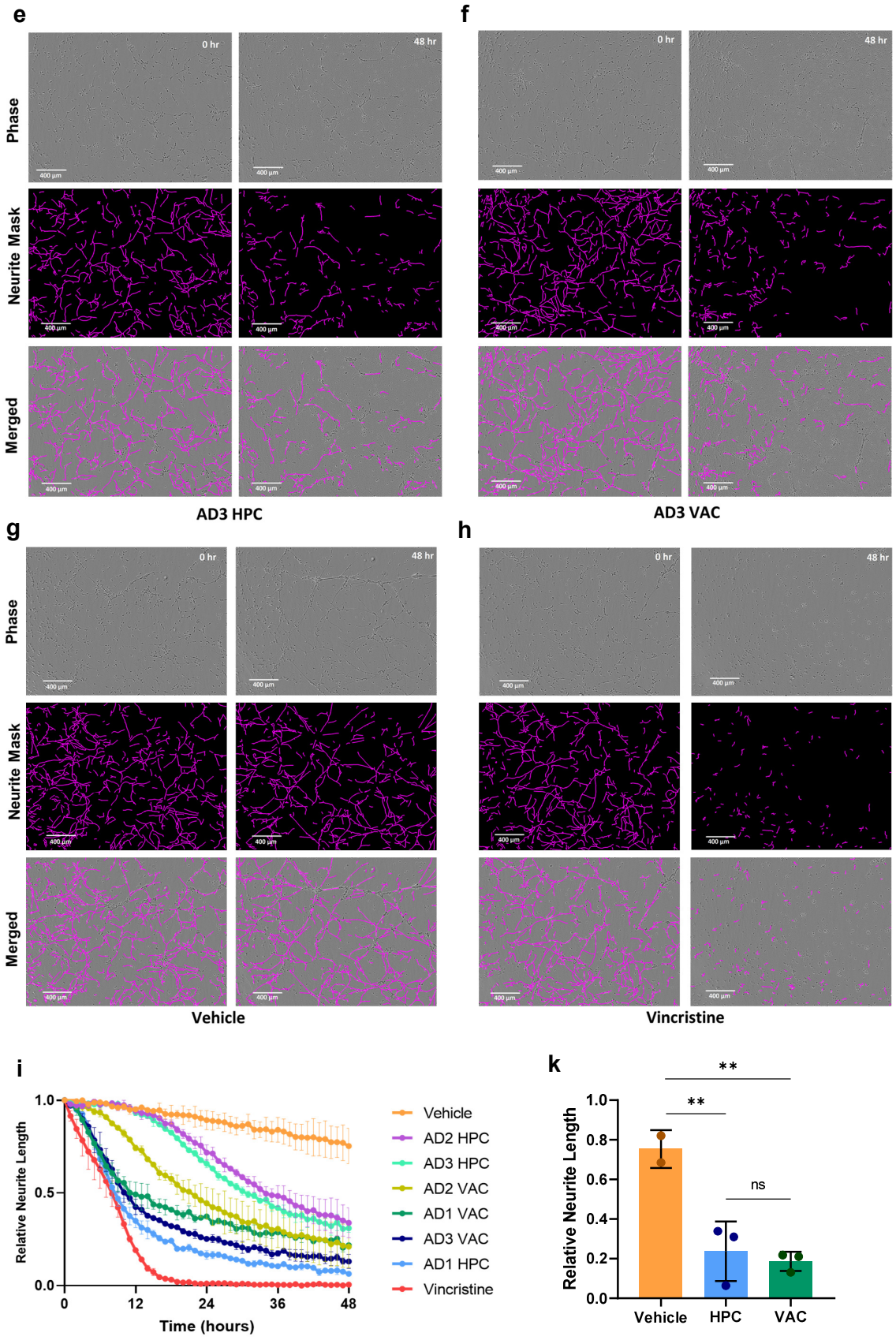
e
f
Phase
Neurite Mask
Merged
0 hr
48 hr
400 µm
AD3 HPC
AD3 VAC
g
h
Vehicle
Vincristine
i
Relative Neurite Length
1.0
0.5
0.0
0
12
24
36
48
Time (hours)
Vehicle
AD2 HPC
AD3 HPC
AD2 VAC
AD1 VAC
AD3 VAC
AD1 HPC
Vincristine
k
**
**
ns
Relative Neurite Length
1.0
0.8
0.6
0.4
0.2
0.0
Vehicle
HPC
VAC

Figure 55: Soluble aggregates cause neurite retraction in LUHMES neurons

Representative images of neurite length of LUHMES cells treated with (**a**) AD1 HPC, (**b**) AD1 VAC, (**c**) AD2 HPC, (**d**) AD2 VAC, (**e**) AD3 HPC, (**f**) AD3 VAC, (**g**) vehicle or (**h**) vincristine, at 0 and 48 hr of treatment. (**i**) Relative neurite length of LUHMES cells (~7,200 cells imaged per condition) treated with soluble aggregate samples at a 1:5 dilution for 48 hr, normalised to neurite length at the 0-hr time point (1.0), and vincristine at 48 hr (0) to signify total neurite retraction. Vehicle was aCSF at same dilution as soluble aggregate samples (1:5), and vincristine (50 nM) served as a positive control for neurite retraction. Error bars are mean ± SD from two biological repeats, with each condition carried out in triplicate wells, and 4 images analysed per well. (**k**) Relative neurite length at the 48-hr time point averaged by brain region. Each point represents one of three Alzheimer's disease patients. Error bars are mean ± SD. (One-way ANOVA: $F(2, 5) = 18.63$, $p = 0.005$. Post hoc Tukey test: n = 3 for all: Vehicle vs HPC: $p = 0.008$; Vehicle vs VAC: $p = 0.005$; HPC vs VAC: $p = 0.84$).

Treatment of LUHMES cells with HPC and VAC soluble aggregates caused significant neurite retraction over 48 hours (**Figure 55**). This suggests that the soluble aggregates are neurotoxic, similar to what has been previously reported with Braak stage VI soluble aggregates.[178] Surprisingly, there was no significant difference between the level of HPC and VAC aggregate-induced neurite retraction (**Figure 55k**).

To determine whether this neurotoxicity is mediated through the TLR4 receptor, LUHMES neurons were pre-incubated with 1 μM TAK242 for 5 hours (as optimised previously, see **Figure 44**) prior to being treated with HPC and VAC from all patients.

4.8.7. Neurite retraction is not mediated through TLR4

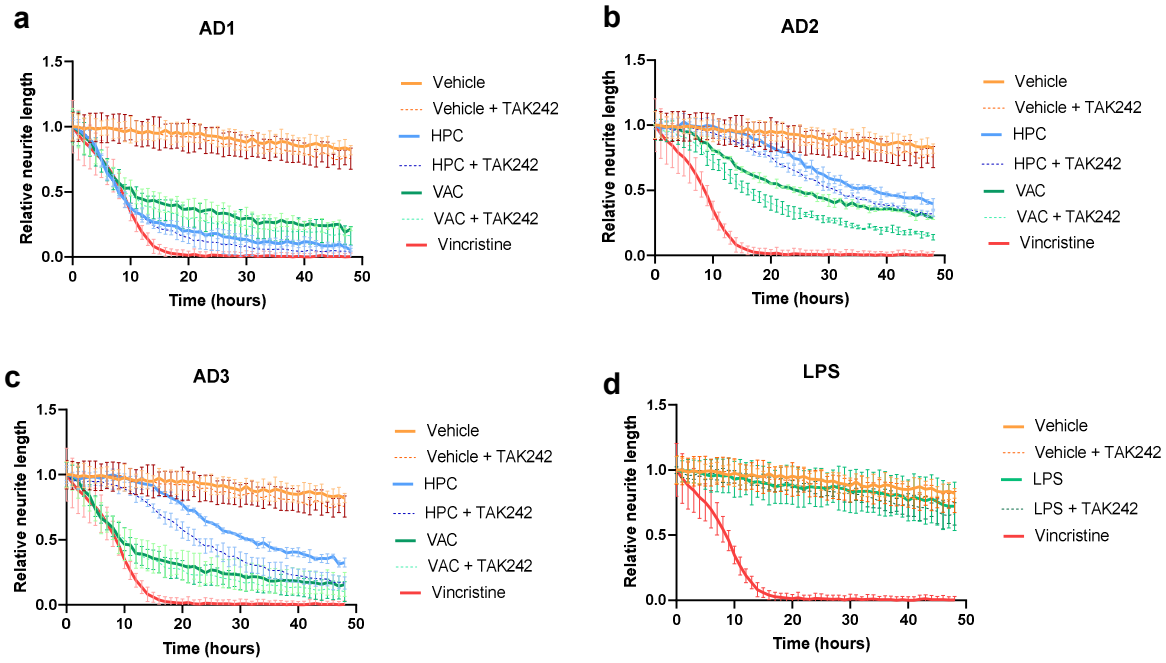

Figure 56: Neurite length with TLR4 inhibitor

Relative neurite length for LUHMES neurons treated with soluble aggregates from patient (**a**) AD1, (**b**) AD2 and (**c**) AD3, with and without 5-hr pre-incubation with 1 μM TAK242. (**d**) Relative neurite length for LUHMES neurons treated with LPS and TAK242. Error bars are mean ± SD from three wells.

Pre-incubation with the TLR4 inhibitor TAK242 did not rescue soluble aggregate-mediated neurite retraction (**Figure 57a-c**). This is not surprising, seeing as treatment with LPS also did not affect neurite length (**Figure 57d**). Neurite retraction therefore does not appear to be mediated through TLR4, suggesting a different mechanism of toxicity. One suggested mechanism is that the Aβ aggregates are acting on the mitochondria, leading to caspase 3 activation and neurite retraction.[245,246]

The soluble aggregates were then characterised further using the super-resolution microscopy technique, Aptamer-DNA PAINT (AD PAINT).

4.9. Length and number characterisation of soluble aggregates

AD PAINT imaging and analysis was done by Dr. John Danial and Dr. Jason C. Sang. ***Figure 57*** *was created by me from their data.*

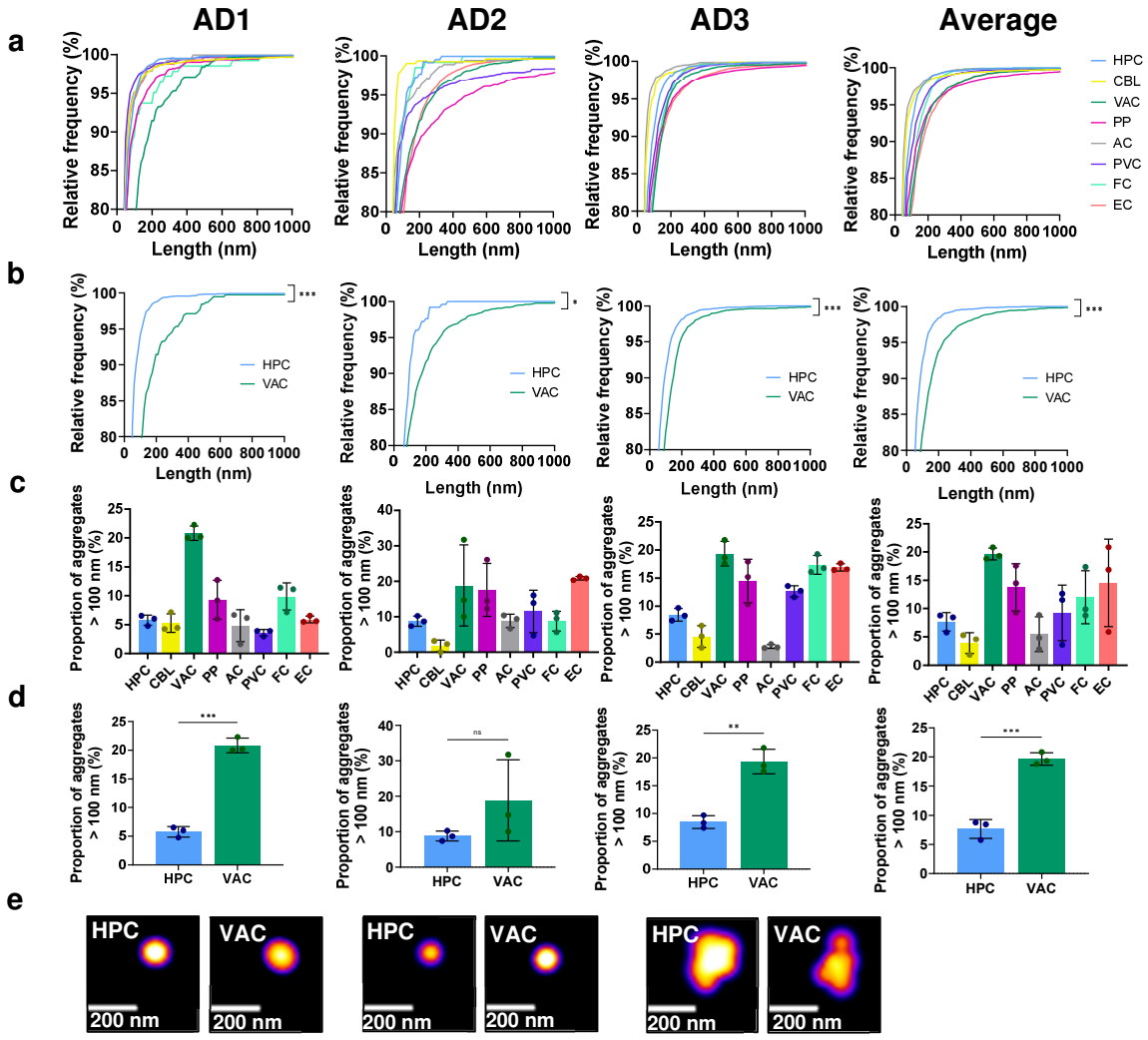

Figure 57: AD PAINT characterisation of soluble aggregates

(**a**) Cumulative frequency of soluble aggregates in all eight brain regions and in (**b**) HPC and VAC regions only, from three independent experiments. (Kolmogorov-Smirnov test, AD1: $p < 0.001$, $D = 0.2092$; AD2: $p = 0.03$, $D = 0.0974$; AD3: $p < 0.001$, $D = 0.3799$; Average: $p < 0.001$, $D = 0.2016$). See Table 7 for the results of multiple comparison test. (**c**) Proportion of soluble aggregates over 100 nm in length in all eight brain regions and in (**d**) HPC and VAC regions only. Each point in the AD1, AD2, and AD3 graphs represents one of three replicates; each point in the Average graph represents one of three Alzheimer's disease patients. Error bars are mean ± SD. (Unpaired two-tailed t-test, n = 3 for all. AD1: $p < 0.001$, $t_4 = 16.71$; AD2: $p = 0.21$, $t_4 = 1.510$; AD3: $p = 0.002$, $t_4 = 7.618$; Average: $p < 0.001$, $t_4 = 10.66$). (**e**) Representative super-resolved images of aggregates in HPC and VAC samples.

Table 7: Results from multiple comparisons test for AD PAINT data

Patient	HPC > VAC	HPC < VAC	Not Significant	No. of tests (#HPC x #VAC)
AD1	0	9	0	9 (3 x 3)
AD2	0	3	6	9 (3 x 3)
AD3	0	9	0	9 (3 x 3)
Average	0	9	0	9 (3 x 3)

HPC > VAC and HPC < VAC refer to cases where the soluble aggregates in the HPC samples were larger or smaller than the VAC aggregates respectively, according to the Kolmogorov-Smirnov test (significance level = 0.01).

The length and number of the soluble aggregates have been characterised by AD PAINT super-resolution microscopy. This was performed using an aptamer-docking strand that binds to fibrillar Aβ, although it can also bind fibrillary α-synuclein fibrils. The complementary imaging strand is then added in buffer and binds transiently to the docking strand creating bright spots that can be measured. The aggregates seemed to vary from region to region, and from patient to patient. In all cases there was a variety of soluble aggregates of a range of lengths detected, however the length distributions differed (**Figure 57a,c**). The HPC aggregates appeared to be shorter than VAC aggregates in general, and had a smaller proportion of longer aggregates (over 100 nm) (**Figure 57b,d**). Despite the clear difference in length there was a relatively small difference between the inflammatory responses of these two regions (**Figure 38d,e**), suggesting that the aggregates smaller than 100 nm (80-95% of all aggregates) are most inflammatory.

The soluble aggregates were then characterised further using atomic force microscopy (AFM) imaging.

4.10. Structural characterisation of aggregates using AFM

AFM imaging and analysis was done entirely by Dr. Francesco Simone Ruggeri.

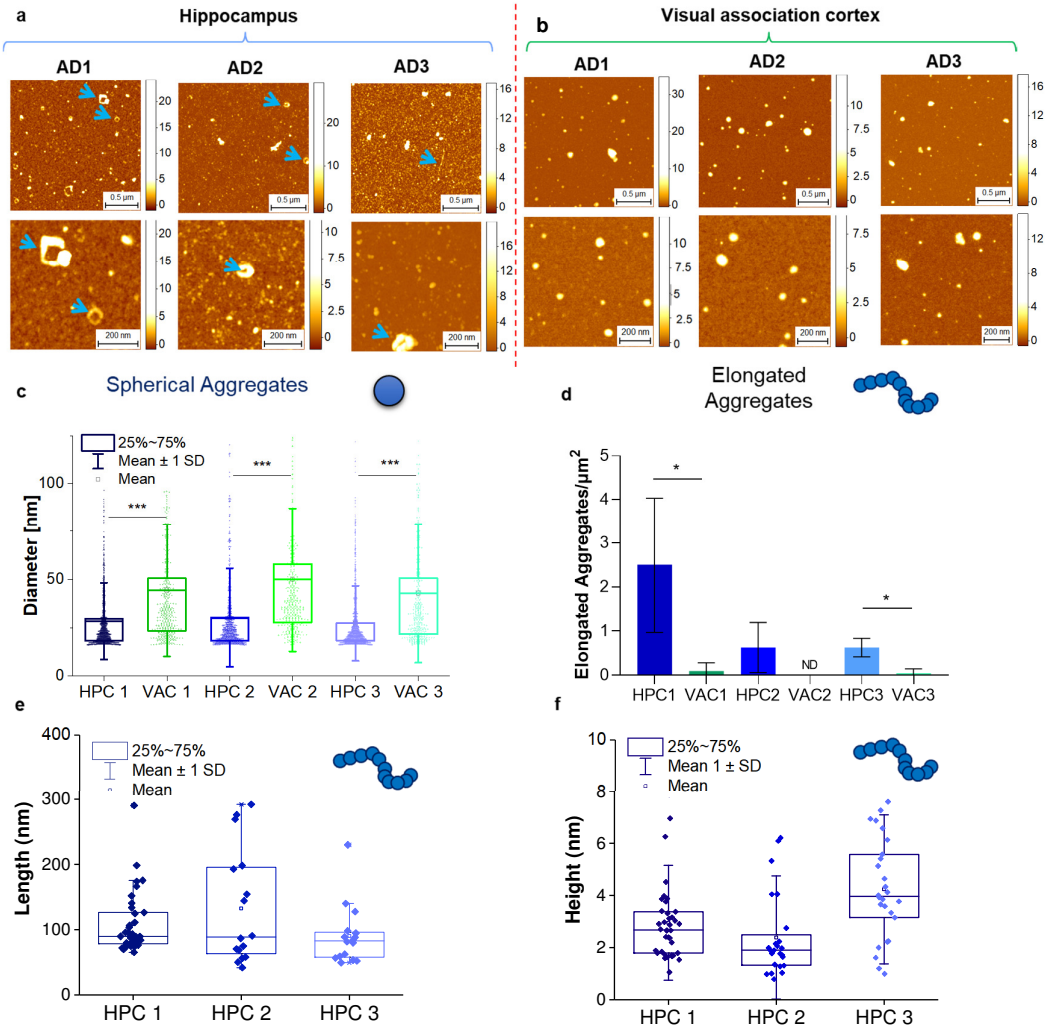

Figure 58: High-resolution AFM imaging of aggregates 3-D morphology

Structural characterisation of the aggregates in (**a**) HPC and (**b**) VAC regions using AFM. The blue arrows are highlighting toroidal and elongated aggregates. (**c**) The single aggregate statistical analysis of the cross-sectional diameter of the spherical aggregates reveals that VAC spherical aggregates are significantly larger than HPC ones (Mann-Whitney test, two-tailed; HPC1 vs VAC1: $p < 0.001$, $U = 140761$; HPC2 vs VAC2: $p < 0.001$, $U = 56141$; HPC3 vs VAC3: $p < 0.001$, $U = 125376$). (**d**) Bar plot with SD of the density of the number of elongated protofilaments and toroidal oligomers for µm² in each sample. The graph shows the significant presence of elongated aggregates in the HPC (n1=35, n2=17, n3=16 per 20 µm2) compared to the VAC samples (n1=2, n2=0, n3=1 per 20 µm2) (Unpaired two-tailed t-test, HPC1 vs VAC1: $p = 0.03$, $t_{35} = 2.195$; HPC3 vs VAC3: $p = 0.02$, $t_{15} = 2.706$). (**e**) Statistical analysis of the cross-sectional length and (**f**) cross-sectional height of the toroidal, prefibrillar and fibrillar aggregates.

The 3-D morphology and the heterogeneity of the aggregates from the HPC and VAC samples were characterised using high-resolution and phase controlled AFM imaging (**Figure 58a-b**).[203,247,248] In both the HPC and the VAC samples, there was an abundant presence of spherical aggregates. The single molecule statistical analysis of the cross-sectional diameter of these aggregates showed that the spherical aggregates present in the HPC samples had a diameter (~30-50 nm) that was significantly smaller than the diameter of the spherical aggregates in the VAC samples (~50-80 nm) (**Figure 58c**). The difference of the average diameter of the aggregates is in agreement with the results obtained by AD-PAINT in **Figure 57**.

Furthermore, the HPC samples contained several elongated toroidal structures, as well as fibrillar and prefibrillar aggregates. The VAC samples contained a significantly smaller number of elongated aggregates, and toroidal aggregates were not found in the 500 μm^2 area of the sample that was imaged in a randomised manner. The statistically significant difference in the number of elongated aggregates in the HPC vs VAC samples was evaluated by calculating the density of the number of these elongated aggregates per μm^2 (**Figure 58d**). The toroidal and fibrillar aggregates had an average length of ~100 nm (**Figure 58e**).

AFM cannot determine the proteins the toroidal, fibrillar, and spherical structures consist of. However, the different heterogeneity of the aggregated species in the HPC and VAC samples suggests that there is a regional variability in the structures of soluble aggregates, and toroidal and fibrillar structures might be more toxic than spherical structures.

4.11. Characterisation of Aβ-containing fragments through SiMPull

SiMPull imaging and analysis was done by Derya Emin, Yu P. Zhang, and Dr Evgenia Lobanova.

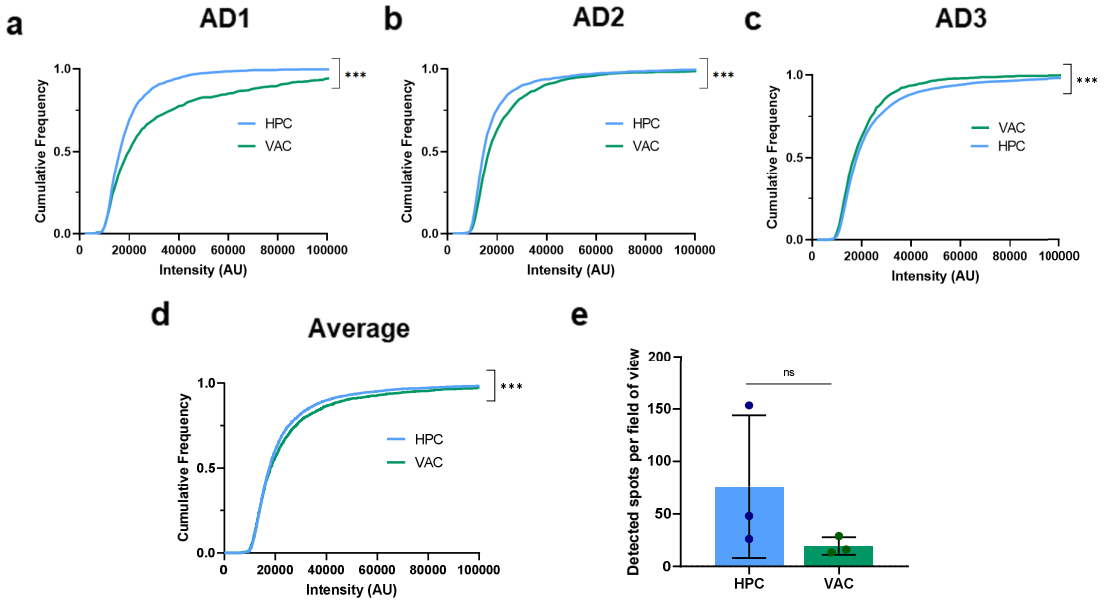

Figure 59: SiMPull characterisation of Aβ-containing aggregates

Cumulative frequency plots of intensity values of Aβ-containing aggregates in HPC and VAC samples from (**a**) AD1 (Kolmogorov-Smirnov test, HPC vs VAC, $p < 0.001$, $D = 0.1987$), (**b**) AD2 (Kolmogorov-Smirnov test, HPC vs VAC, $p < 0.001$, $D = 0.1451$), (**c**) AD3 (Kolmogorov-Smirnov test, HPC vs VAC, $p < 0.001$, $D = 0.0804$) and (**d**) Average of the three patients (Kolmogorov-Smirnov test, HPC vs VAC, $p < 0.001$, $D = 0.05452$). (**e**) The number of detected spots (Aβ) per field of view (380 x 380 pixel cropped images). Each point represents one of three Alzheimer's disease patients. Error bars are mean ± SD. (Unpaired two-tailed t-test, HPC vs VAC, $n = 3$, $p = 0.47$, $t_4 = 0.7978$).

Table 8:Results from multiple comparisons test for SiMPull data

Patient	HPC > VAC	HPC < VAC	Not Significant	No. of tests (#HPC x #VAC)
AD1	1	1	2	4 (2 x 2)
AD2	1	2	1	4 (2 x 2)
AD3	3	1	0	4 (2 x 2)
Average	2	7	0	9 (3 x 3)

HPC > VAC and HPC < VAC refer to cases where the soluble aggregates in the HPC samples were larger or smaller than the VAC aggregates respectively, according to the Kolmogorov-Smirnov test (significance level = 0.01).

AD-PAINT and AFM imaging allowed for the characterisation of the morphology, size, number, and shape of the soluble aggregates. However, as the techniques are not protein-specific, the single-molecule pull-down technique was employed to specifically characterise the Aβ-containing aggregates in these samples.[249] Intensity values provide an approximation of aggregate molecular weight, assuming that more fluorescent antibodies bind larger aggregates, and hence an increase in intensity correlates with an increase in aggregate size. The intensity values suggested that VAC samples contained larger Aβ-containing aggregates than the HPC samples in two out of the three patients (**Figure 59a-c**), and when averaging the three patients (**Figure 59d**). This is in agreement with the AD-PAINT and AFM data, which also showed that VAC samples had larger aggregates than HPC samples. There was no significant difference in the number of detectable spots per field of view for the two regions (**Figure 59e**).

4.12. Conclusions and future work

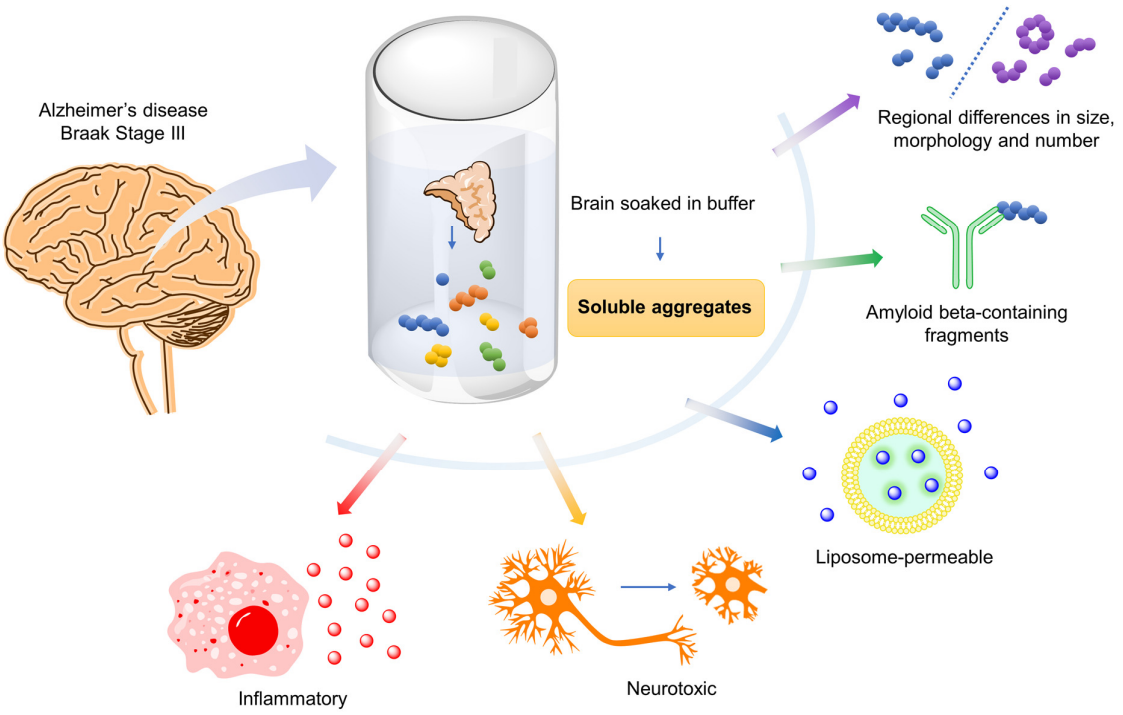

Figure 60: Summary of Chapter 4 major findings

In this chapter, a method for extracting soluble aggregates by soaking AD brain tissue in buffer has been optimised. These soluble aggregates have been found to be inflammatory (most likely driven by Aβ-containing aggregates), neurotoxic, liposome-permeable, and have been shown to have regional differences in size, morphology and number.

The only previous study using soluble aggregates extracted from soaking brain tissue analysed Braak stage VI AD brains and showed that the major species was Aβ that caused LTP deficit and neuronal retraction.[178] In this pilot study we wanted to first see whether we could detect any aggregates in early disease samples, since this would allow us to study earlier events in disease development. We characterised the soluble aggregates from eight different brain regions from three Alzheimer's disease patients at Braak stage III. Soluble aggregates from all eight regions were neuroinflammatory and liposome-permeable, to varying degrees. This suggests that there is global pathology occurring even at Braak stage III. We found extensive variation between the same regions in different brains, for example in the aggregate length and number, but clear differences between HPC and VAC, since the former is affected very early in Alzheimer's disease and the latter is largely unaffected until late disease. We therefore

chose to compare the soluble aggregates in HPC and VAC regions using all assays, with VAC serving as an internal control for each patient.

Despite patient-to-patient variability, HPC aggregates appeared to be the most toxic (**Figure 38,38**). TNFα secretion in response to soluble Aβ aggregates has been previously reported to cause long-term potentiation deficit,[218] a cellular correlate of memory loss, so together with our data showing inflammation being highest in the hippocampus, this offers an explanation as to why memory loss occurs in AD.

Neurite retraction induced by soluble aggregates occurred within 24-48 hours (**Figure 55i**), whereas the microglial TNFα response to the same concentration of soluble aggregates arose after 72-96 hours (**Figure 38a-d**). This might suggest that neurons are more sensitive to soluble aggregates than microglia, although this could simply be a result of different cell densities used for the experiments. Furthermore, this might not be the case in the actual disease condition where neurons are in constant crosstalk with glial cells, which may have neuroprotective or neurotoxic properties. It would be interesting in future experiments to try adding the supernatant from microglia treated with soluble aggregates, which should be full of proinflammatory cytokines and chemokines, to neurons, and in that way measure the direct effect of aggregate-induced neuroinflammation on neurotoxicity, as has been done previously.[250–252] It would also be interesting to grow a co-culture of neurons and glial cells and treat them with soluble aggregates. The use of AD patient-derived iPSCs would also increase the clinical relevance of these experiments.

We have identified the size, length, morphology and number of these endogenous soluble aggregates. These varied from region to region and from patient to patient but importantly there was a range of aggregates of different sizes (20-200 nm) in all regions. It should be noted that the aptamer used for the AD-PAINT studies can bind both Aβ and α-synuclein, however our work[167,186] and previous work[178] suggests that it is most likely Aβ. Furthermore, AFM imaging is not protein specific, but the sizes of the imaged aggregates are consistent with those measured with AD-PAINT, similar to what was observed in our previous work on CSF.[186]

We have taken advantage of the high-resolution of AFM to further characterise the morphology and structure of soluble aggregates from the hippocampus and the visual association cortex. HPC samples contained structures of toroidal nature, as well as

fibrillar structures. VAC samples rarely had fibrillar structures and contained many spherical structures. We have found in CSF[186] and with synthetic aggregates[167] that protofibrils are the main inflammatory species. This is likely because they are the right diameter to be bound by multiple toll-like receptor 4s (TLR4s). Indeed, in the HPC samples about 7-15% of the aggregates detected by AFM have the right height (~2 nm) to produce a strong inflammatory response, compared to the proportion in the VAC, which is less than 2%**.** These aggregates were less than 100 nm in length, which is also consistent with our observation, combining our AD-PAINT and inflammatory assay results, that the inflammatory aggregates are less than 100 nm in length. Overall, our data suggests that fibrillary aggregates less than 100 nm in length and 2 nm in diameter can cause inflammation and that there are more of these aggregates in the HPC compared to the VAC.

A previous study has found that activated microglia are present in HPC and VAC in Alzheimer's disease patients classed as having low neuropathologic change.[53] Both the HPC and VAC already had some activated microglia. It was found that there are more microglia and more activated microglia in HPC than VAC, but an increase in the proportion of activated microglia occurred in both areas at early stages. This is supported by cross-sectional studies, which have used PET scans to detect activated microglia, and have shown increases in inflammation in early disease all over the brain that is associated with cognitive decline.[253–255] Peripheral cytokine studies have shown that this increase in inflammation in early disease plateaus in later stages of the disease.[256–259] In combination with our work, this suggests that instead of aggregates spreading through the brain, the same aggregate-induced inflammation is occurring locally to a greater or lesser extent in the entire brain simultaneously.

In AD, Aβ has been reported to spread from neocortical areas to the brainstem and cerebellum, and tau spreading from the temporal lobe, which includes the entorhinal cortex and hippocampus, to limbic and association areas.[16,260] Several mechanisms for this spreading have been proposed, including the "transneuronal spread model" where toxic aggregates spread along neuronal connections in a prion-like manner,[261] and local spreading where aggregates spread to physically adjacent regions, via release into the extracellular space and then taken up by nearby neurons or glial cells.[262–264] Another possibility is that the toxic proteins are not spreading themselves; instead neuroinflammation is spreading from region to region, inducing the

aggregation of toxic proteins in each region, as supported by the presence of neuroinflammatory soluble aggregates in all eight regions (**Figure 38**). Microglial activation has been reported to correlate with the spread of tau pathology, further supported by reports suggesting microglia might induce tau hyperphosphorylation as well as take-up and release of tau seeds that couldn't be broken down, into the extracellular space.[265,266] This suggests that microglia might play an important role in the spread of tau pathology, however this might not be the case for soluble Aβ. Recent studies have shown that microglia do not appear to take up and transport soluble Aβ, but instead degrade them by secreting insulin-degrading enzyme (IDE).[267] If the spread of toxic proteins is mediated partly by neuroinflammation, the challenge remains to understand why neuroinflammation spreads differently in different neurodegenerative diseases, such as AD and Parkinson's disease. It is possible that the extent of inflammation and where it starts might determine how different neurodegenerative diseases form and spread. For example, traumatic brain injury is a major insult with high inflammation and rapid spreading, while AD may have low long-term levels of inflammation that spread more slowly. To get a stronger understanding of the mechanisms of spreading and the differences between neurodegenerative diseases, future work could look into other toxic aggregates, such as tau, α-synuclein, and TDP-43, as well as brain tissue from patients with other neurodegenerative disorders. Spreading most likely occurs from a combination of mechanisms occurring simultaneously, with neuroinflammation and toxic proteins spreading together and inducing each other in a positive feed-back loop manner.

It should be noted that our study was intended to determine the feasibility of this approach and has been performed on a small number of Alzheimer's disease patients due to the manual nature of these experiments. The Klenerman group is currently working on automating these assays to allow for more high-throughput assessment of Alzheimer's disease brain tissue, to explore whether similar characteristics of soluble aggregates are found in larger cohorts and allow comparison to age matched control brain and brain at later stages of AD. More sensitive neuroinflammation assays are also needed to better characterise the inflammatory properties of aggregates from different brain regions. Examples of this include the TNFα imaging experiments described in Chapter 3, complemented with either flow cytometry or Incucyte live-cell imaging, which could be optimised for brain-derived soluble aggregates. A

combination of automated high-throughput and highly sensitive assays would have the potential to characterise the aggregates that form in humans during the development of AD and identify which aggregates are toxic and by what mechanisms. By studying regions where inflammatory aggregates are just starting to be formed, it may be possible to study the early processes of disease. In the future, AD brains from other Braak stages should be analysed, to gain a stronger understanding of the relationship between soluble Aβ aggregates and disease progression.

Overall, our data is consistent with small soluble Aβ-containing aggregates, 2 nm in diameter and less than 100 nm in length, driving inflammation in Alzheimer's disease to greater or lesser extents in all regions of the brain and this aggregate-induced inflammation then causing cellular dysfunction and ultimately cell death. Our study also highlights the heterogeneity in size, morphology and structure of the aggregates formed in the brain with the proportion of different aggregates differing between brain regions. It also highlights the challenges in selectively targeting the correct species and suggests that targeting the aggregate induced inflammation may be a better therapeutic strategy than attempting to target specific aggregates.

References

1. Alzheimer's Association. 2017 Alzheimer's disease facts and figures. *Alzheimers Dement* **13**, 325–373 (2017).

2. Frisoni, G. B. *et al.* Detection of grey matter loss in mild Alzheimer's disease with voxel based morphometry. *J. Neurol. Neurosurg. Psychiatry* **73**, 657–664 (2002).

3. Thompson, P. M. *et al.* Mapping hippocampal and ventricular change in Alzheimer disease. *Neuroimage* **22**, 1754–1766 (2004).

4. Prince, M. *et al. Dementia UK update*. *Alzheimer's Society* (2014).

5. John, S. *Deaths registered in England and Wales: 2018*. *Office for National Statistics* (2019).

6. Reitz, C. & Mayeux, R. Alzheimer disease: Epidemiology, diagnostic criteria, risk factors and biomarkers. *Biochem. Pharmacol.* **88**, 640–651 (2014).

7. Saunders, A. M. *et al.* Association of apolipoprotein E allele epsilon 4 with late-onset familial and sporadic Alzheimer's disease. *Neurology* **43**, 1467–72 (1993).

8. Tanzi, R. E. *et al.* Assessment of amyloid beta-protein precursor gene mutations in a large set of familial and sporadic Alzheimer disease cases. *Am. J. Hum. Genet.* **51**, 273–82 (1992).

9. Wolfe, C. M., Fitz, N. F., Nam, K. N., Lefterov, I. & Koldamova, R. The role of APOE and TREM2 in Alzheimer′s disease—Current understanding and perspectives. *Int. J. Mol. Sci.* **20**, 65–70 (2018).

10. Tai, L. M. *et al.* APOE-modulated Aβ-induced neuroinflammation in Alzheimer's disease: Current landscape, novel data, and future perspective. *J. Neurochem.* **133**, 465–488 (2015).

11. Guerreiro, R., Brás, J. & Hardy, J. SnapShot: Genetics of Alzheimer's disease. *Cell* **155**, 968-968.e1 (2013).

12. Guerreiro, R. & Hardy, J. Genetics of Alzheimer's Disease. *Neurotherapeutics* **11**, 732–737 (2014).

13. Kunkle, B. W. *et al.* Genetic meta-analysis of diagnosed Alzheimer's disease identifies new risk loci and implicates Aβ, tau, immunity and lipid processing. *Nat. Genet.* **51**, 414–430 (2019).

14. Alzheimer, A. Über eine eigenartige Erkrankung der Hirnrinde. *Cent. fur Nervenheilkd. Psychiatr.* **30**, 177–179 (1907).

15. Citron, M. Alzheimer's disease: Strategies for disease modification. *Nat. Rev. Drug Discov.* **9**, 387–398 (2010).

16. Braak, H. & Braak, E. Neuropathological stageing of Alzheimer-related changes. *Acta Neuropathol.* **82**, 239–259 (1991).

17. Thal, D. R., Rüb, U., Orantes, M. & Braak, H. Phases of Aβ-deposition in the human brain and its relevance for the development of AD. *Neurology* **58**, 1791–1800 (2002).

18. Goedert, M. Alzheimer's and Parkinson's diseases: The prion concept in relation to assembled Aβ, tau, and α-synuclein. *Science* **349**, 61–69 (2015).

19. Thal, D. R., Griffin, W. S. T. & Braak, H. Parenchymal and vascular Aβ-deposition and its effects on the degeneration of neurons and cognition in Alzheimer's disease. *J. Cell. Mol. Med.* **12**, 1848–1862 (2008).

20. Bloom, G. S. Amyloid-β and tau: The trigger and bullet in Alzheimer disease pathogenesis. *JAMA Neurol.* **71**, 505–508 (2014).

21. Wray, S. & Noble, W. Linking amyloid and tau pathology in Alzheimer's disease: The role of membrane cholesterol in Aβ-mediated tau toxicity. *J. Neurosci.* **29**, 9665–9667 (2009).

22. Leroy, K. *et al.* Lack of tau proteins rescues neuronal cell death and decreases amyloidogenic processing of APP in APP/PS1 mice. *Am. J. Pathol.* **181**, 1928–1940 (2012).

23. Chiti, F. & Dobson, C. M. Protein misfolding, amyloid formation, and human disease: A summary of progress over the last decade. *Annu. Rev. Biochem.* **86**, 27–68 (2017).

24. Hartmann, T. *et al.* Distinct sites of intracellular production for Alzheimer's disease Aβ40/42 amyloid peptides. *Nat. Med.* **3**, 1016–1020 (1997).

25. Thinakaran, G. & Koo, E. H. Amyloid precursor protein trafficking, processing, and function. *J. Biol. Chem.* **283**, 29615–29619 (2008).

26. Rice, H. C. *et al.* Secreted amyloid-β precursor protein functions as a GABABR1A ligand to modulate synaptic transmission. *Science* **363**, 1–7 (2019).

27. Takami, M. *et al.* γ-Secretase: Successive tripeptide and tetrapeptide release from the transmembrane domain of β-carboxyl terminal fragment. *J. Neurosci.* **29**, 13042–13052 (2009).

28. Steiner, H., Fukumori, A., Tagami, S. & Okochi, M. Making the final cut: Pathogenic amyloid-β peptide generation by γ-secretase. *Cell Stress* **2**, 292–310 (2018).

29. Chow, V. W., Mattson, M. P., Wong, P. C. & Gleichmann, M. An overview of APP processing enzymes and products. *Neuromolecular Med.* **12**, 1–12 (2010).

30. Knowles, T. P. J., Vendruscolo, M. & Dobson, C. M. The amyloid state and its association with protein misfolding diseases. *Nat. Rev. Mol. Cell Biol.* **15**, 384–396 (2014).

31. Wilson, M. R., Yerbury, J. J. & Poon, S. Potential roles of abundant extracellular chaperones in the control of amyloid formation and toxicity. *Mol. BioSyst.* **4**, 42–52 (2008).

32. Arosio, P., Knowles, T. P. J. & Linse, S. On the lag phase in amyloid fibril formation. *Phys. Chem. Chem. Phys.* **17**, 7606–7618 (2015).

33. Cohen, S. I. A. *et al.* Proliferation of amyloid-β42 aggregates occurs through a secondary nucleation mechanism. *Proc. Natl. Acad. Sci.* **110**, 9758–9763 (2013).

34. Xue, W. F. *et al.* Fibril fragmentation enhances amyloid cytotoxicity. *J. Biol. Chem.* **284**, 34272–34282 (2009).

35. Barykin, E. P., Mitkevich, V. A., Kozin, S. A. & Makarov, A. A. Amyloid β modification: A key to the sporadic Alzheimer's disease? *Front. Genet.* **8**, 1–5 (2017).

36. Shankar, G. M. *et al.* Amyloid-β protein dimers isolated directly from Alzheimer's brains impair synaptic plasticity and memory. *Nat. Med.* **14**, 837–842 (2008).

37. Walsh, D. M. *et al.* Naturally secreted oligomers of amyloid β protein potently inhibit hippocampal long-term potentiation in vivo. *Nature* **416**, 535–539 (2002).

38. Haass, C. & Selkoe, D. J. Soluble protein oligomers in neurodegeneration: lessons from the Alzheimer's amyloid β-peptide. *Nat. Rev. Mol. Cell Biol.* **8**, 101–112 (2007).

39. Glabe, C. G. Structural classification of toxic amyloid oligomers. *J. Biol. Chem.* **283**, 29639–29643 (2008).

40. Cummings, J. L. Alzheimer's Disease. *N. Engl. J. Med.* **351**, 56–67 (2004).

41. Blennow, K., de Leon, M. J. & Zetterberg, H. Alzheimer's disease. *Lancet* **368**, 387–403 (2006).

42. Selkoe, D. J. Amyloid β-protein and the genetics of Alzheimer's disease. *J. Biol. Chem.* **271**, 18295–18298 (1996).

43. Selkoe, D. J. & Hardy, J. The amyloid hypothesis of Alzheimer's disease at 25 years. *EMBO Mol. Med.* **8**, 595–608 (2016).

44. Bronzuoli, M. R., Iacomino, A., Steardo, L. & Scuderi, C. Targeting neuroinflammation in Alzheimer's disease. *J. Inflamm. Res.* **9**, 199–208 (2016).

45. Rivest, S. Regulation of innate immune responses in the brain. *Nat. Rev. Immunol.* **9**, 429–439 (2009).

46. Mandrekar, S. & Landreth, G. E. Microglia and Inflammation in Alzheimers Disease. *CNS Neurol. Disord. - Drug Targets* **9**, 156–167 (2010).

47. Verkhratsky, A., Rodríguez, J. J. & Steardo, L. Astrogliopathology. *Neurosci.* **20**, 576–588 (2014).

48. Liu, Y.-P., Lin, H.-I. & Tzeng, S.-F. Tumor necrosis factor-alpha and interleukin-18 modulate neuronal cell fate in embryonic neural progenitor culture. *Brain Res.* **1054**, 152–158 (2005).

49. Terrando, N. *et al.* Resolving postoperative neuroinflammation and cognitive decline. *Annu. Neurol.* **70**, 986–995 (2011).

50. Czapski, G. A. *et al.* The mechanisms regulating cyclin-dependent kinase 5 in hippocampus during systemic inflammatory response: The effect on inflammatory gene expression. *Neurochem. Int.* **93**, 103–112 (2016).

51. Kinney, J. W. *et al.* Inflammation as a central mechanism in Alzheimer's disease. *Alzheimer's Dement. Transl. Res. Clin. Interv.* **4**, 575–590 (2018).

52. Sudduth, T. L., Schmitt, F. A., Nelson, P. T. & Wilcock, D. M. Neuroinflammatory phenotype in early Alzheimer's disease. *Neurobiol. Aging* **34**, 1051–1059 (2013).

53. Prokop, S. *et al.* Impact of TREM2 risk variants on brain region-specific immune activation and plaque microenvironment in Alzheimer's disease patient brain samples. *Acta Neuropathol.* **138**, 613–630 (2019).

54. Wyss-Coray, T. *et al.* TGF-β1 promotes microglial amyloid-β clearance and reduces plaque burden in transgenic mice. *Nat. Med.* **7**, 612–618 (2001).

55. Brosseron, F., Krauthausen, M., Kummer, M. & Heneka, M. T. Body Fluid Cytokine Levels in Mild Cognitive Impairment and Alzheimer's Disease: a Comparative Overview. *Mol. Neurobiol.* **50**, 534–544 (2014).

56. Frederiksen, H. R., Haukedal, H. & Freude, K. Cell type specific expression of toll-like receptors in human brains and implications in Alzheimer's disease. *Biomed Res. Int.* **2019**, 1–18 (2019).

57. Hollingworth, P. *et al.* Common variants in ABCA7, MS4A6A/MS4A4E, EPHA1, CD33 and CD2AP are associated with Alzheimer's disease. *Nat. Genet.* **43**, 429–435 (2011).

58. Liddelow, S. A. *et al.* Neurotoxic reactive astrocytes are induced by activated microglia. *Nature* **541**, 481–487 (2017).

59. Morgan, B. P. & Morgan, B. P. Complement in the pathogenesis of Alzheimer ' s disease. *Semin. Immunopathol.* **40**, 113–124 (2018).

60. Campioni, S. *et al.* A causative link between the structure of aberrant protein oligomers and their toxicity. *Nat. Chem. Biol.* **6**, 140–147 (2010).

61. Fusco, G. *et al.* Structural basis of membrane disruption and cellular toxicity by a-synuclein oligomers. *Science* **358**, 1440–1443 (2017).

62. Chakrabarty, P. *et al.* TLR5 decoy receptor as a novel anti-amyloid therapeutic for Alzheimer's disease. *J. Exp. Med.* **215**, 2247–2264 (2018).

63. Heneka, M. T. *et al.* Neuroinflammation in Alzheimer's disease. *Lancet Neurol.* **14**, 388–405 (2015).

64. Jarosz-Griffiths, H. H., Noble, E., Rushworth, J. V. & Hooper, N. M. Amyloid-β receptors: The good, the bad, and the prion protein. *J. Biol. Chem.* **291**, 3174–3183 (2016).

65. Mroczko, B., Groblewska, M., Litman-Zawadzka, A., Kornhuber, J. & Lewczuk, P. Cellular receptors of amyloid β oligomers (AβOs) in Alzheimer's disease. *Int. J. Mol. Sci.* **19**, 1–29 (2018).

66. Laurén, J., Gimbel, D. A., Nygaard, H. B., Gilbert, J. W. & Strittmatter, S. M. Cellular prion protein mediates impairment of synaptic plasticity by amyloid-β oligomers. *Nature* **457**, 1128–1132 (2009).

67. Wang, H.-Y. *et al.* β-Amyloid 1–42 Binds to α7 Nicotinic Acetylcholine Receptor with High Affinity . *J. Biol. Chem.* **275**, 5626–5632 (2000).

68. Snyder, E. M. *et al.* Regulation of NMDA receptor trafficking by amyloid-β. *Nat. Neurosci.* **8**, 1051–1058 (2005).

69. Hsieh, H. *et al.* AMPAR Removal Underlies Aβ-Induced Synaptic Depression and Dendritic Spine Loss. *Neuron* **52**, 831–843 (2006).

70. Um, J. W. *et al.* Metabotropic glutamate receptor 5 is a co-receptor for Alzheimer Aβ oligomer bound to cellular prion protein. *Neuron* **79**, 887–902 (2008).

71. Zhao, Y. *et al.* TREM2 is a receptor for β-amyloid which mediates microglial function. *Neuron* **97**, 1023–1031 (2018).

72. Ma, J., Yee, A., Brewer, H., Das, S. & Potter, H. The amyloid-associated proteins alpha1-antichymotypsin and apolipoprotein E promote the assembly of the Alzheimer ß protein into filaments. *Nature* **372**, 92–94 (1994).

73. Liu, S. *et al.* TLR2 Is a Primary Receptor for Alzheimer's Amyloid β Peptide To Trigger Neuroinflammatory Activation. *J. Immunol.* **188**, 1098–1107 (2012).

74. Walter, S. *et al.* Role of the toll-like receptor 4 in neuroinflammation in Alzheimer's disease. *Cell. Physiol. Biochem.* **20**, 947–956 (2007).

75. Chowdhury, P., Sacks, S. H. & Sheerin, N. S. Toll-like receptors TLR2 and TLR4 initiate the innate immune response of the renal tubular epithelium to bacterial products. *Clin. Exp. Immunol.* **145**, 346–356 (2006).

76. Bsibsi, M., Ravid, R., Gveric, D. & Van Noort, J. M. Broad expression of Toll-like receptors in the human central nervous system. *J. Neuropathol. Exp. Neurol.* **61**, 1013–1021 (2002).

77. Zhou, Y. *et al.* Activation of toll-like receptors inhibits herpes simplex virus-1 infection of human neuronal cells. *J. Neurosci. Res.* **87**, 2916–2925 (2009).

78. Zughaier, S. M., Zimmer, S. M., Datta, A., Carlson, R. W. & Stephens, D. S. Differential induction of the toll-like receptor 4-MyD88-dependent and -independent signaling pathways by endotoxins. *Infect. Immun.* **73**, 2940–2950 (2005).

79. Shurety, W., Pagan, J. K., Prins, J. B. & Stow, J. L. Endocytosis of uncleaved tumor necrosis factor-α in macrophages. *Lab. Investig.* **81**, 107–117 (2001).

80. Sedger, L. M. & McDermott, M. F. TNF and TNF-receptors: From mediators of cell death and inflammation to therapeutic giants - past, present and future. *Cytokine Growth Factor Rev.* **25**, 453–472 (2014).

81. Tartaglia, L. A., Ayres, T. M., Wong, G. H. W. & Goeddel, D. V. A novel domain within the 55 kd TNF receptor signals cell death. *Cell* **74**, 845–853 (1993).

82. Chang, R., Yee, K.-L. & Sumbria, R. K. Tumor necrosis factor α Inhibition for Alzheimer's Disease. *J. Cent. Nerv. Syst. Dis.* **9**, 117957351770927 (2017).

83. Rothe, M., Pan, M. G., Henzel, W. J., Ayres, T. M. & V. Goeddel, D. The TNFR2-TRAF signaling complex contains two novel proteins related to baculoviral inhibitor of apoptosis proteins. *Cell* **83**, 1243–1252 (1995).

84. Rao, P., Hsu, K. C. & Chao, M. V. Upregulation of NF-κB-dependent gene expression mediated by the p75 tumor necrosis factor receptor. *J. Interf. Cytokine Res.* **15**, 171–177 (1995).

85. Fontaine, V. *et al.* Neurodegenerative and neuroprotective effects of tumor necrosis factor (TNF) in retinal ischemia: opposite roles of TNF receptor 1 and TNF receptor 2. *J. Neurosci.* **22**, 1–7 (2002).

86. McCoy, M. K. & Tansey, M. G. TNF signaling inhibition in the CNS: Implications for normal brain function and neurodegenerative disease. *J. Neuroinflammation* **5**, 1–13 (2008).

87. Megumi, K., Stellwagen, D., Malenka, R. C. & Stryker, M. P. Tumor Necrosis Factor-α mediates one component of competitive, experience-dependent plasticity in developing visual cortex. *Neuron* **58**, 673–680 (2008).

88. Santello, M., Bezzi, P. & Volterra, A. TNFα controls glutamatergic gliotransmission in the hippocampal dentate gyrus. *Neuron* **69**, 988–1001 (2011).

89. Yamamoto, M. *et al.* Interferon-γ and tumor necrosis factor-α regulate amyloid-β plaque deposition and β-secretase expression in Swedish mutant APP transgenic mice. *Am. J. Pathol.* **170**, 680–692 (2007).

90. Liaoi, Y. F., Wang, B. J., Cheng, H. T., Kuo, L. H. & Wolfe, M. S. Tumor necrosis factor-α, interleukin-1β, and interferon-γ stimulate γ-secretase-mediated cleavage of amyloid precursor protein through a JNK-dependent MAPK pathway. *J. Biol. Chem.* **279**, 49523–49532 (2004).

91. Hickman, S. E., Allison, E. K. & El Khoury, J. Microglial dysfunction and defective β-amyloid clearance pathways in aging alzheimer's disease mice. *J. Neurosci.* **28**, 8354–8360 (2008).

92. Janelsins, M. C. *et al.* Chronic neuron-specific tumor necrosis factor-alpha expression enhances the local inflammatory environment ultimately leading to neuronal death in 3xTg-AD mice. *Am. J. Pathol.* **173**, 1768–1782 (2008).

93. McGeer, E. G. & McGeer, P. L. Inflammatory processes in Alzheimer's disease. *Prog. Neuro-Psychopharmacology Biol. Psychiatry* **27**, 741–749 (2003).

94. von Bernhardi, R., Cornejo, F., Parada, G. E. & Eugenín, J. Role of TGFβ signaling in the pathogenesis of Alzheimer's disease. *Front. Cell. Neurosci.* **9**, 1–21 (2015).

95. Chen, C.-H. *et al.* Increased NF-κB signalling up-regulates BACE1 expression and its therapeutic potential in Alzheimer's disease. *Int. J. Neuropsychopharmacol.* **15**, 77–90 (2012).

96. Fillit, H. *et al.* Elevated circulating tumor necrosis factor levels in Alzheimer's disease. *Neurosci. Lett.* **129**, 318–320 (1991).

97. Tarkowski, E., Andreasen, N., Tarkowski, A. & Blennow, K. Intrathecal inflammation precedes development of Alzheimer's disease. *J. Neurol. Neurosurg. Psychiatry* **74**, 1200–1205 (2003).

98. Paganelli, R. *et al.* Proinflammatory cytokines in sera of elderly patients with dementia: Levels in vascular injury are higher than those of mild-moderate Alzheimer's disease patients. *Exp. Gerontol.* **37**, 257–263 (2002).

99. Dickson, D. W. The pathogenesis of senile plaques. *J. Neuropathol. Exp. Neurol.* **56**, 321–39 (1997).

100. Li, R. *et al.* Tumor Necrosis Factor Death Receptor Signaling Cascade Is Required for Amyloid-β Protein-Induced Neuron Death. *J. Neurosci.* **24**, 1760–1771 (2004).

101. Xue, Q. *et al.* Analysis of single-cell cytokine secretion reveals a role for paracrine signaling in coordinating macrophage responses to TLR4 stimulation. *Sci. Signal.* **8**, 1–12 (2015).

102. Guo, H., Callaway, J. B. & Ting, J. P. Y. Inflammasomes: Mechanism of action, role in disease, and therapeutics. *Nat. Med.* **21**, 677–687 (2015).

103. Shaftel, S. S., Griffin, W. S. T. & Kerry, K. M. The role of interleukin-1 in neuroinflammation and Alzheimer disease: An evolving perspective. *J. Neuroinflammation* **5**, 1–12 (2008).

104. Mrak, R. E. & Griffin, W. S. T. Glia and their cytokines in progression of neurodegeneration. *Neurobiol. Aging* **26**, 349–354 (2005).

105. Brugg, B. *et al.* Inflammatory processes induce β-amyloid precursor protein changes in mouse brain. *Proc. Natl. Acad. Sci. U. S. A.* **92**, 3032–3035 (1995).

106. Li, Y., Liu, L., Barger, S. W. & Griffin, W. S. T. Interleukin-1 mediates pathological effects of microglia on tau phosphorylation and on synaptophysin synthesis in cortical neurons through a p38-MAPK pathway. *J. Neurosci.* **23**, 1605–1611 (2003).

107. Griffin, W. S. T. *et al.* Glial-neuronal interactions in Alzheimer's disease: The potential role of a 'cytokine cycle' in disease progression. *Brain Pathol.* **8**, 65–72 (2006).

108. Olmos, G. & Lladó, J. Tumor necrosis factor alpha: A link between neuroinflammation and excitotoxicity. *Mediators Inflamm.* **2014**, 1–12 (2014).

109. Guerreiro, R. *et al.* TREM2 variants in Alzheimer's Disease. *N. Engl. J. Med.* **368**, 117–127 (2013).

110. Gratuze, M., Leyns, C. E. G. & Holtzman, D. M. New insights into the role of TREM2 in Alzheimer's disease. *Mol. Neurodegener.* **13**, 1–16 (2018).

111. Carmona, S. *et al.* The role of TREM2 in Alzheimer's disease and other neurodegenerative disorders. *Lancet Neurol.* **17**, 721–730 (2018).

112. Ulland, T. K. *et al.* TREM2 maintains microglial metabolic fitness in Alzheimer's disease. *Cell* **170**, 649–663 (2017).

113. Zhong, L. *et al.* Amyloid-beta modulates microglial responses by binding to the triggering receptor expressed on myeloid cells 2 (TREM2). *Mol. Neurodegener.* **13**, 1–12 (2018).

114. Leyns, C. E. G. *et al.* TREM2 function impedes tau seeding in neuritic plaques. *Nat. Neurosci.* **22**, 1217–1222 (2019).

115. Feuerbach, D. *et al.* ADAM17 is the main sheddase for the generation of human triggering receptor expressed in myeloid cells (hTREM2) ectodomain and cleaves TREM2 after Histidine 157. *Neurosci. Lett.* **660**, 109–114 (2017).

116. Wunderlich, P. *et al.* Sequential proteolytic processing of the triggering receptor expressed on myeloid cells-2 (TREM2) protein by ectodomain shedding and γ-secretase- dependent intramembranous cleavage. *J. Biol. Chem.* **288**, 33027–33036 (2013).

117. Suárez-Calvet, M. *et al.* sTREM 2 cerebrospinal fluid levels are a potential biomarker for microglia activity in early-stage Alzheimer's disease and associate with neuronal injury markers. *EMBO Mol. Med.* **8**, 466–476 (2016).

118. Suárez-Calvet, M. *et al.* Early changes in CSF sTREM2 in dominantly inherited Alzheimer's disease occur after amyloid deposition and neuronal injury. *Sci. Transl. Med.* **8**, 1–24 (2016).

119. Brosseron, F. *et al.* Characterization and clinical use of inflammatory cerebrospinal fluid protein markers in Alzheimer's disease. *Alzheimer's Res. Ther.* **10**, 1–14 (2018).

120. Zhou, J. *et al.* Imbalance of microglial TLR4/TREM2 in LPS-treated APP/PS1 transgenic mice: A potential link between Alzheimer's disease and systemic inflammation. *Neurochem. Res.* **44**, 1138–1151 (2019).

121. Ito, H. & Hamerman, J. A. TREM-2, triggering receptor expressed on myeloid cell-2, negatively regulates TLR responses in dendritic cells. *Eur. J. Immunol.* **42**, 176–185 (2012).

122. Graham, W. V., Bonito-Oliva, A. & Sakmar, T. P. Update on Alzheimer's disease therapy and prevention strategies. *Annu. Rev. Med.* **68**, 413–430 (2017).

123. Howard, R. *et al.* Donepezil and Memantine for moderate-to-severe Alzheimer's disease. *N. Engl. J. Med.* **366**, 893–903 (2012).

124. Schenk, D. *et al.* Immunization with amyloid-beta attenuates Alzheimer-disease-like pathology in the PDAPP mouse. *Nature* **400**, 173–177 (1999).

125. Pardridge, W. M. The blood-brain barrier: Bottleneck in brain drug development. *NeuroRx* **2**, 3–14 (2005).

126. Pardridge, W. M. Drug transport across the blood-brain barrier. *J. Cereb. Blood Flow Metab.* **32**, 1959–1972 (2012).

127. Johnsen, K. B. *et al.* Targeting transferrin receptors at the blood-brain barrier improves the uptake of immunoliposomes and subsequent cargo transport into the brain parenchyma. *Sci. Rep.* **7**, 1–13 (2017).

128. Weber, F. *et al.* Brain shuttle antibody for Alzheimer's disease with attenuated peripheral effector function due to an inverted binding mode. *Cell Rep.* **22**, 149–162 (2018).

129. Kopan, R. & Ilagan, M. X. G. The canonical Notch signaling pathway: Unfolding the activation mechanism. *Cell* **137**, 216–233 (2009).

130. Doody, R. S. *et al.* A phase 3 trial of Semagacestat for treatment of Alzheimer's disease. *N. Engl. J. Med.* **369**, 341–350 (2013).

131. Coric, V. *et al.* Targeting prodromal Alzheimer disease with Avagacestat: A randomized clinical trial. *JAMA Neurol.* **72**, 1324 (2015).

132. Egan, M. F. *et al.* Further analyses of the safety of verubecestat in the phase 3 EPOCH trial of mild-to-moderate Alzheimer's disease. *Alzheimer's Res. Ther.* **11**, 1–12 (2019).

133. Update on Phase 3 Clinical Trials of Lanabecestat for Alzheimer's Disease. *AstraZeneca* https://www.astrazeneca.com/media-centre/press-releases/2018/update-on-phase-iii-clinical-trials-of-lanabecestat-for-alzheimers-disease-12062018.html (2018).

134. Rogers, M. Lilly halts phase 2 trial of BACE inhibitor due to liver toxicity. *Alzheimer Res. Forum* (2013).

135. Leissring, M. A. Aβ-Degrading Proteases: Therapeutic Potential in Alzheimer Disease. *CNS Drugs* **30**, 667–675 (2016).

136. Loureiro, J. C. *et al.* Passive antiamyloid immunotherapy for Alzheimer's disease. *Curr. Opin. Psychiatry* **33**, 284–291 (2020).

137. Imbimbo, B. P. *et al.* Solanezumab for the treatment of mild-to- moderate Alzheimer's disease. *Expert Rev. Clin. Immunol.* **8**, 135–149 (2012).

138. Goure, W. F., Krafft, G. A., Jerecic, J. & Hefti, F. Targeting the proper amyloid-beta neuronal toxins: A path forward for Alzheimer's disease immunotherapeutics. *Alzheimers. Res. Ther.* **6**, 1–15 (2014).

139. Cummings, J. *et al.* A randomized, double-blind, placebo-controlled phase 2 study to evaluate the efficacy and safety of Crenezumab in patients with mild to moderate Alzheimer's disease. *Neurology* **90**, 1889–1897 (2018).

140. Ostrowitzki, S., Deptula, D., Thurjell, L., Bakhof, F. & Bohrmann, B. Mechanism of Amyloid Removal in Patients With Alzheimer Disease Treated With Gantenerumab. *Arch. Neurol.* **69**, 198–207 (2012).

141. ClinicalTrials.gov. *National Institute of Health* www.clinicaltrials.gov (2020).

142. Logovinsky, V. *et al.* Safety and tolerability of BAN2401 - a clinical study in Alzheimer's disease with a protofibril selective Aβ antibody. *Alzheimers. Res. Ther.* **8**, 14 (2016).

143. Sevigny, J. *et al.* The antibody aducanumab reduces Aβ plaques in Alzheimer's disease. *Nature* **537**, 50–56 (2016).

144. Bulaklak, K. & Gersbach, C. A. The once and future gene therapy. *Nat. Commun.* **11**, 1–4 (2020).

145. Stepanichev, M. Gene Editing and Alzheimer's Disease: Is There Light at the End of the Tunnel? *Front. Genome Ed.* **2**, 1–10 (2020).

146. Griciuc, A. *et al.* Alzheimer's disease risk gene CD33 inhibits microglial uptake of amyloid beta. *Neuron* **78**, 631–643 (2013).

147. Griciuc, A. *et al.* Gene therapy for Alzheimer's disease targeting CD33 reduces amyloid beta accumulation and neuroinflammation. *Hum. Mol. Genet.* **29**, 2920–2935 (2020).

148. Almeida, F. L. *et al.* MIR-NATs repress MAPT translation and aid proteostasis in neurodegeneration. *Nature* (2021).

149. LaFee, S. First-in-human clinical trial to assess gene therapy for Alzheimer's disease. *UC San Diego Health* https://health.ucsd.edu/news/releases/Pages/2021-02-18-first-in-human-clinical-trial-to-assess-gene-therapy-for-alzheimers-disease.aspx (2021).

150. Rackham, O. J. L. *et al.* A predictive computational framework for direct reprogramming between human cell types. *Nat. Genet.* **48**, 331–335 (2016).

151. Lachmann, P. J. The penumbra of thalidomide, the litigation culture and the licensing of pharmaceuticals. *Qjm* **105**, 1179–1189 (2012).

152. Cummings, J. Lessons Learned from Alzheimer Disease: Clinical Trials with Negative Outcomes. *Clin. Transl. Sci.* **11**, 147–152 (2018).

153. Barker, W. W. *et al.* Relative frequencies of Alzheimer disease, Lewy body, vascular and frontotemporal dementia, and hippocampal sclerosis in the state of Florida brain bank. *Alzheimer Dis. Assoc. Disord.* **16**, 203–212 (2002).

154. Togo, T., Cookson, N. & Dickson, D. W. Argyrophilic grain disease: neuropathology, frequency in a dementia brain bank and lack of relationship with apolipoprotein E. *Brain Pathol.* **12**, 45–52 (2006).

155. Deture, M. A. & Dickson, D. W. The neuropathological diagnosis of Alzheimer's disease. *Mol. Neurodegener.* **14**, 1–18 (2019).

156. Nelson, P. T. *et al.* 'New old pathologies': AD, PART, and cerebral age-related TDP-43 with sclerosis (CARTS). *J. Neuropathol. Exp. Neurol.* **75**, 482–498 (2016).

157. Aisen, P. S. *et al.* On the path to 2025: Understanding the Alzheimer's disease continuum. *Alzheimer's Res. Ther.* **9**, 1–10 (2017).

158. Canter, R. G., Penney, J. & Tsai, L. H. The road to restoring neural circuits for the treatment of Alzheimer's disease. *Nature* **539**, 187–196 (2016).

159. Xu, X. *et al.* Species and cell-type properties of classically defined human and rodent neurons and glia. *Elife* **7**, 1–47 (2018).

160. Drummond, E. & Wisniewski, T. Alzheimer's disease: Experimental models and reality. *Acta Neuropathol.* **133**, 155–175 (2018).

161. Penney, J., Ralvenius, W. T. & Tsai, L. H. Modeling Alzheimer's disease with iPSC-derived brain cells. *Mol. Psychiatry* **25**, 148–167 (2020).

162. Arber, C. *et al.* Mass spectrometry analysis of tau and amyloid-beta in iPSC-derived models of Alzheimer's disease and dementia. *J. Neurochem.* 1–13 (2021).

163. Choi, S. H. *et al.* A three-dimensional human neural cell culture model of Alzheimer's disease. *Nature* **515**, 274–278 (2014).

164. Lancaster, M. A. & Knoblich, J. A. Generation of cerebral organoids from human pluripotent stem cells. *Nat. Protoc.* **9**, 2329–2340 (2014).

165. Lancaster, M. A. *et al.* Guided self-organization and cortical plate formation in human brain organoids. *Nat. Biotechnol.* **35**, 659–666 (2018).

166. Wray, S. Modelling neurodegenerative disease using brain organoids. *Semin. Cell Dev. Biol.* **111**, 60–66 (2021).

167. De, S. *et al.* Different soluble aggregates of Aβ42 can give rise to cellular toxicity through different mechanisms. *Nat. Commun.* **10**, 1–11 (2019).

168. Heneka, M. T. *et al.* Neuroinflammation in Alzheimer's disease. *Lancet Neurol.* **14**, 388–405 (2015).

169. Lambert, M. P. *et al.* Diffusible, nonfibrillar ligands derived from Aβ1–42 are potent central nervous system neurotoxins. *Proc. Natl. Acad. Sci. U. S. A.* **95**, 6448–6453 (1998).

170. Wang, H. W. *et al.* Soluble oligomers of β amyloid (1-42) inhibit long-term potentiation but not long-term depression in rat dentate gyrus. *Brain Res.* **924**, 133–140 (2002).

171. Townsend, M., Shankar, G. M., Mehta, T., Walsh, D. M. & Selkoe, D. J. Effects of secreted oligomers of amyloid β-protein on hippocampal synaptic plasticity: A potent role for trimers. *J. Physiol.* **572**, 477–492 (2006).

172. Selkoe, D. J. Soluble oligomers of the amyloid β-protein impair synaptic plasticity and behavior. *Behav. Brain Res.* **192**, 106–113 (2008).

173. Ono, K., Condron, M. M. & Teplow, D. B. Structure-neurotoxicity relationships of amyloid β-protein oligomers. *Proc. Natl. Acad. Sci.* **106**, 14745–14750 (2009).

174. Kayed, R. *et al.* Common structure of soluble amyloid oligomers implies common mechanism of pathogenesis. *Science* **300**, 486–489 (2003).

175. Cleary, J. P. *et al.* Natural oligomers of the amyloid-β protein specifically disrupt cognitive function. *Nat. Neurosci.* **8**, 79–84 (2005).

176. Lesné, S. *et al.* A specific amyloid-β protein assembly in the brain impairs memory. *Nature* **440**, 352–357 (2006).

177. Dahlgren, K. N. *et al.* Oligomeric and fibrillar species of amyloid-β peptides differentially affect neuronal viability. *J. Biol. Chem.* **277**, 32046–32053 (2002).

178. Hong, W. *et al.* Diffusible, highly bioactive oligomers represent a critical minority of soluble Aβ in Alzheimer's disease brain. *Acta Neuropathol.* **136**, 19–40 (2018).

179. Kuo, Y. M. *et al.* Water-soluble Aβ (N-40, N-42) oligomers in normal and Alzheimer disease brains. *J. Biol. Chem.* **271**, 4077–4081 (1996).

180. Tomic, J. L., Pensalfini, A., Head, E. & Glabe, C. G. Soluble fibrillar oligomer levels are elevated in Alzheimer's disease brain and correlate with cognitive dysfunction. *Neurobiol. Dis.* **35**, 352–358 (2009).

181. Jin, M. *et al.* Soluble amyloid β-protein dimers isolated from Alzheimer cortex directly induce Tau hyperphosphorylation and neuritic degeneration. *Proc. Natl. Acad. Sci. U. S. A.* **108**, 5819–5824 (2011).

182. Murphy, M. P. & Levine III, H. Alzheimer's Disease and the Beta-Amyloid Peptide. *J. Alzheimer's Dis.* **19**, 311–323 (2010).

183. Saido, T. C., Yamao-Harigaya, W., Iwatsubo, T. & Kawashima, S. Amino- and carboxyl-terminal heterogeneity of β-amyloid peptides deposited in human brain. *Neurosci. Lett.* **215**, 173–176 (1996).

184. Benilova, I., Karran, E. & De Strooper, B. The toxic Aβ oligomer and Alzheimer's disease: An emperor in need of clothes. *Nat. Neurosci.* **15**, 349–357 (2012).

185. Esparza, T. J. *et al.* Soluble amyloid-beta aggregates from human Alzheimer's disease brains. *Sci. Rep.* **6**, 1–16 (2016).

186. De, S. *et al.* Soluble aggregates present in cerebrospinal fluid change in size and mechanism of toxicity during Alzheimer's disease progression. *Acta Neuropathol. Commun.* **7**, 1–13 (2019).

187. Li, S. & Selkoe, D. J. A mechanistic hypothesis for the impairment of synaptic plasticity by soluble Aβ oligomers from Alzheimer's brain. *J. Neurochem.* **154**, 583–597 (2020).

188. Zott, B. *et al.* A vicious cycle of β amyloid–dependent neuronal hyperactivation. *Science* **365**, 559–565 (2019).

189. Hector, A. & Brouillette, J. Hyperactivity Induced by Soluble Amyloid-β Oligomers in the Early Stages of Alzheimer's Disease. *Front. Mol. Neurosci.* **13**, 1–15 (2021).

190. Corbett, G. T. *et al.* PrP is a central player in toxicity mediated by soluble aggregates of neurodegeneration-causing proteins. *Acta Neuropathol.* **139**, 503–526 (2020).

191. Teplow, D. B. Preparation of amyloid β-protein for structural and functional studies. *Methods Enzymol.* **413**, 20–33 (2006).

192. Narayan, P. *et al.* Rare individual amyloid-β oligomers act on astrocytes to initiate neuronal damage. *Biochemistry* **53**, 2442–2453 (2014).

193. Narayan, P. *et al.* The extracellular chaperone clusterin sequesters oligomeric forms of the Aβ1–40 peptide. *Nat. Struct. Mol. Biol.* **19**, 79–83 (2016).

194. Flagmeier, P. *et al.* Ultrasensitive measurement of Ca2+ influx into lipid vesicles induced by protein aggregates. *Angew. Chemie* **129**, 1–6 (2017).

195. Walsh, D. M. *et al.* A facile method for expression and purification of the Alzheimer's disease-associated amyloid β-peptide. *FEBS J.* **276**, 1266–1281 (2009).

196. Hellstrand, E., Boland, B., Walsh, D. M. & Linse, S. Amyloid β-protein aggregation produces highly reproducible kinetic data and occurs by a two-phase process. *ACS Chem. Neurosci.* **1**, 13–18 (2010).

197. Khurana, R. *et al.* Mechanism of thioflavin T binding to amyloid fibrils. *J. Struct. Biol.* **151**, 229–238 (2005).

198. Montine, T. J. *et al.* National institute on aging-Alzheimer's association guidelines for the neuropathologic assessment of Alzheimer's disease: A practical approach. *Acta Neuropathol.* **123**, 1–11 (2012).

199. Pagan, J. K. *et al.* The t-SNARE syntaxin 4 is regulated during macrophage activation to function in membrane traffic and cytokine secretion. *Curr. Biol.* **13**, 156–160 (2003).

200. Huang, J. *et al.* A single peptide-major histocompatibility complex ligand triggers digital cytokine secretion in CD4+ T cells. *Immunity* **39**, 846–857 (2013).

201. Bogstedt, A. *et al.* Development of immunoassays for the quantitative assessment of amyloid-β in the presence of therapeutic antibody: Application to pre-clinical studies. *J. Alzheimer's Dis.* **46**, 1091–1101 (2015).

202. Whiten, D. R. *et al.* Nanoscopic Characterisation of Individual Endogenous Protein Aggregates in Human Neuronal Cells. *ChemBioChem* **19**, 2033–2038 (2018).

203. Ruggeri, F. S. *et al.* Nanoscale studies link amyloid maturity with polyglutamine diseases onset. *Sci. Rep.* **6**, 1–11 (2016).

204. Ruggeri, F. S., Šneideris, T., Vendruscolo, M. & Knowles, T. P. J. Atomic force microscopy for single molecule characterisation of protein aggregation. *Arch. Biochem. Biophys.* **664**, 134–148 (2019).

205. Chandradoss, S. D. *et al.* Surface passivation for single-molecule protein studies. *J. Vis. Exp.* 1–8 (2014).

206. de Vellis, J. & Cole, R. Preparation of mixed glial cultures from postnatal rat brain. *Methods Mol. Biol.* **814**, 49–59 (2012).

207. Chen, S.-H., Oyarzabal, E. A. & Hong, J. Preparation of rodent primary cultures for neuron–glia, mixed glia, enriched microglia, and reconstituted cultures with microglia. *Methods Mol. Biol.* **1041**, 231–240 (2013).

208. Monnet-Tschudi, F., Defaux, A., Braissant, O., Cagnon, L. & Zurich, M. G. Methods to assess neuroinflammation. *Curr. Protoc. Toxicol.* **50**, 1–20 (2011).

209. Ye, X. *et al.* Lipopolysaccharide induces neuroinflammation in microglia by activating the MTOR pathway and downregulating Vps34 to inhibit autophagosome formation. *J. Neuroinflammation* **17**, 1–17 (2020).

210. McQuade, A. *et al.* Gene expression and functional deficits underlie TREM2-knockout microglia responses in human models of Alzheimer's disease. *Nat. Commun.* **11**, 1–17 (2020).

211. Timmerman, R., Burm, S. M. & Bajramovic, J. J. An overview of in vitro methods to study microglia. *Front. Cell. Neurosci.* **12**, 1–12 (2018).

212. Henn, A. *et al.* The suitability of BV2 cells as alternative model system for primary microglia cultures or for animal experiments examining brain inflammation. *ALTEX* **26**, 83–94 (2009).

213. Tweedie, D. *et al.* A cellular model of inflammation for identifying TNF-α synthesis inhibitors. *J. Neurosci. Methods* **183**, 182–187 (2009).

214. Kacimi, R., Giffard, R. G. & Yenari, M. A. Endotoxin-activated microglia injure brain derived endothelial cells via NF-κB, JAK-STAT and JNK stress kinase pathways. *J. Inflamm.* **8**, 1–15 (2011).

215. Kirikae, T. *et al.* Endotoxin contamination in fetal bovine serum and its influence on tumor necrosis factor production by macrophage-like cells J774.1 cultured in the presence of the serum. *Int. J. Immunopharmacol.* **19**, 255–262 (1997).

216. Jian, M., Kwan, J. S. C., Bunting, M., Ng, R. C. L. & Chan, K. H. Adiponectin suppresses amyloid-β oligomer (AβO)-induced inflammatory response of microglia via AdipoR1-AMPK-NF-κB signaling pathway. *J. Neuroinflammation* **16**, 1–19 (2019).

217. Faller, P. & Hureau, C. Reproducibility Problems of Amyloid-β Self-Assembly and How to Deal With Them. *Front. Chem.* **8**, 1236 (2021).

218. Hughes, C. *et al.* Beta amyloid aggregates induce sensitised TLR4 signalling causing long-term potentiation deficit and rat neuronal cell death. *Commun. Biol.* **3**, 1–7 (2020).

219. Tripathy, D., Thirumangalakudi, L. & Grammas, P. RANTES upregulation in the Alzheimer's disease brain: A possible neuroprotective role. *Neurobiol. Aging* **31**, 8–16 (2010).

220. Schapansky, J. *et al.* Mek1/2 activity modulates trem2 cell surface recruitment. *J. Biol. Chem.* **296**, 1–11 (2021).

221. Smith, A. M. & Dragunow, M. The human side of microglia. *Trends Neurosci.* **37**, 125–135 (2014).

222. Galatro, T. F. *et al.* Transcriptomic analysis of purified human cortical microglia reveals age-associated changes. *Nat. Neurosci.* **20**, 1162–1171 (2017).

223. Gosselin, D. *et al.* An environment-dependent transcriptional network specifies human microglia identity. *Science* **356**, 1248–1259 (2017).

224. Colletier, J. P. *et al.* Molecular basis for amyloid-β polymorphism. *Proc. Natl. Acad. Sci. U. S. A.* **108**, 16938–16943 (2011).

225. Zheng, X. *et al.* Mechanism of C-terminal fragments of amyloid β-protein as Aβ inhibitors: Do C-terminal interactions play a key role in their inhibitory activity? *J. Phys. Chem. B* **120**, 1615–1623 (2016).

226. Smith, A. D. Imaging the progression of Alzheimer pathology through the brain. *Proc. Natl. Acad. Sci.* **99**, 4135–4137 (2002).

227. DeVos, S. L. *et al.* Synaptic tau seeding precedes tau pathology in human Alzheimer's disease brain. *Front. Neurosci.* **12**, 1–15 (2018).

228. Reas, E. T. Amyloid and tau pathology in normal cognitive aging. *J. Neurosci.* **37**, 7561–7563 (2017).

229. Fjell, A. M., McEvoy, L., Holland, D., Dale, A. M. & Walhovd, K. B. What is normal in normal aging? Effects of Aging, Amyloid and Alzheimer's Disease on the Cerebral Cortex and the Hippocampus. *Prog. Neurobiol.* **117**, 20–40 (2014).

230. Bennett, D. A. *et al.* Neuropathology of older persons without cognitive impairment from two community-based studies. *Neurology* **66**, 1837–1844 (2006).

231. Marks, S. M., Lockhart, S. N., Baker, S. L. & Jagust, W. J. Tau and β-amyloid are associated with medial temporal lobe structure, function, and memory encoding in normal aging. *J. Neurosci.* **37**, 3192–3201 (2017).

232. Li, J. *et al.* Oligomeric aβ-induced microglial activation is possibly mediated by NADPH oxidase. *Neurochem. Res.* **38**, 443–452 (2013).

233. Crutch, S. J. *et al.* Posterior cortical atrophy. *Lancet Neurol.* **11**, 170–178 (2012).

234. Joachim, C. L., Morris, J. H. & Selkoe, D. J. Diffuse senile plaques occur commonly in the cerebellum in Alzheimer's disease. *Am. J. Pathol.* **135**, 309–319 (1989).

235. Flanary, B. The role of microglial cellular senescence in the aging and Alzheimer diseased brain. *Rejuvenation Res.* **8**, 82–85 (2005).

236. Feng, G. *et al.* Repeated stimulation by LPS promotes the senescence of DPSCs via TLR4/MyD88-NF-κB-p53/p21 signaling. *Cytotechnology* **70**, 1023–1035 (2018).

237. Wang, H. *et al.* BRD4 contributes to LPS-induced macrophage senescence and promotes progression of atherosclerosis-associated lipid uptake. *Aging (Albany. NY).* **12**, 9240–9259 (2020).

238. Kim, C. O., Huh, A. J., Han, S. H. & Kim, J. M. Analysis of cellular senescence induced by lipopolysaccharide in pulmonary alveolar epithelial cells. *Arch. Gerontol. Geriatr.* **54**, e35–e41 (2012).

239. Wang, T. H. *et al.* Palbociclib induces DNA damage and inhibits DNA repair to induce cellular senescence and apoptosis in oral squamous cell carcinoma. *J. Formos. Med. Assoc.* **S0929-6646**, 30609–4 (2020).

240. Martinez Bueno, A. *et al.* Palbociclib-induced senescence upregulates the expression of IL-8 and may enhance the response to inmunotherapy. *Ann. Oncol.* **30**, 15–16 (2019).

241. Hunter, S. & Brayne, C. Do anti-amyloid beta protein antibody cross reactivities confound Alzheimer disease research? *J. Negat. Results Biomed.* **16**, 1–8 (2017).

242. Jin, M. *et al.* An in vitro paradigm to assess potential anti-Aβ antibodies for Alzheimer's disease. *Nat. Commun.* **9**, 1–13 (2018).

243. Kim, Y., Lee, Y., Kim, Y. & Lee, Y. Differential expressions of synaptogenic markers between primary cultured cortical and hippocampal neurons. *Exp. Neurobiol.* **21**, 61–67 (2012).

244. Harrill, J. A. *et al.* Ontogeny of biochemical , morphological and functional parameters of synaptogenesis in primary cultures of rat hippocampal and cortical neurons. *Mol. Brain* **8**, 1–15 (2015).

245. Baranov, S. V. *et al.* Mitochondria modulate programmed neuritic retraction. *Proc. Natl. Acad. Sci. U. S. A.* **116**, 650–659 (2019).

246. Calkins, M. J. & Reddy, P. H. Amyloid beta impairs mitochondrial anterograde transport and degenerates synapses in Alzheimer's disease neurons. *Biochim. Biophys. Acta - Mol. Basis Dis.* **1812**, 507–513 (2011).

247. Ruggeri, F. S. *et al.* The Influence of Pathogenic Mutations in α-Synuclein on Biophysical and Structural Characteristics of Amyloid Fibrils. *ACS Nano* **14**, 5213–5222 (2020).

248. Ruggeri, F. S., Šneideris, T., Vendruscolo, M. & Knowles, T. P. J. Atomic force microscopy for single molecule characterisation of protein aggregation. *Arch. Biochem. Biophys.* **664**, 134–148 (2019).

249. Je, G. *et al.* Endogenous Alpha-Synuclein Protein Analysis from Human Brain Tissues Using Single-Molecule Pull-Down Assay. *Anal. Chem.* **89**, 13044–13048 (2017).

250. Floden, A. M., Li, S. & Combs, C. K. β-Amyloid-stimulated microglia induce neuron death via synergistic stimulation of tumor necrosis factor α and NMDA receptors. *J. Neurosci.* **25**, 2566–2575 (2005).

251. Ji, Y. *et al.* Effects of Microglial Cytokines on Alzheimer's Disease-Related Phenomena. *J. Alzheimer's Dis.* **67**, 1021–1034 (2019).

252. Merlo, S., Spampinato, S. F., Beneventano, M. & Sortino, M. A. The contribution of microglia to early synaptic compensatory responses that precede β-amyloid-induced neuronal death. *Sci. Rep.* **8**, 1–11 (2018).

253. Passamonti, L. *et al.* PK11195 binding in Alzheimer disease and progressive supranuclear palsy. *Neurology* **90**, 1989–1996 (2018).

254. Surendranathan, A. *et al.* Early microglial activation and peripheral inflammation in dementia with Lewy bodies. *Brain* **141**, 3415–3427 (2018).

255. Malpetti, M. *et al.* Microglial activation and tau burden predict cognitive decline in Alzheimer's disease. *Brain* **143**, 1588–1602 (2020).

256. King, E. *et al.* Peripheral inflammation in prodromal Alzheimer's and Lewy body dementias. *J. Neurol. Neurosurg. Psychiatry* **89**, 339–345 (2018).

257. King, E. *et al.* Peripheral inflammation in mild cognitive impairment with possible and probable Lewy body disease and Alzheimer's disease. *Int. Psychogeriatrics* **31**, 551–560 (2019).

258. King, E. *et al.* Inflammation in mild cognitive impairment due to Parkinson's disease, Lewy body disease, and Alzheimer's disease. *Int. J. Geriatr. Psychiatry* **34**, 1244–1250 (2019).

259. Thomas, A. J. *et al.* Prospective longitudinal evaluation of cytokines in mild cognitive impairment due to AD and Lewy body disease. *Int. J. Geriatr. Psychiatry* **35**, 1250–1259 (2020).

260. Braak, H. & Braak, E. Demonstration of Amyloid Deposits and Neurofibrillary Changes in Whole Brain Sections. *Brain Pathol.* **1**, 213–216 (1991).

261. Goedert, M., Masuda-Suzukake, M. & Falcon, B. Like prions: The propagation of aggregated tau and α-synuclein in neurodegeneration. *Brain* **140**, 266–278 (2017).

262. Rajendran, L. *et al.* Alzheimer's disease β-amyloid peptides are released in association with exosomes. *Proc. Natl. Acad. Sci. U. S. A.* **103**, 11172–11177 (2006).

263. Simón, D. *et al.* Tau overexpression results in its secretion via membrane vesicles. *Neurodegener. Dis.* **10**, 73–75 (2012).

264. Kim, H. R. *et al.* Comparison of Amyloid β and Tau Spread Models in Alzheimer's Disease. *Cereb. Cortex* **29**, 4291–4302 (2019).

265. Maphis, N. *et al.* Reactive microglia drive tau pathology and contribute to the spreading of pathological tau in the brain. *Brain* **138**, 1738–1755 (2015).

266. Hopp, S. C. *et al.* The role of microglia in processing and spreading of bioactive tau seeds in Alzheimer's disease. *J. Neuroinflammation* **15**, 1–15 (2018).

267. Fu, H., Liu, B., Li, L. & Lemere, C. A. Microglia Do Not Take Up Soluble Amyloid-beta Peptides, But Partially Degrade Them by Secreting Insulin-degrading Enzyme. *Neuroscience* **443**, 30–43 (2020).